University of Southampton

Faculty of Engineering and Physical Sciences
School of Electronics and Computer Science
Digital Health and Biomedical Electronics Research Group

Multiple Model Switched Repetitive Control for FES-based Tremor Suppression

by

Tingze Fang
ORCiD: 0009-0000-7074-6869

A thesis for the degree of
Doctor of Philosophy

November 2025

University of Southampton

Abstract

Faculty of Engineering and Physical Sciences
School of Electronics and Computer Science

Doctor of Philosophy

Multiple Model Switched Repetitive Control for FES-based Tremor Suppression

by Tingze Fang

Tremor is a rhythmic, approximately periodic oscillation of the limbs caused by a range of neurological disorders. Functional electrical stimulation (FES) can help reduce tremor by artificially stimulating opposing muscles, thereby decreasing the oscillation's amplitude. However, various traditional control methods have not proven effective. Repetitive control (RC) has the potential to completely suppress tremor, however previous applications of repetitive controllers have limitations. In particular, they heavily rely on an accurate model of the limb dynamics, and their effectiveness declines steeply due to factors like muscle fatigue, spasticity, and modeling inaccuracies.

This thesis first reviews conventional tremor suppression technologies, before summarising existing applications of RC to suppress tremor. Then RC theory is summarised with focus on a general class of linear algorithms. Following this, their robustness is analysed for the first time using the gap metric. This enables a robust stability margin to be developed that characterises robustness of the system to unstructured modelling uncertainty. Building on these results, a design procedure for RC is proposed to maximise its robust performance. A control structure with an additional feedback compensator is also proposed and a corresponding robust design procedure is developed for this more general case. Both design procedures are applied to a model of the tremulous wrist in simulation. The results show that the repetitive controllers used in previous research are not robust to model uncertainty and have performance limitations. Finally, a multiple model switched repetitive control (MMSRC) framework is established, which has the potential to solve the current limitations of existing RC approaches. Experimental validation is performed with four participants, showing that MMSRC effectively suppresses tremor even in the presence of severe modeling uncertainty and fatigue, unlike conventional RC methods which often become unstable under these conditions. This is an important step towards home-based tremor suppression where model identification and expert tuning are not possible.

Contents

List of Figures **ix**

List of Tables **xiii**

Declaration of Authorship **xv**

Acknowledgements **xvii**

List of Symbols **xix**

Acronyms **xxiii**

1 Introduction **1**
1.1 Contributions and Publications . . . 3
1.2 Thesis Organisation . . . 4

2 Overview of Tremor Suppression and Repetitive Control **7**
2.1 Neurological Tremor . . . 7
2.2 Methods used to Characterise the Effectiveness of Tremor Suppression . . . 8
2.2.1 Metrics for Tremor Suppression . . . 9
2.2.2 Characterising Impact on Voluntary Movement . . . 10
2.3 Medical Methods for Tremor Suppression . . . 11
2.3.1 Invasive Methods . . . 11
2.3.2 Non-Invasive Methods . . . 12
2.4 Functional Electrical Stimulation . . . 14
2.4.1 Introduction to FES . . . 14
2.4.2 Repetitive Control . . . 16
2.5 Standard Repetitive Control Structure . . . 20
2.6 Basic Principle of Repetitive Control . . . 21
2.6.1 Repetitive Control Convergence Conditions . . . 24
2.6.2 The Inverse Repetitive Control Algorithm . . . 25
2.6.3 The Gradient Repetitive Control Algorithm . . . 26
2.6.4 The Optimal Repetitive Control Algorithm . . . 27
2.7 Repetitive Control Designed for Model Uncertainty . . . 30
2.7.1 Repetitive Control Designed for Uncertainty in Disturbance Frequency . . . 32
2.8 Tolerance of Uncertainty in RC Algorithms . . . 33
2.9 Summary . . . 34

3 Robust Stability and Robust Repetitive Control Design 35
3.1 Robust Stability . . . 35
3.1.1 Gain Stability . . . 35
3.1.2 The Gap Metric and Robust Stability . . . 36
3.1.3 Robust Stability of Repetitive Control . . . 38
3.2 Repetitive Control Design Procedure . . . 38
3.3 Repetitive Control with Inner Feedback Loop . . . 40
3.3.1 Closed-Loop Feedback Control System . . . 41
3.3.2 A Realisable Structure . . . 42
3.3.3 Convergence Conditions of the New Structure . . . 43
3.3.4 Robust Stability Margin of the New Structure . . . 43
3.3.5 Gain Stability of the New Structure . . . 45
3.3.6 Repetitive Control Design Procedure with Feedback Controller . . . 45
3.4 Application of Robust Design Procedure . . . 46
3.4.1 Establishment of an Idealized Wrist Model . . . 46
3.4.1.1 Parametrised Wrist Model . . . 49
3.5 Application of Design Procedure 1 . . . 50
3.5.1 Design Rationale for RC Algorithm Selection . . . 50
3.5.2 Decide on the Suppression Range . . . 51
3.5.3 Design $L(q)$ to Accelerate the Convergence . . . 51
3.5.4 Design Q Filter to Satisfy the Stability Condition . . . 52
3.5.5 Robustness of the FMI-RC to Parametric Uncertainty . . . 54
3.6 Application of Design Procedure 2 . . . 59
3.6.1 Design Rationale for RC Algorithm Selection . . . 59
3.6.2 Decide on the Suppression Range . . . 59
3.6.3 Design $K(q)$ to Improve the Suppression Range to Include Tremor Frequency f . . . 59
3.6.4 Design $L(q)$ to Accelerate the Convergence . . . 60
3.6.5 Design Q Filter to Satisfy the Stability Condition . . . 61
3.6.6 Robustness of the Gradient RC to Parametric Uncertainty . . . 63
3.7 Conclusion of Simulation Tests and Summary . . . 66

4 Multiple Model Switched Repetitive Control 67
4.1 Multiple Model Control . . . 67
4.2 Basic Principle of MMSRC . . . 69
4.2.1 MMSRC Robust Performance Conditions . . . 69
4.3 General MMSRC Design Procedure . . . 71
4.3.1 Design of Candidate Model Set and Controller set . . . 71
4.3.2 Estimator Design . . . 72
4.3.3 Switching Algorithm and Delay . . . 73
4.4 Application of MMSRC Design Procedure . . . 73
4.5 Robustness of MMSRC to Parametric Uncertainty . . . 78
4.5.1 Robustness of MMSRC (33 models) to Parametric Uncertainty . . . 78
4.5.2 Effect of Adding Candidate Models . . . 80
4.6 Conclusion of Simulation Tests . . . 82
4.7 Summary . . . 83

5 MMSRC for Hammerstein Systems 85
5.1 Modeling of Wrist Dynamics . . . 86
5.2 Extended Hammerstein RC Control System . . . 87
5.3 The Robust Stability of Hammerstein RC System . . . 88
5.4 Hammerstein MMSRC Structure . . . 94
5.4.1 MMSRC Robust Performance Conditions . . . 95
5.4.2 Candidate Model Set Design . . . 96
5.4.3 Estimator Design . . . 97
5.5 Summary . . . 98

6 Experiment Procedure and Results 99
6.1 Model Identification and Uncertainty Space Design . . . 99
6.1.1 Parameterized Model . . . 99
6.1.2 Identification of Nominal Model . . . 100
6.1.3 Establishing the Model Uncertainty Set . . . 101
6.2 Estimator Design for Uncertain Tremor . . . 101
6.3 Experimental System . . . 103
6.3.1 Wrist Rig . . . 103
6.3.2 Induced Tremor . . . 104
6.4 Experimental Procedure . . . 104
6.5 Experimental Results and Analyses . . . 107
6.5.1 Tremor Suppression Performance . . . 107
6.5.2 Switching of MMSRC . . . 115
6.5.3 Energy Consumption . . . 116
6.5.4 Conclusions based on Quantitative Analyses and Further Discussion 124
6.6 Summary . . . 125

7 Conclusions and Future Work 127
7.1 Conclusions . . . 127
7.2 Future Work . . . 130
7.2.1 Limitations of Current Testing Methods and Potential Solutions . 130
7.2.2 Transition to Testing People with Tremor . . . 131

References 133

List of Figures

2.1 Block diagram of standard closed-loop system. 20
2.2 General RC structure. 22
2.3 Optimal RC structure. 27

3.1 Ball of plants in uncertainty space U that are stabilised by controller C. . 37
3.2 Closed-loop system with additional feedback controller. 41
3.3 Closed-loop system with additional feedback controller after rearrangement. 42
3.4 Realizable closed-loop system with additional feedback controller. 42
3.5 a) Biomechanical wrist model with coactivation function h_{cc}, b) equivalent wrist model P. 47
3.6 a) Coactivation mapping h_{cc} with levels $\bar{u}_{fcr}$, $\bar{u}_{ecr}$. b) $f(u_2)$ for cases: zero coactivation ($\bar{u}_{fcr}, \bar{u}_{ecr} = 0$) [dashed line], and non-zero coactivation [solid line]. 48
3.7 Linear closed-loop system. 49
3.8 Stability conditions with different m_L ($Q(q) = I, n_L = 0$). 51
3.9 Stability conditions with different n_L ($Q(q) = I, m_L = 40$). 52
3.10 The impulse response of the low-pass filter with different n ($f_c = 5$ Hz). . 53
3.11 The amplitude response of the Q filter with different n ($f_c = 5$ Hz). 53
3.12 Stability conditions with different n ($f_c = 5$ Hz). 54
3.13 Performance index of FMI-RC with different b, k_p. 55
3.14 Stability condition and gap metric of FMI-RC with different b, k_p. 56
3.15 Performance index of FMI-RC of FMI-RC with different I_p, w_n. 56
3.16 Stability condition and gap metric of FMI-RC with different I_p, w_n. . . . 57
3.17 Performance index, stability condition and gap metric of FMI-RC with different c. 58
3.18 Performance index of FMI-RC with different f. 58
3.19 The impulse response of P and P_f with different K_p. 60
3.20 Stability conditions with different γ ($Q(q) = I$). 61
3.21 The impulse response of the low-pass filter with different n ($f_c = 2.5$ Hz). 61
3.22 The amplitude response of the Q filter with different n ($f_c = 2.5$ Hz). . . . 62
3.23 Stability conditions with different n ($f_c = 2.5$ Hz). 62
3.24 Performance index of gradient RC with different b, k_p. 63
3.25 Stability condition and gap metric of gradient RC with different b, k_p. . . 63
3.26 Performance index of gradient RC with different I_p, w_n. 64
3.27 Stability condition and gap metric of gradient RC with different I_p, w_n. . 64
3.28 Performance index, stability condition and gap metric of gradient RC with different c. 65
3.29 Performance index of gradient RC with different f. 65

4.1 MMSRC structure showing uncertain plant, estimator bank, and switched controller. 69
4.2 Criterion (4.1): Uncertainty space $\mathcal{U}$ is covered by gap metric balls of radius ρ and centre $P_i \in \mathcal{P}$. 70
4.3 Criterion (4.2): $\forall P \in \mathcal{U}$, there exists $C_i \in \mathcal{C}$ that stabilises it. 70
4.4 Performance index and stability condition with different c (FMI-RC is designed for the plant with $c = 30\%c_o$). 76
4.5 Performance index and stability condition with different c (FMI-RC is designed for the plant with $c = 250\%c_o$). 77
4.6 Performance index of MMSRC (33 models) with different b, k_p. 78
4.7 Performance index of MMSRC (33 models) with different I_p, w_n. 79
4.8 Performance index of MMSRC (33 models) with different c. 80
4.9 Performance index of MMSRC (145 models) with different b, k_p. 81
4.10 Performance index of MMSRC (145 models) with different I_p, w_n. 81
4.11 Performance index of MMSRC (145 models) with different c. 82

5.1 a) Biomechanical wrist model with coactivation function h_{cc}, b) simplified wrist model P. 86
5.2 Equivalent Hammerstein wrist model $P = (f, G)$. 87
5.3 Closed-loop nominal RC system. 87
5.4 a) Closed-loop nominal RC system $[P, C]$, b) True RC closed loop system $[P^*, C]$. 88
5.5 a) Closed-loop nominal RC system and b) standard form $[M, N]$. 89
5.6 Nominal RC system in standard form with additional disturbance x_0. . . 89
5.7 True RC closed loop system $[M^*, N]$ in standard form with internal biases $\tilde{w}_i = (\tilde{u}_i, \tilde{y}_i)^\top$, $i = 1, 2$. 92
5.8 Ball of true plants in uncertainty space $\mathcal{U}$ that are stabilised by controller C. 94
5.9 MMSRC structure showing true plant $P^* = (f^*, G^*)$, estimator bank, and switched controller. 95
5.10 Criterion (5.22): Uncertainty space $\mathcal{U}$ is covered by gap metric balls of radius ρ and centre $P_i \in \mathcal{P}$. 96
5.11 Criterion (5.23): $\forall P \in \mathcal{U}$, there exists $C_i \in \mathcal{C}$ that stabilises it. 96

6.1 Augmented plant (f, G) embedding disturbance in tremor. 102
6.2 a) Experimental set-up showing test participant seated in the wrist rig, b) artificially induced tremor device. 103
6.3 Artificially induced tremor. 108
6.4 RC and MMSRC error norms plotted against the period number for the ideal conditions test (Participant A). 109
6.5 RC and MMSRC error norms plotted against the period number for the ideal conditions test (Participant B). 109
6.6 RC and MMSRC error norms plotted against the period number for the ideal conditions test (Participant C). 110
6.7 RC and MMSRC error norms plotted against the period number for the ideal conditions test (Participant D). 110
6.8 RC and MMSRC error norms plotted against the period number for the muscle fatigue test (Participant A). 111

6.9 RC and MMSRC error norms plotted against the period number for the muscle fatigue test (Participant B). . . . 111
6.10 RC and MMSRC error norms plotted against the period number for the muscle fatigue test (Participant C). . . . 112
6.11 RC and MMSRC error norms plotted against the period number for the muscle fatigue test (Participant D). . . . 112
6.12 RC and MMSRC error norms plotted against the period number for the electrode misalignment test (Participant A). . . . 113
6.13 RC and MMSRC error norms plotted against the period number for the electrode misalignment test (Participant B). . . . 113
6.14 RC and MMSRC error norms plotted against the period number for the electrode misalignment test (Participant C). . . . 114
6.15 RC and MMSRC error norms plotted against the period number for the electrode misalignment test (Participant D). . . . 114
6.16 Switching signal $i_c(k)$ for MMSRC24 plotted against the period number for the misaligned electrodes test (Participant A). . . . 115
6.17 Control signal $u_w(k)$ during switch transition for MMSRC24 plotted against time for the misaligned electrodes test (Participant A). . . . 116
6.18 RC and MMSRC energy norms plotted against the period number for the ideal conditions test (Participant A). . . . 117
6.19 RC and MMSRC energy norms plotted against the period number for the ideal conditions test (Participant B). . . . 118
6.20 RC and MMSRC energy norms plotted against the period number for the ideal conditions test (Participant C). . . . 118
6.21 RC and MMSRC energy norms plotted against the period number for the ideal conditions test (Participant D). . . . 119
6.22 RC and MMSRC energy norms plotted against the period number for the muscle fatigue test (Participant A). . . . 120
6.23 RC and MMSRC energy norms plotted against the period number for the muscle fatigue test (Participant B). . . . 120
6.24 RC and MMSRC energy norms plotted against the period number for the muscle fatigue test (Participant C). . . . 121
6.25 RC and MMSRC energy norms plotted against the period number for the muscle fatigue test (Participant D). . . . 121
6.26 RC and MMSRC energy norms plotted against the period number for the electrode misalignment test (Participant A). . . . 122
6.27 RC and MMSRC energy norms plotted against the period number for the electrode misalignment test (Participant B). . . . 122
6.28 RC and MMSRC energy norms plotted against the period number for the electrode misalignment test (Participant C). . . . 123
6.29 RC and MMSRC energy norms plotted against the period number for the electrode misalignment test (Participant D). . . . 123

List of Tables

3.1 Values of wrist model parameters. 49

4.1 Parameter sets (33 models case). 77
4.2 Parameter sets (145 models case). 80

6.1 Participant physical characteristics 105
6.2 Performance indices for different controllers in different test scenarios . . . 108
6.3 Steady control energy for different controllers in different test scenarios . . 117

Declaration of Authorship

I, **Tingze Fang** declare that this thesis entitled

Multiple Model Switched Repetitive Control for FES-based Tremor Suppression

and the work presented in it is my own and has been generated by me as the result of my own original research.

I confirm that:

1. This work was done wholly or mainly while in candidature for a research degree at this University;
2. Where any part of this thesis has previously been submitted for a degree or any other qualification at this University or any other institution, this has been clearly stated;
3. Where I have consulted the published work of others, this is always clearly attributed;
4. Where I have quoted from the work of others, the source is always given. With the exception of such quotations, this thesis is entirely my own work;
5. I have acknowledged all main sources of help;
6. Where the thesis is based on work done by myself jointly with others, I have made clear exactly what was done by others and what I have contributed myself;
7. Parts of this work have been published as:

   (Fang and Freeman, 2023) and (Fang and Freeman, 2025)

Signed:..... Date:.....

Acknowledgements

Thanks to my supervisor, Professor Christopher Freeman. The completion of this thesis is inseparable from his guidance, feedback and suggestions.

List of Symbols

k	Discrete sample number
q	One-sample advance operator
s	Laplace variable
ω	Frequency in rad/s
I	Identity matrix
$\|\cdot\|_\infty$	Infinity norm
$\|\cdot\|$	2-norm
A	Magnitude of $P(q)$
b	Damping
$b_{m_L} \cdots b_{0_L} \cdots b_{n_L}$	Coefficients of $L(q)$
$b_{m_Q} \cdots b_{0_Q}$	Coefficients of $Q(q)$
$b_{P,C}$	Robust stability margin
c	Muscle amplitude
f_c	Cut-off frequency of the Q filter
f_{max}	Maximum suppression frequency
h_i	Impulse response coefficients of $P(q)$
I_p	Inertia
K_p	Proportional gain
k_p	Stiffness
m_L	Length of $L(q)$
m_Q	Length of $Q(q)$
N	Number of samples
N_J	Length of a set of frequencies
n	Order of the Q filter
T	Period
T_s	Sampling interval
W	Weighting factor
α	Gain
β	Learning gain of inverse repetitive control
γ	Learning gain of gradient repetitive control
$\vec{\delta}(P, P^*)$	Gap metric between plant P and plant P^*

$\mathcal{M}_P$	Graph of the system P
$\mathcal{M}_{\mathbf{P}^*}$	Graph of the system P^*
ϕ	Parameter vector comprising of coefficients of $L(q)$
φ	Phase of $P(q)$
ω_n	Natural frequency
$\{f_i\}_{i=0,1,...,N_J}$	A set of frequencies
$\mathbb{N}$	Set of natural numbers
d	Tremor
d_{ecr}	Tremor acting on the ECR
d_{fcr}	Tremor acting on the FCR
e	Error
u_0	Process noise
u_{0ecr}	Unknown process noise acting on the ECR
u_{0fcr}	Unknown process noise acting on the FCR
u_1	Plant input
u_2	Control action
u_{dis}	Disturbance
u_{ecr}	FES stimulation inputs of ECR
$\bar{u}_{ecr}$	Coactivation level of ECR
u_{fcr}	FES stimulation inputs of FCR
$\bar{u}_{fcr}$	Coactivation level of FCR
u_{max}	Maximal stimulation pulsewidth
u_{rc}	Output of repetitive controller
y_0	Measurement Noise
$\{y_i\}_{i=1,11,12}$	Plant output
y_2	Controller input
$\{y_i\}_{i=21,22}$	Input of $C_f(q)$
y_f	Input of feedback controller
y_{ref}	Reference trajectory
v_0	Noise
w_0	External disturbances
$\bar{w}_0$	External bias signal
w_1	Plant signals
$\bar{w}_1$	Internal plant bias
$C(q)$	Controller
$C_f(q)$	Controller consisting of $K(q)$ and $C(q)$
$IM(q)$	Internal model
$K(q)$	Feedback controller
$L(q)$	Filter defined by the specific RC algorithm
P^*	Unknown true plant
$P(q)$	Plant

$P_f(q)$	Plant consisting of $K(q)$ and $P(q)$
$P^{-1}(q)$	Inverse of $P(q)$
$P(q^{-1})$	Complex conjugate of $P(q)$
$Q(q)$	Zero-phase low-pass filter
J	Cost function
$\Pi_{P//C}$	Mapping from external signals to internal signals
ρ	Positive scalar function
U	Uncertainty space
$\mathcal{P}$	Candidate model set
$\{P_i\}_{i=0,1,\ldots,n}$	Models in the candidate model set
A_{P_i}	State matrix of P_i
B_{P_i}	Input matrix of P_i
C_{P_i}	Output matrix of P_i
x_{P_i}	State of P_i
$\mathcal{C}$	Controller set
$\{C_i\}_{i=0,1,\ldots,n}$	Repetitive controllers in the controller set
$\{E(P_i)\}_{i=0,1,\ldots,n}$	Estimators
$\hat{x}_{P_i}$	Estimated state of the plant P_i
Σ_{P_i}	Covariance of estimated state
$\tilde{y}_{P_i}$	Estimated output of P_i
r_{P_i}	Residual generated by $E(P_i)$
i	Switching signal
h_{cc}	Coactivation function
$h_{IRC,ecr}$	IRC of ECR
$h_{IRC,fcr}$	IRC of FCR
$\{c_{i,ecr}\}_{i=1,2,3}$	constant parameters of $h_{IRC,ecr}$
$\{c_{i,fcr}\}_{i=1,2,3}$	constant parameters of $h_{IRC,fcr}$
$f(u_2)$	Combination of IRC and h_{cc}
f	Nonlinear part of plant
H_{LAD}	Transfer function of LAD
H_{RBD}	Transfer function of RBD
G	Linear part of plant
$P_i = (f_i, G_i)$	Hammerstein system
$P^* = (f^*, G^*)$	Unknown true plant
$\phi()$	Inverse function of f
R	RC update
x_2	Output of R
A_Π	State matrix of $\Pi_{P//C}$
B_Π	Input matrix of $\Pi_{P//C}$
C_Π	Output matrix of $\Pi_{P//C}$
D_Π	Feedthrough matrix of $\Pi_{P//C}$

V_Π	Eigenvectors of A_Π
$\mathcal{U}$	Uncertainty set
A_N	State matrix of IM
B_N	Input matrix of IM
C_N	Output matrix of IM

Acronyms

ADRC	Active Disturbance Rejection Control
ARE	Algebraic Riccati Equation
BMI	Body Mass Index
CPG	Central Pattern Generator
DBS	Deep Brain Stimulation
ECR	Extensor Carpi Radialis
EMG	Electromyography
EMMSAC	Estimation Based Multiple Model Switched Adaptive Control
FCR	Flexor Capri Radialis
FDRC	Finite-dimensional Repetitive Control
FES	Functional Electrical Stimulation
FFT	Fast Fourier Transform
FIR	Finite Impulse Response
FMI-MP-RC	Frequency-Modified Inverse Multiperiodic Repetitive Control
FMI-RC	Frequency Modified Inverse Repetitive Control
GB-MP-RC	Gradient-based Multiperiodic Repetitive Control
HORC	High-Order Repetitive Control
HPF	High-pass Filter
IIR	Infinite Impulse Response
IRC	Isometric Recruitment Curve
LAD	Linear Activation Dynamics
LHS	Left Hand Side
LTI	Linear Time-invariant
MISO	Multiple-input Single-output
MM	Multimuscle
MMC	Multiple Model Control
MMSRC	Multiple Model Switched Repetitive Control
MP-RC	Multiperiodic Repetitive Control
MS	Multiple Sclerosis
PI	Proportional–Integral
PID	Proportional-Integral-Differential

PSD	Power Spectral Density
PWM	Pulse-Width Modulated
RBD	Rigid Body Dynamics
RC	Repetitive Control
RHS	Right Hand Side
RMSE	Root Mean Square Error
SATS	Selective and Adaptive Timely Electrical Stimulation
SDP	Semidefinite Programming
SISO	Single-input Single-output
SMP	Single-muscle-pair
ST	Stereotactic Thalamotomy
TSR	Tremor Suppression Rate
WFLC	Weighted Frequency Fourier Linear Combiner
ZPHP	Zero-Phase High-Pass

Chapter 1

Introduction

Tremor is a rhythmic, involuntary, periodic movement of the limbs often associated with neurological conditions (Bain, 2002), affecting a significant portion of patients; for instance, globally, between 25.5% and 58% of the 2 million individuals with multiple sclerosis and 70% of the 6 million people diagnosed with Parkinson's disease experience tremors (Mehanna and Jankovic, 2013; Gironell et al., 2018). This condition disrupts daily life; 95% of affected individuals report tremor in their hands and arms, which causes difficulties in activities such as writing, eating, drinking, and using tools, while also leading to embarrassment and challenges in maintaining employment, hobbies, and social interactions (Gupta et al., 2021). Moreover, neither surgery nor medication effectively suppresses tremor, and both carry substantial risks of side effects: medication can result in drowsiness, imbalance, and altered taste perception (Handforth, 2009), while surgical interventions like deep brain stimulation may cause complications such as gait disturbances, cerebral hemorrhage, and disorientation (Wagle Shukla and Okun, 2014; Zirh, 1999). In a survey of over $2,864$ people, only 3% underwent invasive surgery, and 35% discontinued medication due to adverse effects (Gupta et al., 2021).

Functional electrical stimulation (FES) artificially actuates muscles using electrical pulses to reduce tremor by activating muscles to oppose the tremulous motion. It provides an inexpensive, non-invasive alternative with no harmful side effects, working by delivering electrical pulses to surface electrodes placed on the skin over the muscle; these pulses stimulate action potentials in the peripheral nerves, activating the muscle fibers and causing them to contract. Prochazka et al. (1992a) first demonstrated that FES-based tremor suppression was possible, although conventional feedback methods could only reduce the oscillation amplitude by between 38% and 68% when applied to twelve patients; moreover, its effectiveness declined significantly due to muscle fatigue.

Although several control approaches have been applied to FES-based tremor suppression, repetitive control (RC) has achieved the greatest success due to its design for counteracting fixed period disturbances. Based on the internal model principle, RC can

theoretically completely suppress periodic tremors (Copur et al., 2019). Implementations of two RC algorithms (gradient RC and frequency modified inverse RC) demonstrated over 80% tremor suppression in five participants, surpassing the 50% reduction achieved by high-pass feedback compensators (Copur et al., 2019). Subsequent research extended the FMI-RC to dual-muscle stimulation, increasing the suppression rate from 78.48% to 87.73%. Simultaneously, with the aim of alleviating muscle fatigue, the required stimulation intensity was reduced, leading to an approximately 75% decrease in the average FES levels, thereby effectively mitigating muscle fatigue. However, the approach assumed a fixed tremor frequency, which does not account for the time-varying nature of tremors. Furthermore, the identification process for multiple muscle models is more complex and time-consuming compared to that for a single muscle model (Zhang et al., 2022a). To enhance robustness against multiple tremor frequencies, Zhang et al. (2022b) incorporated multiple internal models, increasing the suppression rate from 73.94% to 90.1% in four healthy participants with dual-frequency tremors. Even more encouragingly, a suppression rate of approximately 80% was achieved in a patient with intentional tremor. However, the design still does not fully address the issue of muscle fatigue during prolonged FES, and the system's performance may be affected by model uncertainty.

However, although the aforementioned studies established the superior performance of RC over alternative FES control approaches, they exhibited important limitations. These include time-consuming model identification processes requiring lengthy experimental sessions. Additionally, there is evidence of limited robustness to modeling inaccuracies caused by factors such as spasticity, muscle fatigue, or electrode movement (Page, 2020; Freeman et al., 2015). These critical limitations remain unaddressed both experimentally and theoretically, significantly restricting the translation potential of FES-based tremor suppression technology to hospitals, clinics, or home environments where accurate model identification and expert controller tuning are impractical. This provides strong motivation for developing new RC frameworks that address these challenges.

Furthermore, while numerous RC designs have been developed to handle model uncertainty (Xudong, 2012; Yu and Huang, 2015; Jiang et al., 2021; Gao et al., 2021; Chen et al., 2021), these robust RC methods all impose constraints on the underlying system dynamics and require the uncertainty to have a specific structure. Consequently, they are unable to address the more general, nonlinear, and unstructured forms of uncertainty common in biomedical systems. Additionally, most research has focused on designing RC updates to stabilize particular types of uncertain plants, instead of analyzing the robustness properties of broader classes of RC updates. This highlights a significant gap: there is a clear lack of analytical tools suitable for general nonlinear dynamics subject to unstructured model uncertainty that could guide general RC design.

1.1 Contributions and Publications

To address the research gaps highlighted above, the main contributions of this research are as follows:

- Gap metric based analysis has been applied to RC to connect the gain stability of the system and the standard stability condition of RC. Then a robust stability margin is derived to define set of plants that a general RC update stabilises. The results provide robust performance guarantees for a broader, less structured, class of model uncertainty than has previously been possible. Based on this, RC design procedures have been developed for a general closed-loop system and a closed-loop system with an additional feedback controller. Simulations verify the feasibility of the two design procedures. This provides guidance for designers to quantitatively evaluate the robustness of the system in practical applications or engineering. Based on the feasible design procedures, they can then tune parameters to trade off the system's convergence speed against its robustness.

- Theoretical and practical multiple model switched repetitive control (MMSRC) design procedures are then developed. MMSRC is then applied to tremor suppression. The simulations verify the feasibility of the practical MMSRC design procedure. Compared with the results of conventional RC, the simulation results demonstrate that MMSRC is more robust to model uncertainty. Increasing the number of candidate models can further enhance the robustness of MMSRC. Moreover, the novel practical design procedure provides designers with computationally less demanding guidance with validated feasibility. The simulation results offer reliable evidence for designers to make trade-offs between computational load and robustness.

- The robust performance bounds for conventional RC applied to Hammerstein systems is derived. Bounds are derived that define the robust performance of the RC system in terms of the degree of model mismatch. This enables designers to use this robustness analysis tool in a wider range of scenarios to quantitatively evaluate system robustness. The MMSRC framework for linear systems is then extended to Hammerstein systems with uncertain periodic disturbances. This extension builds upon gap metric stability analysis. It ensures guaranteed robust performance, provided the actual plant falls within an uncertainty set defined by the designer. The expanded MMSRC can also be applied to more scenarios involving nonlinear controlled objects, further enhancing its practicality. A design procedure is developed to efficiently satisfy the theoretical conditions while minimizing computational overhead. Consequently, this provides designers with a principled method to maximize robust performance in practical applications.

- The Hammerstein MMSRC framework is then applied to FES-based tremor suppression. Its feasibility is verified through high model uncertainty scenarios. The experimental results confirm MMSRC's superior performance over existing conventional RC schemes, along with its robustness to model uncertainty and ability to adapt to physiological changes. This demonstrates that MMSRC has the potential to eliminate the need for repeated model identification and parameters tuning, thus paving the way for its application in future settings like homes or clinics, where dedicated control designers may be lacking.

Results of this research has featured in the following publications:

- Fang, Tingze and Freeman, Christopher T. (2023) Multiple model switched repetitive control with application to tremor suppression. *In 2023 American Control Conference, ACC 2023.* vol. 2023-May, IEEE. pp. 3859-3864 . (doi:10.23919/ACC55779.2023.10156534).
- Fang, Tingze and Freeman, Christopher T. (2025) Multiple model switched repetitive control for tremor suppression. *Mechatronics*, Volume 110, 2025, 103392, ISSN 0957-4158. (doi: 10.1016/j.mechatronics.2025.103392).

1.2 Thesis Organisation

The thesis is structured as follows:

Chapter 2 initially introduces neurological tremor, then summarizes existing tremor suppression methods. It demonstrates the potential of FES and the limitations of current tremor control approaches. Subsequently, research on tremor suppression based on FES and RC is summarized, highlighting both the theoretical potential of RC to completely suppress tremor and the limitations of its current applications. It then reviews the framework and fundamental theory of standard RC and introduces a class of common RC algorithms. Subsequently, robust RC design techniques are summarized.

Chapter 3 employs a tool for measuring system robustness, termed the robust stability margin, whose calculation is based on the gap metric. Subsequently, based on the summarized robust theory, a general RC design procedure is proposed. Then an additional feedback controller and disturbance are introduced to form a new augmented system. The augmented design procedure for both the repetitive controller and the feedback controller is then summarised. Then, the design procedures are applied to an idealized wrist model. The results demonstrate the feasibility of using RC for tremor suppression, but also revealed that the existing RC lacks robustness to model uncertainty.

Chapter 4 introduces a structure termed "multiple model switched RC" and its fundamental principles. Building upon a comprehensive explanation of its general design procedure, a computationally less intensive design procedure is proposed. The new design procedure is then validated in simulation, where MMSRC controllers with varying numbers of candidate models are designed. The simulation results demonstrate that MMSRC is more robust against model uncertainty than conventional RC, and that increasing the number of candidate models further enhances MMSRC's robustness.

Chapter 5 initially extends the idealised wrist model built in Chapter 3 into a more general Hammerstein structure. Subsequently, the standard RC framework from Chapter 2 is extended to a structure applicable to wrist models that possess a nonlinear component. Building on this, the tool for analysing robustness introduced in Chapter 3, the robust stability margin, is also generalized to the Hammerstein structure. Based on the new robust theory, the MMSRC framework from Chapter 4 is further extended to support a Hammerstein structure. This paves the way for the experiments presented in the following Chapter 6.

Chapter 6 first explains the process of model identification and uncertainty space establishment in the experiment, extending the estimator part of MMSRC to encompass unknown tremors. It then details the experimental system and procedure. The designed RC and MMSRC controllers are applied to four human subjects. The experimental results validate the simulation conclusions from Chapter 4: MMSRC demonstrates greater robustness against model uncertainty than RC, although the improvement gained by increasing the number of candidate models was less pronounced. Additionally, the energy consumption of both RC and MMSRC is presented, providing evidence for researchers or designers to make trade-offs between performance and energy consumption.

Chapter 7 summarizes the conclusions, contributions, and limitations of this research. It also discusses potential future work that could be undertaken.

Chapter 2

Overview of Tremor Suppression and Repetitive Control

This chapter introduces neurological tremor and summarises the advantages and disadvantages of established tremor suppression methods. It then focuses on application of functional electrical stimulation to tremor suppression and reviews the current approaches taken in this area. Conclusions are drawn regarding the strengths and weaknesses of control strategies for effective tremor suppression. Based on this, the potential of repetitive control is examined in detail. It then provides the necessary background to understand the RC approach and reviews existing algorithms that have been applied to tremor suppression.

2.1 Neurological Tremor

Tremor is an involuntary, periodic oscillatory motion that occurs in the limbs and may be caused by diseases of the nervous system such as multiple sclerosis and Parkinson's disease (Bain, 2002). Globally, more than 2.8 million people have multiple sclerosis (MS) and more than 10.76 million people have Parkinson's disease (Wang et al., 2025; Peng et al., 2025). Among them, 25.5% to 58% of patients with MS and 70% of patients with Parkinson's disease have symptoms of tremor (Mehanna and Jankovic, 2013; Gironell et al., 2018). It can occur locally in an individual limb, or it can affect multiple parts of the body at the same time, such as the arms, head, feet, one side of the body or even the whole body (Elble, 2017). The frequency of tremor varies significantly depending on its underlying cause and type. While the overall frequency range reported in the literature spans from 2 to 18 Hz (Bhatia et al., 2018; Deuschl et al., 1998), specific tremor types exhibit characteristic bands. For instance, intention tremor, which is relevant to this study, typically occurs at lower frequencies, commonly between 0 and 5 Hz (Deuschl et al., 1998). Tremor is typically produced by the patient's intentional movement, and

as the target approaches, the amplitude of the tremor may increase. Consequently, this kind of periodic oscillation will not only affect the patient's daily life, but may also bring them serious psychological burden (Elble, 2017).

Tremor can be broadly classified into several types based on its etiology and clinical presentation. The most common forms include essential tremor, Parkinsonian tremor, and intention tremor.

- Essential tremor is one of the most prevalent movement disorders, typically presenting as a bilateral, postural or kinetic tremor of the hands and forearms, though it may also affect the head, voice, or lower limbs. Its frequency typically ranges between 4 and 12 Hz, and it is often exacerbated by voluntary actions such as writing or holding a cup (Bhatia et al., 2018; Okelberry et al., 2024).
- Parkinsonian tremor is a hallmark of Parkinson's disease, classically presenting as a unilateral resting tremor of the hand, which may diminish during voluntary movement. Its frequency typically lies between 4 and 6 Hz. In advanced stages, it may also manifest as a postural or kinetic tremor (Deuschl et al., 1998; Dirkx and Bologna, 2022).
- Intention tremor is characterized by oscillatory movements that worsen during goal-directed activities, such as reaching for an object. It is commonly associated with multiple sclerosis, cerebellar lesions, or stroke. The frequency of intention tremor is generally lower, typically between 0 and 5 Hz, and its amplitude often increases as the limb approaches the target (Deuschl et al., 1998; Bhatia et al., 2018).

Each type of tremor has distinct clinical features and frequency ranges. However, they all manifest as approximate periodic oscillations occurring in the limbs, which is crucial for designing targeted therapeutic approaches.

2.2 Methods used to Characterise the Effectiveness of Tremor Suppression

Evaluating the effectiveness of tremor suppression is critical for comparing different methods and translating them into clinical practice. Researchers have employed various metrics to quantify suppression performance, each with distinct advantages and limitations. This section consolidates these measures and discusses their relative merits. Additionally, it summarises how the impact of these interventions on voluntary movement has been characterised.

2.2.1 Metrics for Tremor Suppression

- Tremor Suppression Rate: The tremor suppression rate is one of the most straightforward and commonly metrics. It is often defined as the percentage reduction in the amplitude of tremor oscillation before and after the application of the control intervention. In this thesis, a normalised version of this metric, termed the performance index, is defined in (3.25) and used extensively in Chapter 3, Chapter 4, and Chapter 6. It is calculated as:

$$\text{performance index} = \max\left(1 - \frac{\|y_c\|}{\|y\|},\ 0\right)$$

  where $\|y_c\|$ is the 2-norm of the controlled wrist angle and $\|y\|$ is the 2-norm of the uncontrolled tremor. A value of 1 indicates complete suppression, while 0 indicates no suppression or instability. This metric is intuitive, easy to compute, and provides a direct, scalar measure of overall suppression effectiveness. The 2-norm captures the total signal energy, making it sensitive to both the amplitude and duration of residual tremor. However, it is an aggregate measure and does not provide insight into performance at specific frequencies. It can also be influenced by the signal length used for calculation.

- Reduction in Tremor Power: Another approach, particularly in studies employing frequency-domain analysis, is to compute the reduction in tremor power within the characteristic tremor frequency bands. The tremor power reduction was computed by first quantifying the tremor power within the frequency band from accelerometer data. The power spectral density (PSD) was derived using a fast Fourier transform (FFT), and tremor power was defined as the integral of the PSD over this frequency range. The reduction rate was then calculated by comparing the tremor power during stimulation to the baseline (pre-stimulation) power, using the formula:

$$\text{Reduction Rate} = 1 - \frac{\text{Tremor Power during Stimulation}}{\text{Tremor Power during Baseline}}$$

  This normalized metric allowed for the assessment of how effectively peripheral nerve stimulation attenuated tremor amplitude across trials (Kim et al., 2020). In (Pascual-Valdunciel et al., 2021), the reduction in tremor power is referred to as tremor reduction. Although the calculation formula differs—quantifying tremor reduction by analyzing kinematic data of joint angles recorded by sensors—the fundamental concept remains similar. Both approaches assess tremor suppression performance by measuring the decrease in tremor power. This kind of method is physiologically relevant as it directly targets the oscillatory component of the movement. It can distinguish between suppression of the tremor itself and changes in voluntary motion. However, its accuracy depends on the correct identification of the tremor frequency band, which may be time-varying. It also requires sufficiently

long data segments for reliable spectral estimation. This undoubtedly increases the computational load and makes it unsuitable for the evaluation of a large number of controllers.

2.2.2 Characterising Impact on Voluntary Movement

A significant challenge in FES-based tremor suppression is achieving tremor reduction without impeding the user's intentional voluntary movements. Researchers have employed several methods to quantify this interference:

In (Prochazka et al., 1992b), voluntary movement was qualitatively assessed during tracking tasks, where participants followed a moving target. The study did not employ specific numerical metrics, but instead used diagrams and descriptions to illustrate that voluntary movement was not significantly impaired. The researchers merely observed that tremor attenuation hindered voluntary intention. The study by (Padilha Lanari Bó et al., 2011) utilized an online tremor estimation algorithm to separate voluntary and tremulous motion, but did not explicitly quantify the effect of FES on voluntary performance.

In contrast, Freeman et al. (2015) and Copur et al. (2019) introduced more rigorous quantitative measures. Freeman et al. (2015) assessed the impact of the RC-FES intervention on voluntary movement using two primary metrics: the amplitude of voluntary movement at frequencies below 1 Hz, derived from frequency analysis of wrist joint angle data, and the root mean square error (RMSE) of all movement during step-tracking tasks. The amplitude metric directly quantifies the magnitude of intended motion by isolating low-frequency components associated with voluntary effort, providing a specific and objective measure of how the intervention affects voluntary control without confounding tremor-related movements. However, its limitation lies in the reliance on a fixed frequency cutoff, which may not fully capture individual variations in movement dynamics or aspects like smoothness and cognitive effort, and it does not account for multidimensional movement quality. The RMSE of all movement offers a broader performance indicator by measuring overall tracking accuracy, which benefits from simplicity and comprehensiveness but is limited by its inability to distinguish voluntary from involuntary contributions, potentially masking specific effects on voluntary movement and reflecting combined influences of tremor suppression and voluntary control changes.

In (Copur et al., 2019), the impact of interventions on voluntary motion was primarily described using the measure J_1 and its time domain counterpart Δy_v. These metrics quantify the distortion in voluntary movement by evaluating the difference between the intended voluntary output y_v (without intervention) and the actual output y (with intervention) over the voluntary frequency range $[0, \omega_c]$, where ω_c is the cutoff frequency separating voluntary and involuntary motion. Specifically, J_1 uses the infinity norm

to capture the maximum deviation in the frequency domain, while Δy_v employs the 2-norm on frequency filtered signals to assess overall error magnitude. The benefits of these metrics include their ability to isolate voluntary motion effects from tremor suppression by leveraging frequency domain analysis, providing a clear and mathematically rigorous quantification of interference. However, limitations include their dependence on the accurate selection of ω_c, which may vary between individuals, and the assumption that voluntary motion is strictly low-frequency, which may not hold in practice. Additionally, the infinity norm in J_1 can be sensitive to outliers, while the 2-norm in Δy_v may average out localized distortions, potentially underestimating intermittent interference.

In summary, assessing the effectiveness of tremor suppression requires a dual-focus approach: quantifying the reduction of tremor while evaluating the interference with voluntary movements. The selection of metrics is crucial, as it directly influences the interpretation of the controller's clinical feasibility, balancing the primary goal of suppressing tremor with the essential requirement of preserving natural motor function.

2.3 Medical Methods for Tremor Suppression

Several tremor suppression methods have been proposed and these can be briefly divided into invasive methods and non-invasive methods.

2.3.1 Invasive Methods

Invasive methods comprise deep brain stimulation (DBS) and stereotactic thalamotomy (ST). These are briefly summarised below.

DBS is a method of implanting electrodes into the patient's brain to control abnormal electrical activity (Benabid et al., 1987). In a research study by Sun et al. (2020), seven patients with intractable essential tremor were treated with DBS of the posterior subthalamic area. As a result, the patients' upper limb tremor and other symptoms were reportedly greatly improved after the operation, and the patient's quality of life also improved. However, the surgery was accompanied by side effects. Two of the patients developed balance disorders and one of the patient's right arm showed symptoms of paralysis after the surgery. Other studies have also shown that adverse reactions such as gait disturbance, cerebral hemorrhage, postoperative depression, and mental confusion may occur after DBS treatment (Wagle Shukla and Okun, 2014). In (He et al., 2020), a closed-loop deep brain stimulation system driven by thalamic local field potentials effectively suppressed tremor in three essential tremor patients while eliminating reliance on external sensors. However, the approach exhibited a notably high false positive rate, leading to unnecessary stimulation that may increase patient discomfort and accelerate battery depletion in implantable devices. A recent study by Geigel and

Gunduz (2024) used a closed-loop deep brain stimulation technique to detect patients' motor intentions based on motor cortex beta-wave power desynchronisation to reduce ineffective stimulation by initiating stimulation only when needed and stopping stimulation at rest or during sleep. Experiments were performed on only 1 patient, and the results validated the potential of closed-loop DBS in reducing ineffective stimulation, but exposed the problem of beta-wave false triggering during sleep. In addition, beta waves have limitations as biomarkers, and the lack of sleep stage detection leads to nonessential stimulation and accelerates the risk of battery depletion. The method may have potential side effects such as tolerance and undetected neuroadaptive effects due to prolonged stimulation.

ST involves incising the thalamus after local anesthesia, and ameliorating the target location with electrodes. In most cases, the tremor will disappear completely when the surgery is complete (Jankovic, 1995). According to the study by Zirh (1999), after ST surgery, at least 66% of patients experienced no tremor or only slight residual tremor. However, at the same time, side effects also appeared in patients. Some patients reported balance disorders, gait abnormalities and cognitive disorders. In twenty-one patients with tremor, there was a permanent numbness in the corner of the mouth, and three patients required a second operation. This confirms that there is undoubtedly a significant risk of side effects. Similar research by Jankovic (1995) also shows that, although most patients with intractable tremor improved or even reported that their tremor stopped, 58% of the sixty patients experienced side effects such as weakness and confusion after surgery. A recent systematic review reported significant improvement in contralateral upper extremity tremor, with reductions of up to 76–88% on standardized scales (Ghimire et al., 2024). This review, which synthesized 9 studies involving 274 patients, confirmed the functional benefits of the procedure, particularly for unilateral thalamotomy. However, the generalizability of these findings was constrained by the limited number of available studies, methodological heterogeneity, and the use of non-validated outcome measures in some instances. Furthermore, these therapeutic benefits were counterbalanced by a notable adverse event profile. Dysarthria emerged as the most frequent complication, and persistent limb weakness was also reported, with a higher incidence observed following bilateral procedures.

These studies show that invasive surgery may be able to achieve effective tremor suppression, but it is also accompanied by a risk of multiple side effects.

2.3.2 Non-Invasive Methods

Non-invasive methods can be divided into pharmacological treatment and non-phamacological methods. These are briefly summarised next.

Pharmacological treatments have similar characteristics to surgery, and although drug treatment is beneficial for tremor suppression, it can also cause adverse health effects. This was demonstrated in a study with twenty-five subjects with upper limb tremor (Handforth, 2009). Here the drug 'Zonisamide' was applied and was found to reduce the tremor, however it also introduced problems such as drowsiness, lack of energy, imbalance, and changes in taste. Research reported in (Ondo et al., 2006) also showed that the drug 'Topiramate' was effective for severe essential tremor, and the patient's motor tasks were improved. However, 31.9% of the two-hundred and eight patients experienced adverse events such as nausea and inattention (Ondo et al., 2006). Many patients even withdrew from the study due to adverse side effects. A recent study indicated that pharmacological interventions for tremor demonstrated variable efficacy across different tremor types, though often with notable limitations and side effects (Frei and Truong, 2022). Propranolol, which was effective for essential tremor, showed superior tremor reduction but was limited by cardiovascular risks such as bradycardia and hypotension. Primidone, another first-line treatment for essential tremor, frequently caused malaise, dizziness, and sedation. In Parkinsonian tremor, dopaminergic agents like levodopa reduced tremor by 30–50%, yet a significant subset of patients exhibited dopamine-resistant tremor. Anticholinergics, though historically used, were constrained by neuropsychiatric side effects, including confusion and hallucinations. Novel agents such as perampanel and octanoic acid showed promise in essential tremor but were hampered by dizziness, imbalance, and limited tolerability. Overall, while medications provided meaningful tremor control, their utility was frequently offset by adverse effects and incomplete response.

The category of non-invasive treatments comprise non-phamacological methods. The first example in this category is limb cooling. In (Feys et al., 2005) a freezing bag was wrapped around the forearm of a patient with essential tremor, and coolant was delivered from a cooling device to reduce the temperature of the skin to a constant level. It was found that the reduction in tremor was directly proportional to the degree of cooling. However, this method required at least fifteen minutes to deploy, and the effect was only maintained for about 30 minutes. In (Feys et al., 2023), peripheral cooling of the upper limb led to a significant reduction in intention tremor severity in persons with multiple sclerosis. In Experiment 1, cooling the forearm via cold pack or cryomanchet for 15 minutes led to a reduction in tremor, with effects lasting up to 25 minutes. Experiment 2, which applied whole-arm cooling, further reduced tremor within the first 30 minutes after cooling. Subjectively, patients reported a reduction in tremor perception. Although no major adverse effects were reported, cooling via ice immersion was less well-tolerated due to pain and the risk of skin injury. Overall, peripheral cooling offered a temporary, non-invasive tremor management strategy with potential risks, and required time to take effect.

The use of exoskeleton technology has also been proposed. This comprises an electromechanical device that was worn by the patient which applied force to counteract the tremor (Yi et al., 2019). However, this technique could not completely suppress the tremor (Huen et al., 2016). It was also been found to affect the patient's voluntary movement due to excessive damping force (Yi et al., 2019). For example, Zhou et al. (2021) designed a glove with a wearable exoskeleton. This system monitored joint motion in real-time using an inertial measurement unit and a weighted frequency Fourier linear combiner (WFLC) to separate tremor signals. It then used a distributed cable transmission system driven by a brushless motor to suppress the tremor. An experiment was conducted on only one Parkinsonian tremor patient, and the results showed that the suppression rates of resting tremor, postural tremor, and locomotion tremor were 73.1%-85.5%, 70.2%-81%, and 58.7%-65.0%, respectively. However, the device designed in this study was heavy and prolonged use may lead to muscle fatigue and significant discomfort. In addition, there was a delay in the control system that slowed the response during movement transitions. The accuracy of the WFLC algorithm was also insufficient. Potential side effects include exacerbation of elbow tremor due to improper weight distribution and loss of inhibition efficiency due to imperfect mechanical coupling. In other research, Garcia-Higuera et al. (2023) presented a lightweight wrist exoskeleton called TuMove that detected and suppressed tremor in real-time through a mechanical damping system combined with a proportional-integral-differential (PID) controller. Experiments were conducted with five healthy subjects. The results showed that the exoskeleton reduced the angular velocity of tremor by 50.7% and 38.6%. However, the method resulted in a limited range of motion in wrist extension, and caused muscle fatigue and local skin irritation due to prolonged wear.

From the above review, existing medical methods have several important limitations: While some invasive procedures can completely suppress tremor in certain cases, they are accompanied by significant risks of side effects and are not suitable for all patients. Non-invasive methods, however, cannot completely suppress tremor; they may cause harmful side effects to the body; they are often time-consuming to apply and their effect is short-lived; they usually impair voluntary action; they may be expensive; they may cause embarrassment to the user when worn in public.

2.4 Functional Electrical Stimulation

2.4.1 Introduction to FES

Functional electrical stimulation involves applying electrical signals to artificially activate muscle. When suitably applied this can replace lost function. FES manifests as a series of electrical pulses that trigger action potentials in peripheral nerves which then activate muscle contractions in related muscle fibers (Hamid and Hayek, 2008).

If suitably controlled, FES can replace or supplement the motor function of the limbs (Peckham and Knutson, 2005).

The first attempt to apply FES for tremor suppression was proposed in (Prochazka et al., 1992a) using a compensation filter feedback system. The researchers first built a model of the wrist, and then used it to design a compensated notch filter to suppress oscillations within $2-5$ Hz. This was tested on twelve patients with essential tremor due to Parkinson's disease or multiple sclerosis. The results showed that the tremor was suppressed by $38\%-73\%$ in amplitude (Prochazka et al., 1992b). However, four patients reported muscle fatigue and two patients found the stimulation to be uncomfortable. There was also evidence that it impeded patient's voluntary motion.

A subsequent study by Padilha Lanari Bó et al. (2011) employed an extended Kalman filter to estimate the tremor and voluntary motion components of the motion. The tremor component was then sent to a proportional-integral (PI) controller to generate the FES signal which was split between a pair of antagonistic muscles. Four unimpaired people and one patient with essential tremor were tested. Figures confirmed that the method was feasible, however this study did not show a quantitative suppression effect. In addition, the level of FES-induced co-contraction caused muscle fatigue and interfered with the voluntary movement of the patient.

An estimator based on a central pattern generator (CPG) was used for tremor suppression in (Luo et al., 2018). CPG is a biological neural model that describes the rhythmic movement behavior of animals. The mathematical model based on it can predict the limb movement. This method established a basis function model based on CPG, combined with an estimator to estimate tremor, and fed back the predicted tremor information to the controller as an error. Finally, the controller outputted the FES signal. The design of the controller was not mentioned. The study tested the system on the arm of a person with resting tremor, and results showed that the average tremor suppression rate was about 78%.

A combination of a neural network and FES was proposed by Vatanpour et al. (2015). The controller had a neural network embedded inside, and it was trained with a gradient descent method. The output of the neural network was the FES signal, and the input was the angle and speed of the tremor. However, the method used to obtain tremor information and adjust network parameters was not explained. This method was only tested on the elbow of one unimpaired person. No quantitative results were provided, however figures showed that tremor suppression was extremely mild. Since the neural network required a large amount of data for training, this method was extremely time-consuming to deploy and also carried a high computational load.

A recent study by Kim et al. (2020) used a wearable wireless system to apply peripheral nerve electrical stimulation. The system detected upper limb tremor in real-time via a triaxial accelerometer and controlled the stimulation using basic closed- and open-loop

stimulation modes with adjustable parameters. Nine patients with idiopathic tremor were recruited for the experiment, which showed an average reduction in tremor power of 42.17%. However the study had limitations including: uncontrolled patient medication may have affected the results, a single experimental task was tested, and muscle activity was not analysed. Potential side effects mainly comprised mild tingling or perceived discomfort during stimulation.

Subsequently Pascual-Valdunciel et al. (2021) employed closed-loop controlled intramuscular selective and adaptive timely electrical stimulation (SATS), which utilized real-time electromyography (EMG) to detect tremor activity in antagonist muscles and triggered submotor threshold stimulation of target muscles to suppress wrist flexion-extension tremor in essential tremor patients. Experiments were conducted on nine patients, and results demonstrated an average 32% acute tremor reduction during stimulation, with sustained tremor suppression observed in four patients 24 hours post-stimulation. Key limitations included incomplete parameter matching between surface and intramuscular stimulation conditions, and some patients reported no perceived effects due to low-intensity stimulation, which may have impacted the reliability of the outcomes.

The above studies confirm that existing FES-based tremor suppression technologies are feasible, but could not completely suppress the tremor. Although some of these methods had reasonable suppression within a certain frequency range, they degraded significantly due to muscle fatigue. In addition, the problem that they suppressed the patient's voluntary action was also a serious drawback.

2.4.2 Repetitive Control

The limitation of existing FES-based tremor suppression technologies in suppressing periodic disturbances naturally led to more targeted control approaches being applied. According to the internal model principle, in order to completely suppress periodic disturbances like tremor, it is necessary to embed an internal model of the disturbance inside the controller (Wonham and Francis, 1975). A controller is then designed to stabilise the series connection of the internal model and the plant. The internal model principle then guarantees that the joint angle asymptotically convergences to zero (i.e. the tremor is suppressed). The internal model structure gives rise to an update law which modifies the control signal applied over the current tremor period by taking the control signal from the previous period and adding a function of the error measured over the past period. RC hence learns from experience how to correct the control action.

The earliest research using RC for tremor suppression was by Verstappen et al. (2012). This first built a complete wrist model, and then used optimal control to stablise the series connection of the plant and internal model (Verstappen et al., 2012). This method

was tested on the wrists of four unimpaired people. An induced tremor was applied to enable the suppression effect to be seen. Although the results demonstrated that RC for FES-based tremor suppression was feasible, the single frequency tremor was only 80% suppressed. When testing whether the patient could move according to their own intentions, voluntary movements were prevented to a certain extent. When the frequency of tremor changed from a single fixed frequency to multiple fixed frequencies, the tremor suppression effect dropped to 69%. The same control scheme was subsequently tested on the wrists of nine unimpaired people with induced tremor (Freeman et al., 2015). The results showed that the amplitude of the single peak tremor was reduced by about 41%, but the voluntary intention also was reduced by about 12%. Like the previous studies, this again demonstrated that while the RC approach suppressed tremor, it also reduced participants' voluntary movements.

In (Copur et al., 2019) two different update laws were implemented to provide closed-loop stability of the RC system. One was termed frequency modified inverse RC (FMI-RC). It stabilised the system using a controller that embedded an inverse model of the system dynamics. The other update was termed gradient RC and was designed to be robust but less rapid than inverse RC. The key contribution of this research was to embed zero-phase high-pass (ZPHP) filtering in RC to remove tremor while not distorting lower frequency voluntary actions. In this study, FMI-RC, gradient RC and a simple HPF feedback controller were compared for tremor suppression performance and voluntary intention preservation. The HPF method used the same design procedure as (Prochazka et al., 1992a), but replaced the filter with HPF. Four unimpaired patients with induced tremor and one patient with multiple sclerosis were tested using the different controllers. Experimental results demonstrated that the tremor suppression rate of FMI-RC and gradient RC for the five participants exceeded 80%, while the suppression rate of HPF was only 50%. However, the tremor was still only a single frequency. The two RC schemes also caused about 30% distortion in the participants' voluntary intention. Although this was still lower than the 35% distortion of HPF, and the influence of RC on voluntary intention was improved by the ZPHP filter to 20%, this still showed that the negative influence of RC on patients' voluntary intention.

Subsequently, Zhang et al. (2022a) advanced their FES-based tremor suppression approach by integrating RC with a multimuscle (MM) stimulation strategy. Moving beyond single-muscle-pair (SMP) systems, they developed a multiple-input single-output (MISO) wrist musculoskeletal model with a Hammerstein structure, actuated by two pairs of muscles. To control this system, a feedforward linearizing controller was designed to compensate for the nonlinear muscle recruitment characteristics, combined with a feedback system. Two specific RC algorithms were implemented: FMI-RC and

gradient RC, to properly regulate the multichannel FES levels for suppressing the periodic tremor. Experimental validation involved four unimpaired participants with induced tremor and two intention tremor patients. The results demonstrated a substantial performance improvement over SMP methods, with the MM FES scheme achieving tremor suppression rates of up to 87.73% using FMI-RC and 83.43% using GB-RC, compared to a maximum of 78.48% with SMP FMI-RC. Crucially, the MM approach significantly reduced the required stimulation intensity, lowering the average FES levels of extensors and flexors by approximately 75%, thereby effectively mitigating muscle fatigue. However, the method possesses several limitations. It assumes a fixed tremor frequency, which does not reflect the time-varying nature of pathological tremors in real-world conditions. Furthermore, the identification process for the MISO model is more complex and time-consuming than for a SMP model. Finally, while the reduced stimulation level strongly suggests decreased fatigue, the study did not include a direct, prolonged functional assessment to conclusively demonstrate this advantage.

Zhang et al. (2022b) also developed a multi-periodic RC (MP-RC) strategy to address the more realistic scenario of tremors comprising multiple frequency components. The control framework integrates a linearizing controller to compensate for the nonlinear muscle recruitment dynamics, modeled using a Hammerstein structure, with a feedback RC controller. The core of the MP-RC is the embedding of multiple parallel internal models, each targeting a specific tremor frequency, thereby enabling simultaneous suppression of multi-frequency disturbances. Two implementation methods were proposed: a frequency-modified inverse MP-RC (FMI-MP-RC) and a novel gradient-based MP-RC (GB-MP-RC), both accompanied by rigorous closed-loop stability analysis. The method was rigorously validated through simulations and experiments involving four unimpaired participants and one intention tremor patient. In experiments with healthy subjects, where tremors at 2 Hz and 2.5 Hz were induced, the proposed MP-RC methods significantly outperformed existing techniques. The FMI-MP-RC and GB-MP-RC achieved remarkable tremor suppression rates (TSR) of approximately 90.1%, compared to 73.94% for single-periodic RC and 69.81% for a conventional filter-based controller. This superior performance was corroborated in the patient study, where the MP-RC methods attained TSRs of 82.21% and 80.24%, respectively, demonstrating a substantial improvement over single-frequency approaches. Despite the promising results, the authors acknowledge several limitations. A key assumption is that tremor frequencies are fixed and identified offline, whereas real-world physiological tremors can be time-varying. The design also does not fully address the issue of muscle fatigue during prolonged FES, and the system's performance may be affected by musculoskeletal model uncertainty.

In recent years, experiments were performed by Yin and Zhang (2024) using MATLAB and LabVIEW software platforms, together with myRIO hardware to implement real-time tremor signal acquisition and arm motion control. MATLAB simulation results showed that the system was able to effectively reduce the amplitude of wrist tremor and

converge the joint angle to zero, indicating that the tremor was successfully suppressed. However, experiments using LabVIEW performed poorly due to data issues. The article does not explicitly mention the scale of the actual human experiment, and it is surmised that the study relied heavily on simulation and hardware testing. Limitations of the methodology include dependence on model accuracy, complex parameter tuning, and unvalidated multi-joint scaling effects.

Then Zhang et al. (2024) proposed a composite control strategy combining Active Disturbance Rejection Control (ADRC) with High-Order Repetitive Control (HORC) to suppress wrist tremor. Experimental validation was conducted on 9 unimpaired subjects and 4 intention tremor patients, demonstrating an average tremor suppression rate of 87.76%, which represented an 11% improvement over traditional RC methods and effective handling of tremor frequency variations and musculoskeletal model uncertainties. However, the study did not consider the potential delays between motion measurement and stimulation application. Additionally, tremor frequency variations were confined to a narrow range, and uncertainties other than model variation such as electrode sheet misalignment were not considered.

All the aforementioned research on RC-based tremor suppression used artificially induced tremor, either induced by a motor or by FES applied to additional muscles. This enabled precise control over the frequency and amplitude of the resulting quasi-sinusoidal movement. However, pathological tremor stems from neurological dysfunction, involving spontaneous, uncontrolled muscle motion within the limb (Bain, 2002). Unlike the single frequency tremor often induced artificially for experimental purposes, pathological tremor is more complex. Its frequency, while relatively stable for a given type, is not absolutely singular and can exhibit time-varying characteristics and multiple harmonic components (Bhatia et al., 2018). Furthermore, its amplitude is readily influenced by physiological and psychological states, such as anxiety or fatigue. Its movement pattern can be more complex, potentially involving multiple tremor directions, though primarily manifesting as horizontal left-right shaking, and is often accompanied by other symptoms like rigidity or bradykinesia (Elble, 2017).

The above approaches demonstrate that RC improves upon previous FES-based technologies, however they all have key drawbacks:

1) Time-consuming model identification. The process of model identification requires a lengthy data collection session.

2) Lack of robustness to modelling inaccuracy, spasticity, muscle fatigue or electrode movement. Testing has tried to avoid these affects by being short and identifying the model in the same session as the tests.

3) Lack of robustness to time-varying tremor frequencies. Whether using a single internal model or multiple internal models, each is only designed for a fixed known

frequency. However, the frequency of the tremor in reality is time-varying within a wide range.

4) The controller affects voluntary intention. Although adding a ZPHP can help reduce the distortion of voluntary actions to a certain degree, the effect is imperfect.

2.5 Standard Repetitive Control Structure

Critiques of FES-based control methods have shifted the discussion toward control strategies specifically designed for periodic disturbances: RC. The following section will delve into the fundamental principles of RC.

The standard closed-loop system representation is shown in Figure 2.1. This will be used to summarise the basic RC approach and then to facilitate subsequent robustness analysis. Plant operator P is assumed to be linear and maps input signal u_1 to the output signal y_1. Control operator C is also assumed to be linear and generates control action u_2 in response to receiving input signal y_2. Signals u_0 and y_0 represent unknown external process and measurement noise respectively. Signal u_{dis} is included to represent an additional known external signal (e.g. a tremor). Signal y_{ref} denotes a prescribed reference signal that the plant output is required to follow. The control problem is to design FES input signal u_2 such that the effect of tremor u_{dis} is removed from joint angle y_1. For tremor suppression, reference signal $y_{\text{ref}} = 0$, although it is retained here for generality.

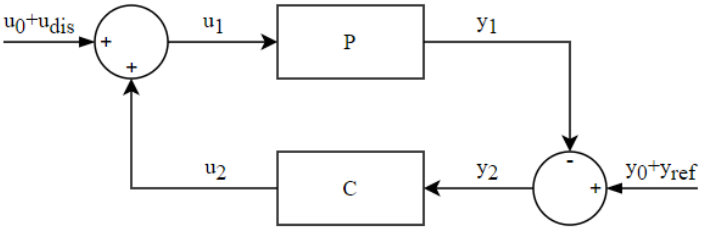

FIGURE 2.1: Block diagram of standard closed-loop system.

The signal relationships associated with Figure 2.1 are given by

$$\begin{cases} y_1 = Pu_1 \\ u_1 = u_0 + u_2 + u_{dis} \\ u_2 = Cy_2 \\ y_2 = y_0 + y_{ref} - y_1 \end{cases} . \tag{2.1}$$

All signals are assumed to belong to the l^2 space of all discrete-time signals with bounded 2-norm. In the case of RC, both disturbance u_{dis} and reference signal y_{ref} are assumed to be N-periodic, i.e. for a fixed $N \in \mathbb{N}_+$,

$$u_{dis}(k) = u_{dis}(k+N), \quad y_{ref}(k) = y_{ref}(k+N), \ \forall k \in \mathbb{N} \tag{2.2}$$

where k is the discrete time index. The number of samples in each period, N, is computed as the integer

$$N = \frac{T}{T_s} \tag{2.3}$$

where T is the period in seconds and T_s is the sampling interval. The RC problem is to design C to make y_1 asymptotically converge to the reference signal y_{ref}.

Convergence to y_{ref} is usually only possible when u_0, y_0 are both zero, and hence these signals are neglected in most RC designs. In practice, however, it is necessary to ensure that all signals remain bounded in the presence of external noise. This can be done by examining the mapping between the external and internal signals given by

$$\begin{aligned} \begin{pmatrix} u_1 \\ y_1 \end{pmatrix} &= \begin{pmatrix} (I+CP)^{-1} & (I+CP)^{-1}C \\ P(I+CP)^{-1} & P(I+CP)^{-1}C \end{pmatrix} \begin{pmatrix} u_0 + u_{dis} \\ y_0 + y_{ref} \end{pmatrix} \\ &= \begin{pmatrix} I \\ P \end{pmatrix} (I+CP)^{-1} \begin{pmatrix} I, C \end{pmatrix} \begin{pmatrix} u_0 + u_{dis} \\ y_0 + y_{ref} \end{pmatrix} \end{aligned} \tag{2.4}$$

where I is the identity matrix.

2.6 Basic Principle of Repetitive Control

The most common form of RC update is given by

$$u_2(k+N) = Q(q)[u_2(k) + L(q)y_2(k)], \quad u_2(-k) = 0 \quad \forall k \in \mathbb{N} \tag{2.5}$$

where q is the one-sample advance operator, i.e. $qx(k) = x(k+1)$, $Q(q)$ is a so-called 'robustness' filter, and $L(q)$ is a filter defined by the specific RC algorithm (Pipeleers and Moore, 2014). Update (2.5) can be represented as the system shown in Figure 2.2.

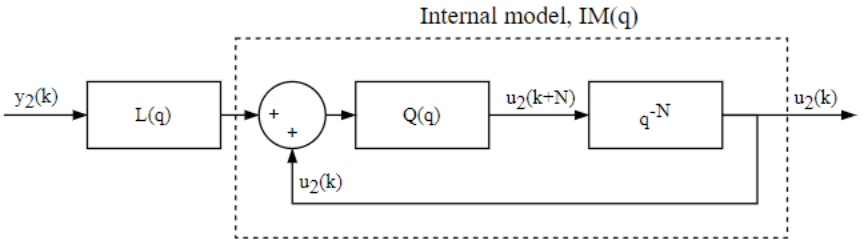

FIGURE 2.2: General RC structure.

It follows that the transfer function of the repetitive controller is

$$C(q) = \frac{u_2(k)}{y_2(k)} = \frac{Q(q)L(q)}{q^N - Q(q)} \ . \tag{2.6}$$

This contains a structure called an 'internal model' which can generate any N-period signal and is given by

$$IM(q) = \frac{Q(q)}{q^N - Q(q)} \ . \tag{2.7}$$

The remaining component, $L(q)$, is used to stabilise the closed-loop system. According to the internal model principle of (Wonham and Francis, 1975), this then guarantees ideal tracking of the trajectory y_{ref} in the absence of noise. The learning operator $L(q)$ has the general finite impulse response (FIR) form

$$L(q) = b_{m_L} q^{m_L} + \cdots + b_{1_L} q + b_{0_L} + b_{1_L} q^{-1} + \cdots + b_{n_L} q^{-n_L} \tag{2.8}$$

and $Q(q)$ usually takes the form of a zero-phase low-pass filter with FIR form

$$Q(q) = b_{m_Q} q^{m_Q} + \cdots + b_{1_Q} q + b_{0_Q} + b_{1_Q} q^{-1} + \cdots + b_{m_Q} q^{-m_Q} \tag{2.9}$$

where m_L, n_L, and m_Q are positive integers determining the order of the operators. However $L(q)$ and $Q(q)$ are chosen, they must give rise to a controller $C(q)$ which is causal. Substituting (2.8) and (2.9) into (2.5) gives

$$\begin{aligned} u_2(k+N) =& Q(q)u_2(k) + Q(q)L(q)y_2(k) \\ =& b_{m_Q} u_2(k+m_Q) + \cdots + b_{m_Q} u_2(k-m_Q) + b_{m_Q} b_{m_L} y_2(k+m_Q+m_L) \\ &+ \cdots + b_{m_Q} b_{n_L} y_2(k-m_Q-n_L) \end{aligned}$$

so that

$$\begin{aligned} u_2(k) =& b_{m_Q} u_2(k + m_Q - N) + \cdots + b_{m_Q} u_2(k - m_Q - N) \\ &+ b_{m_Q} b_{m_L} y_2(k + m_Q + m_L - N) + \cdots + b_{m_Q} b_{n_L} y_2(k - m_Q - n_L - N) \end{aligned} \tag{2.10}$$

must be causal. The term with highest sample number on the right hand side (RHS) of (2.10) is $y_2(k + m_Q + m_L - N)$. Therefore for causality m_Q and m_L must be chosen to satisfy

$$m_Q + m_L \leqslant N \, . \tag{2.11}$$

Ignoring noise (i.e. setting u_0, $y_0 = 0$), the closed-loop plant output can be obtained by substituting (2.6) into the bottom row of (2.4) to give

$$\begin{aligned} y_1(k) &= \frac{Q(q)P(q)L(q)}{q^N - Q(q)(I - P(q)L(q))} y_{ref}(k) + \frac{P(q)(q^N - Q(q))}{q^N - Q(q)(I - P(q)L(q))} u_{dis}(k) \\ &= \frac{Q(q)P(q)L(q)y_{ref}(k) + P(q)(q^N - Q(q))u_{dis}(k)}{q^N - Q(q)(I - P(q)L(q))} \end{aligned} \tag{2.12}$$

which leads to the error equation

$$\begin{aligned} y_2(k) &= y_{ref}(k) - y_1(k) \\ &= y_{ref}(k) - \frac{Q(q)P(q)L(q)y_{ref}(k) + P(q)(q^N - Q(q))u_{dis}(k)}{q^N - Q(q)(I - P(q)L(q))} \\ &= \frac{(q^N - Q(q))y_{ref}(k) - P(q)(q^N - Q(q))u_{dis}(k)}{q^N - Q(q)(I - P(q)L(q))} \, . \end{aligned} \tag{2.13}$$

If the filter is chosen as $Q(q) = I$, the numerator of (2.13) becomes

$$\begin{aligned} (q^N - I)y_{ref}(k) - P(q)(q^N - I)u_{dis}(k) & \\ &= q^N y_{ref}(k) - y_{ref}(k) - P(q)(q^N u_{dis}(k) - u_{dis}(k)) \\ &= y_{ref}(k + N) - y_{ref}(k) - P(q)(u_{dis}(k + N) - u_{dis}(k)) \\ &= 0 \end{aligned} \tag{2.14}$$

where the last equation follows since u_{dis} and y_{ref} are N-periodic. This means that the error will asymptotically converge to 0 if and only if the poles of transfer function (2.13) are stable. If $Q(q) \neq I$, then convergence will still occur, but generally not to zero error. The convergence rate depends on the location of the closed-loop poles and will be summarised next.

2.6.1 Repetitive Control Convergence Conditions

Conventional RC design ignores external disturbances and considers only the stability of the closed-loop error dynamics. This corresponds to requiring $P(q)$ and the poles of closed-loop system (2.12) are stable. The latter are the N solutions to

$$q^N = Q(q)(I - P(q)L(q)) \tag{2.15}$$

which, according to the Nyquist stability criterion, must all be contained in the unit circle (Longman, 2000). This directly leads to the well-known sufficient condition for stability

$$\|Q(q)(I - P(q)L(q))\|_\infty := \eta < 1 \tag{2.16}$$

which can be expressed in the frequency domain as

$$\sup_{\omega\in[0,2\pi]} \left|Q(e^{j\omega})(I - P(e^{j\omega})L(e^{j\omega}))\right| := \eta < 1 \tag{2.17}$$

where ω is the frequency in rad/s. The smaller the left hand side (LHS) value of (2.17), the faster the convergence rate is at the corresponding frequency.

As stated in Section 2.6, selecting $Q(q) \neq I$ impairs the tracking performance. This can be shown by computing the limiting value of the error signal in the absence of external noise (u_0, $y_0 = 0$). This is done by combining (2.1), (2.2) and (2.5) to give

$$\begin{aligned} e(k+N) =& y_2(k+N) \\ =& y_{ref}(k) - y_1(k+N) \\ =& Q(q)(I - P(q)L(q))e(k) + P(q)(Q(q) - I)u_{dis}(k) + (I - Q(q))y_{ref}(k) \end{aligned} \tag{2.18}$$

and it follows that the error equation after $i \in \mathbb{N}$ cycles is

$$\begin{aligned} e(k+Ni) =& \left[Q(q)(I - P(q)L(q))\right]^i e(k) \\ &+ \sum_{j=0}^{i} \left[Q(q)(I - P(q)L(q))\right]^j \left[P(q)(Q(q) - I)u_{dis}(k) + (I - Q(q))y_{ref}(k)\right] . \end{aligned} \tag{2.19}$$

If convergence condition (2.16) is satisfied, then the error (2.19) convergences to a fixed signal as i tends to infinity. In particular, since $\|Q(q)(I - P(q)L(q))\|_\infty < 1$, the first term in (2.19) converges to 0 and the limiting error then becomes

$$\begin{aligned}
&\lim_{i\to\infty} e(k+Ni) \\
&\quad = 0 + \sum_{j=0}^{\infty} \left[Q(q)(I - P(q)L(q))\right]^j \left[P(q)(Q(q) - I)u_{dis}(k) + (I - Q(q))y_{ref}(k)\right] \\
&\quad = \left(I - \left[Q(q)(I - P(q)L(q))\right]\right)^{-1} \left[P(q)(Q(q) - I)u_{dis}(k) + (I - Q(q))y_{ref}(k)\right] .
\end{aligned} \tag{2.20}$$

over all samples $k = 0, 2, \cdots, N-1$ of the period.

It is therefore clear that when $Q(q) \neq I$ the error will not converge to zero for an arbitrary reference or filter. The RC design problem is therefore to select $L(q)$ and $Q(q)$ to reduce the LHS of (2.16) or (2.17), while still providing convergence to zero error over a sufficiently broad frequency range. Popular design choices are now examined.

2.6.2 The Inverse Repetitive Control Algorithm

In order to reduce the LHS of (2.16), the simplest way is to set $Q(q) = I$ and design $L(q)$ as an inverse operator to minimize $\|I - P(q)L(q)\|_\infty$. This was proposed in (Songjun, 2014) using the selection

$$L(q) = \beta P^{-1}(q) \tag{2.21}$$

where β is a learning gain used to change the convergence rate. However, in practice $P(q)$ is generated by sampling a continuous plant $P(s)$, which is known to introduce new zeros through the use of a zero-order hold (Longman, 2010). This means that the inverse of $P(q)$ may contain poles outside the unit circle, resulting in an unstable $L(q)$. This problem has meant researchers have to generate a stable approximation to $P^{-1}(q)$.

Frequency modified inverse RC (FMI-RC) is an approximation of inverse RC and was proposed in (Panomruttanarug and Longman, 2004). It minimizes $\|I - P(q)L(q)\|_\infty$ by selecting the coefficients of $L(q)$ in a limited frequency range. This is achieved by choosing the coefficients of $L(q)$, $\phi := [b_{m_L} \cdots b_{0_L} \cdots b_{n_L}]^\top$ to minimize the cost function

$$J = \sum_{i=0}^{N_J} [1 - P(e^{j\omega_i})L(e^{j\omega_i})]W_i[1 - P(e^{j\omega_i})L(e^{j\omega_i})]^* \tag{2.22}$$

where $\omega_i = 2\pi f_i T_s$, $\{f_i\}_{i=0,1,\ldots,N_J}$ is a set of N_J frequencies chosen from 0 to $\frac{1}{2T_s}$, and W_i is a weighting factor applied to the i-th frequency.

The solution to $\min_\phi J$ is $\phi = \Gamma^{-1}\Phi$, where

$$\Gamma := \sum_{i=0}^{N_J} W_i A^2(\omega_i) \Psi_i \,,$$

in which

$$\Psi_i = \begin{bmatrix} 1 & \cos(\omega_i) & \cdots & \cos((m_L+n_L)\omega_i) \\ \cos(\omega_i) & 1 & \cdots & \cos((m_L+n_L-1)\omega_i) \\ \vdots & \vdots & \ddots & \vdots \\ \cos((m_L+n_L)\omega_i) & \cos((m_L+n_L-1)\omega_i) & \cdots & 1 \end{bmatrix}$$

and

$$\Phi = \sum_{i=0}^{N_J} W_i A(\omega_i) \begin{bmatrix} \cos((m_L)\omega_i + \varphi(\omega_i)) \\ \vdots \\ \cos((-n_L)\omega_i + \varphi(\omega_i)) \end{bmatrix} \tag{2.23}$$

where $A(\omega_i)$, $\varphi(\omega_i)$ are the magnitude, phase of $P(q)$ respectively.

2.6.3 The Gradient Repetitive Control Algorithm

The gradient RC algorithm was proposed in (Hätönen et al., 2006) and chooses

$$L(q) = \gamma P(q^{-1}) \tag{2.24}$$

where $P(q^{-1})$ is the adjoint of $P(q)$, and γ is the learning gain. This operator can be computed by first expressing $P(q)$ in FIR form

$$P(q) = \sum_{i=0}^{m_L} h_i q^{-i} \tag{2.25}$$

where h_i are the impulse response coefficients of plant $P(q)$. Then this is reversed in the temporal direction, so that

$$L(q) = \gamma \sum_{i=0}^{m_L} h_{m_L-i} z^{m_L-i} \,. \tag{2.26}$$

The reason for this choice of $L(q)$ is that $P(q^{-1})$ and $P(q)$ have the same amplitude response, but opposite phase response. Therefore, the phase of $P(e^{j\omega})$ and $L(e^{j\omega})$ in (2.17) is cancelled, and the LHS of (2.17) can be tuned by γ to satisfy the stability condition. The algorithm can only be applied to plants with impulse response lengths less than or equal to m_L. If the length of the impulse response exceeds m_L, design

methods can be used to reduce the length, so that the impulse response is 0 after m_L steps. These methods will be introduced later in this thesis.

2.6.4 The Optimal Repetitive Control Algorithm

Another common approach to designing $L(q)$ is termed 'Optimal RC' and was proposed in (Freeman et al., 2008). This method does not select $L(q)$ to directly satisfy stability condition (2.17) but instead selects $L(q)$ to implement optimal state-feedback around the series connection of the internal model and plant P. This therefore guarantees stability of the closed-loop system, satisfying the internal model principle. Since the system states are not directly measurable in general, $L(q)$ also embeds a state observer. The structure of the optimal RC is shown in the Figure 2.3 (Freeman et al., 2008).

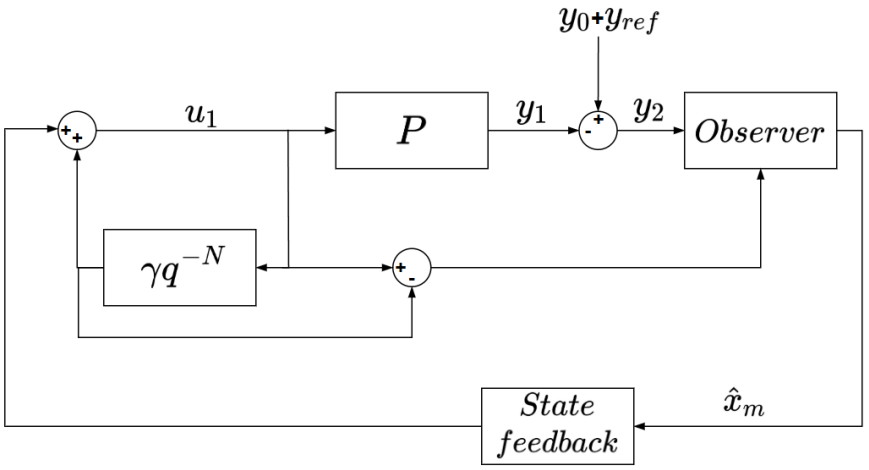

FIGURE 2.3: Optimal RC structure.

The design of the $L(q)$ of the optimal RC is more complicated than the above three algorithms. Define $u_F(k)$ as the output of state feedback controller,

$$\begin{aligned} u_F(k) + \gamma q^{-N} u_1(k) &= u_1(k) \\ u_F(k) &= (1 - \gamma q^{-N}) u_1(k) \end{aligned} \tag{2.27}$$

$$\begin{aligned} y_1(k) &= P(q) * u_1(k) \\ 0 - y_2(k) &= P(q) u_1(k) \\ -y_2(k) &= \frac{1}{1 - \gamma q^{-N}} P(q)(1 - \gamma q^{-N}) u_1(k) \\ y_2(k) &= \frac{-1}{1 - \gamma q^{-N}} P(q) u_F(k) \end{aligned} \tag{2.28}$$

The mathematical relationship between $u_F(k)$ and $y_2(k)$ is as follows:

$$y_2(k) = \frac{-1}{1 - \gamma q^{-N}} P(q) u_F(k) \tag{2.29}$$

Equation (2.29) can be divided into the series of two systems (Freeman et al., 2008):

$$u_M(k) = \frac{-1}{1-\gamma q^{-N}} u_F(k) \tag{2.30}$$

$$y_2(k) = P(q) u_M(k) \tag{2.31}$$

The state space equation of the system represented by Equation (2.30) is expressed as (Freeman et al., 2008):

$$\begin{aligned} x_1(k+1) &= A_1 x_1(k) + B_1 u_F(k) \\ u_M(k) &= -C_1 x_1(k) - u_F(k) \end{aligned} \tag{2.32}$$

Where

$$\begin{aligned} A_1 &= \begin{bmatrix} 0 & 0 & \cdots & 0 & 1 \\ 1 & 0 & \cdots & 0 & 0 \\ 0 & 1 & \cdots & 0 & 0 \\ \vdots & \ddots & \ddots & \ddots & \vdots \\ 0 & 0 & \cdots & 1 & 0 \end{bmatrix} \\ B_1 &= \begin{bmatrix} 1 & 0 & 0 & 0 & 0 & 0 \end{bmatrix}^T \\ C_1 &= \begin{bmatrix} 0 & 0 & 0 & 0 & 0 & 1 \end{bmatrix} \end{aligned} \tag{2.33}$$

The state space equation of the system represented by Equation (2.31) is expressed as (Freeman et al., 2008):

$$\begin{aligned} x_2(k+1) &= A_p x_2(k) + B_p u_M(k) \\ y_2(k) &= C_p x_2(k) \end{aligned} \tag{2.34}$$

Where A_p, B_p, C_p are the state space equation representation of $P(q)$ (Freeman et al., 2015). Combine the Equation (2.32) and Equation (2.34) to obtain (Freeman et al., 2008):

$$\begin{aligned} x_3(k+1) &= A_2 x_3(k) + B_2 u_F(k) \\ y_2(k) &= C_2 x_3(k) \end{aligned} \tag{2.35}$$

Where

$$x_3(k) = \begin{bmatrix} x_1(k) \\ x_2(k) \end{bmatrix}, A_2 = \begin{bmatrix} A_1 & 0 \\ -B_p C_1 & A_p \end{bmatrix}, B_2 = \begin{bmatrix} B_1 \\ -B_p \end{bmatrix} C_2 = \begin{bmatrix} 0 & C_p \end{bmatrix} \tag{2.36}$$

The method of stabilizing the optimal RC is different from the above three algorithms. It is not achieved by selecting parameters, but by minimizing the cost function J represented by Equation (2.37) (Freeman et al., 2015):

$$J = \sum_{i=1}^{\infty} x_3(i)^T C_2^T Q C_2 x_3(i) + u_F^T(i) R u_F(i) \tag{2.37}$$

Where Q and R are the symmetric positive definite matrices. The solution to minimize J is

$$u_F(k) = -Kx_3(k) \tag{2.38}$$

Where

$$K = (B_2^T S B_2 + R)^{-1} B_2 S A_2 \tag{2.39}$$

S is the solution of algebraic Riccati equation (ARE) represented by Equation (2.40):

$$S = A_2^T [S - S B_2 (B_2^T S B_2 + R)^{-1} B_2^T S] A_2 + C_2^T Q C_2 \tag{2.40}$$

x_3 may be unobservable, so an observer can be used to estimate x_3 (Freeman et al., 2008). According to Equation (2.35), a new state equation can be obtained (Freeman et al., 2015):

$$\hat{x_3}(k+1) = A_2 \hat{x_3}(k) + B_2 u_F(k) + L(y_2(k) - C_2 \hat{x_3}(k)) \tag{2.41}$$

Where $\hat{x_3}$ represents estimated x_3, L is the observer matrix. Combining (2.38) and (2.41) can obtain a new state space equation (Freeman et al., 2008):

$$\begin{aligned} x_3(k+1) &= A_F x_3(k) + B_F y_2(k) \\ u_F(k) &= C_F x_3(k) \end{aligned} \tag{2.42}$$

Where

$$A_F = A_2 - L C_2 - B_2 K,\ B_F = L,\ C_F = -K \tag{2.43}$$

Equation (2.42) is the state space equation representation of $L(q)$ of the optimal RC.

Optimal RC has been evaluated on tremor suppression in (Verstappen et al., 2012). Although it has a more complex structure than inverse and gradient RC, it only has a single tuning parameter which allows transparent design. However, the computational complexity of implementing the associated state observer and solving the ARE online presents a challenge for the real-time, potentially wearable systems required for FES therapy.

The two algorithms presented in this section—FMI-RC and gradient RC-were selected due to their historical significance and practical applicability in FES-based tremor suppression, as evidenced by their repeated use in prior studies (Copur, 2017; Copur et al., 2019; Zhang et al., 2022a,b). These methods represent the most widely adopted and experimentally validated RC designs in the biomedical control literature. Other RC design families—such as HORC or finite-dimensional RC (FDRC)—have been proposed in the broader control literature. However, they often impose structural assumptions on the uncertainty or require specific system properties, which limit their applicability to the highly unstructured and nonlinear uncertainty encountered in biomedical systems like the tremulous wrist. Therefore, these methods are not included in this section, as

the focus here is on general-purpose RC algorithms that are amenable to robustness analysis using the gap metric, as developed in the next chapter.

2.7 Repetitive Control Designed for Model Uncertainty

Given the model uncertainty present in all dynamical system representations, a fundamental research challenge lies in the development of stabilizing controllers for such systems. Existing literature has extensively explored the application of robust control frameworks within the context of repetitive control systems. The starting point is to define the system structure and constrain the uncertainty, and then derive a controller that keeps the system stable over the range of possible uncertainty.

Numerous approaches to design L and Q operators have been proposed in the RC literature. As explained in Section 2.6, they typically guarantee stability of the closed-loop error dynamics and convergence to zero, or a fixed error signal. However, the issue of robustness to model uncertainty has not been thoroughly analysed. In practice, plant model P will not exactly match the unknown true system (termed P^*) being controlled, and this is especially true in biomedical applications. Therefore, understanding the system robustness to model uncertainty is extremely important.

Model uncertainty can be classified into structured uncertainty and unstructured uncertainty (Bradley, 2010). Structured uncertainty is expressed in terms of the parameters used to define the plant model. This kind of uncertainty is also called parametric uncertainty. Although parametric uncertainty is simple to define, it also has the disadvantage of lacking consideration of unmodeled dynamics and therefore is not as realistic as other forms. The typical types of unstructured uncertainty are multiplicative uncertainty and additive uncertainty. For single-input single-output (SISO) systems, which are the focus of this work, these expressions simplify to $P^* = (I + \Delta)P$ for multiplicative uncertainty and $P^* = P + \Delta$ for additive uncertainty. In both cases, Δ represents dynamics that capture the unmodeled or erroneous part of the system. Both these forms of uncertainty are prescriptive in the sense that they impose a specific structure on how the model mismatch Δ relates to the nominal plant P. This structure limits the types of modeling errors they can represent. For instance, they are less suited for capturing general, nonlinear, and unstructured uncertainty.

A variety of RC designs have been proposed explicitly considering model uncertainty. The approach of (Hsu and Lin, 2013) combined μ control and RC to address multiplicative uncertainty. The design started with the introduction of a multiplicative uncertainty, and a weight matrix was used to specify the extent of the uncertainty. Then $L(q)$ was designed to stabilize the entire closed loop. However, the multiplicative

uncertainty was assumed to be linear and stable. The designed controller was also conservative, the tracking effect was very slow and poor, and there was still a large error after 250 seconds.

More recently, Dey et al. (2020) defined a multiplicative structured uncertainty using a weighting function and bounded stable perturbations. This modeling approach was capable of encompassing unmodeled dynamics and nonlinear factors. To address such uncertainties, the study proposed a HORC. The transfer function of HORC demonstrated that it enhanced system robustness against period mismatches and model disturbances by introducing multiple delay channels and weighting factors to accumulate historical error information. Simulation results showed that HORC outperformed conventional RC and FDRC in performance metrics, while closed-loop stability was validated through eigenvalue analysis. However, the method increased the system order, leading to structural complexity in the controller, which could elevate computational burdens and implementation challenges. Parameters such as weighting factors required careful tuning, as improper selection might compromise stability. Additionally, the research was based solely on simulations of linear time-invariant systems, leaving its effectiveness for highly nonlinear or time-varying systems in need of further verification.

Then Jiang et al. (2021) proposed a unified disturbance compensation framework under multiplicative uncertainty assumptions, employing an Equivalent-Input-Disturbance estimator to address both dynamic uncertainty and external disturbances without requiring precise plant models. However, its applicability was constrained by strict requirements placed on the nominal system (controllability, observability, and absence of imaginary-axis zeros) and lacked generalization to non-multiplicative uncertainty types.

At the same time, Gao et al. (2021) focused on a brushless DC motor, and categorized uncertainty into parametric (resistive parameters) and nonlinear (modeling errors and external load disturbance). The controller combined adaptive parameter estimation with a generalized reduced-order extended state observer for compensation. Practical limitations include the assumption of bounded nonlinear dynamics and susceptibility to sensor noise in speed and current measurements.

Finally, Chen et al. (2021) proposed an adaptive repetitive learning control scheme for permanent magnet synchronous motor servo systems with bounded nonparametric uncertainties. The method decomposed uncertainties into periodic and nonperiodic components. A key assumption was that the periodic part depended solely on the reference trajectory, which limited its applicability to cases where periodic disturbances were fully synchronized with the command. For the periodic part, a saturated repetitive learning law ensured continuous and bounded estimation. For the nonperiodic part, adaptive laws compensated without requiring prior knowledge of bounds. Lyapunov analysis proved the convergence of the tracking error, and experiments demonstrated improved accuracy and smoother control compared to existing methods.

All these robust RC methods constrain the underlying system dynamics, and impose structure on the uncertainty. These forms are highly restrictive since they do not capture the arbitrary, nonlinear, unstructured certainty found in real systems. Most research involved designing an RC update that stabilised an uncertain true plant, rather than providing a general procedure to analyse the robustness of a given RC update.

2.7.1 Repetitive Control Designed for Uncertainty in Disturbance Frequency

Other RC algorithms have focused on uncertainty disturbance frequencies rather than dynamics. Steinbuch et al. (2007) designed a HORC that combined cascaded delay lines with weighted historical periodic signals. Convex optimization was employed to adjust weighting parameters, balancing trade-offs between robustness to period-time uncertainty and suppression of intermediate-frequency noise. Frequency jitter uncertainty was addressed by defining shaping functions (e.g., low-pass or full-bandwidth filters) as optimization objectives. Linear programming minimized the $\mathcal{H}_\infty$ norm of the modified sensitivity function, achieving period-time robustness through alternating-sign weight sequences or noise reduction via monotonically decreasing weights. Experimental results on an optical storage CD tracking system showed effective periodic disturbance rejection under rotational frequency variations (± 0.05 Hz), though trade-offs existed: period-robust configurations amplified mid-frequency noise, while noise-robust versions sacrificed period robustness. Key limitations included reliance on accurate noise models, performance degradation from high-frequency modeling errors, unresolved stability issues in adaptive scenarios, and computational complexity in large-scale convex optimization.

Then Pipeleers et al. (2008) designed a high-order repetitive controller based on semidefinite programming (SDP), aiming to optimize the trade-off between robust performance under periodic input uncertainties and sensitivity to non-periodic inputs. The controller adjusted polynomial parameters $W(z)$ and incorporated low-pass filters $Q(z)$ combined with $L(z) = T_o^{-1}(z)$. Frequency uncertainties, modeled as relative frequency variations Δ covering intervals Ω_l, were transformed into linear matrix inequality constraints via the generalized KYP lemma, and globally optimal parameters were solved using SDP. Results demonstrated that the method generated trade-off curves, showing performance limits for different controller orders M and uncertainty levels Δ. It significantly outperformed traditional approaches under large uncertainties while reducing non-periodic performance degradation. Limitations included assumptions that all harmonics resided within the passband of $Q(z)$, restricting applicability in high-bandwidth systems; high memory requirements for implementing higher-order controllers; computational complexity dependent on SDP solvers; and exclusion of non-uniform probability distributions for uncertainties, potentially affecting robustness assessments.

2.8 Tolerance of Uncertainty in RC Algorithms

The previous approaches developed methods to stabilise uncertainty plants. A different approach is to take an established RC algorithm and examine how much modelling error can be tolerated and it still converge.

Freeman et al. (2008) designed a discrete-time repetitive controller. By constructing an augmented state-space model and solving the algebraic Riccati equation for optimal feedback gains, asymptotic convergence was guaranteed. For unmeasurable states, a state observer was developed, while a relaxation parameter γ balanced convergence speed and robustness. In robustness analysis, the article derived phase and gain uncertainty bounds using the Nyquist criterion and frequency-domain methods. A zero-phase filter was introduced to suppress high-frequency noise and model uncertainties, with experimental validation on a nonminimum-phase spring-mass-damper system confirming stable long-term tracking despite nonlinearities or modeling errors. The limitations of this research were that the nominal plant had to be linear and multiplicative, with high computational complexity and model dependence.

In recent years, Freeman (2017) proposed a multiple model switched RC framework, where robustness was guaranteed through gap metric analysis. Specifically, the controller design involved three steps: first, embedding the conventional RC structure into a 'lifted domain' to segment time-domain signals into periodic sequences; second, constructing a set of candidate linear time-invariant plant models to cover the possible uncertainty range of the true plant; and finally, dynamically switching to the RC controller corresponding to the model best matching the current observations via Kalman filter-based residual estimation.

The study utilized the gap metric to quantify model discrepancies and began by proposing an important theorem for conventional linear time-invariant (LTI) RC. This stated that, if the gap metric between the true plant and the nominal model was smaller than a threshold determined by the closed-loop gain (b_{P_p,C_c}), the closed-loop LTI RC system remained stable and convergent. This result was used to specify a ball of plant that are stabilised by a conventional RC algorithm, with a radius of b_{P_p,C_c}.

Conditions were then derived for the multiple model switched RC framework to stabilise a much larger plant uncertainty region specified by the designer. This involved specifying how close the plant models were spaced out. Unfortunately there were key limitations: Firstly, the framework assumed the plant was LTI which limited its applicability to nonlinear systems. Secondly, the design process required extremely complex calculations that would be difficult to satisfy in practice. Thirdly, the results were conservative, specifying a huge number of models and controllers, even for a simple numerical example. Finally, no experimental results were provided to validate the approach's practicality.

Despite these limitations, (Freeman, 2017) is the only RC framework that can stabilise an arbitrary uncertainty region, and the only one to use the powerful gap metric which encompasses unstructured model uncertainty. Consequently, the following chapter will summarise this method and attempt to develop a framework for robust RC design.

2.9 Summary

Tremor affects millions of people worldwide, but conventional treatments have numerous limitations. FES-based tremor suppression technology has shown great potential but conventional control schemes have limited performance. RC can theoretically provide ideal suppression and has been demonstrated in many studies. However it also has issues associated with robustness, set-up time and interference with voluntary effort. This motivates undertaking a thorough review of the basic principles and robustness analysis of RC.

Then the structure of RC and the conditions required for convergence and causality are summarized. The key components are the learning operator L and the robustness filter Q. These must be chosen to satisfy the convergence condition, and it is clear how the Q filter assists with this while also impairing tracking performance. The existing robust RC designs were investigated, which revealed a lack of appropriate analytical tools to systematically guide robust RC design practices.

Given the progress made using the powerful gap metric approach, the next chapter will apply gap metric analysis to guide the subsequent RC design.

Chapter 3

Robust Stability and Robust Repetitive Control Design

The last chapter provided a background to RC. Based on these findings, this chapter defines the current tools that have been used to study its robust stability. In particular, focus is on the gap metric, due to its applicability to unstructured uncertainty. Then these concepts will be used to develop a principled procedure to enable the RC designer to trade convergence, tracking accuracy and robustness. Following this, the structure will be expanded to tackle the case in which a conventional feedback controller is added in combination with RC. A new, updated, design procedure is then generalised to exploit the extra flexibility this delivers. The design procedures are then applied to a realistic model of the tremulous wrist in order to verify its effectiveness. Applying the procedure will also reveal the limitations of the conventional RC algorithms that have so far been employed for tremor suppression.

3.1 Robust Stability

The first step to defining a 'robust stability margin' for RC is to introduce the concept of 'gain stability' as follows.

3.1.1 Gain Stability

Recall the general form of closed-loop feedback system of Figure 2.1. Define $w_i = (u_i, y_i)^\top$ to represent the external disturbances ($i = 0$), the plant signals ($i = 1$) and controller signals ($i = 2$). Finally, denote $\bar{w_0} = (u_{dis}, y_{ref})^\top$ as the external bias signals. Then the operator that maps the external signals to the internal plant signals can be defined as the projection operator

$$\Pi_{P//C} : (w_0 + \bar{w_0}) \mapsto w_1 \tag{3.1}$$

and, from relations (2.4), is given by

$$\Pi_{P//C} = \begin{pmatrix} I \\ P \end{pmatrix} (I + CP)^{-1} \begin{pmatrix} I, C \end{pmatrix} . \tag{3.2}$$

This provides a measure of robust stability for the closed loop system which was introduced in (Georgiou and Smith, 1997). Assuming for simplicity that P and C are both linear, this measure is defined as follows.

Definition 3.1. The closed-loop linear system in Figure 2.1 is said to be 'gain stable' with respect to the external bias $\bar{w_0}$ if there exists a scalar $0 < M < \infty$ such that

$$\left\| \Pi_{P//C} \right\|_\infty < M . \tag{3.3}$$

Gain stability means that bounded external disturbances give rise to bounded plant and control signals. Using this measure of stability, a general robustness metric can now be summarised.

3.1.2 The Gap Metric and Robust Stability

Suppose the true plant is denoted P^* and differs from the model P used for control design. In this case the controller C designed to control P may not stabilise P^*. To investigate this, it is first necessary to measure the difference between the two plants. This can be achieved using the gap metric, denoted $\delta(P, P^*)$, which mathematically describes the 'distance' between the two plants P and P^* and was introduced in (Zames and El-Sakkary, 1981).

Defining the gap first requires the notion of the graph of the system P. This is denoted $\mathcal{M}_\mathbf{P}$ and comprises the set of all bounded input and output signals compatible with P, e.g. for a SISO plant with input $u_1 \in l^2$, the graph is

$$\mathcal{M}_P := \left\{ \omega \in l^2 \times l^2 \quad | \quad \omega = (u_1, P_p u_1) \right\}. \tag{3.4}$$

The graph of P^* is defined similarly, and denoted $\mathcal{M}_{\mathbf{P}^*}$. Then the directed gap is defined as

$$\vec{\delta}(P, P^*) := \sup_{\omega \in \mathcal{M}_P, \omega \neq 0} \inf_{v \in \mathcal{M}_{P^*}} \frac{\|\omega - v\|}{\|\omega\|}. \tag{3.5}$$

This is interpreted as: for every signal pair in $\mathcal{M}_{\mathbf{P}}$, find the distance to the nearest signal pair in $\mathcal{M}_{\mathbf{P}^*}$. Then take the largest of these distances. A metric must be symmetrical in P_P and P_{P^*}, and therefore the gap is taken as the largest directed gap between the two systems, i.e.

$$\delta(P, P^*) := \max\{\vec{\delta}(P^*, P), \vec{\delta}(P, P^*)\}. \tag{3.6}$$

The gap can be easily computed for linear systems, but is often computationally expensive for nonlinear systems.

Using this measure, the following theorem from (Georgiou and Smith, 1997) provides a sufficient condition for stability of the closed-loop connection of P^* and C, denoted $[P^*, C]$.

Theorem 3.2. *Assume that linear controller C satisfies Definition 3.1 (i.e. it stabilises the linear plant P). Suppose controller C is applied to another linear plant P^*. If*

$$\delta(P, P^*) < \left\|\Pi_{P//C}\right\|_\infty^{-1}, \tag{3.7}$$

then the closed-loop system $[P^*, C]$ is stable.

Theorem 3.2 states that the gap metric between plant P^* and plant P must be less than $\left\|\Pi_{P//C}\right\|_\infty^{-1}$ to ensure that the closed-loop system is still stable. Therefore, if the value of $\left\|\Pi_{P//C}\right\|_\infty^{-1}$ is small, the gap metric between the plant P^* and P must be small, i.e. the controller C can only stabilize plants that are close to the original plant P.

Therefore, $\left\|\Pi_{P//C}\right\|_\infty^{-1}$ can be used to measure the 'ball' of plants that are stabilised about P, as shown in Figure 3.1. As in (Georgiou and Smith, 1990), the radius of this ball (i.e. the robust stability margin) can be defined by

$$b_{P,C} = \left\|\Pi_{P//C}\right\|_\infty^{-1} \tag{3.8}$$

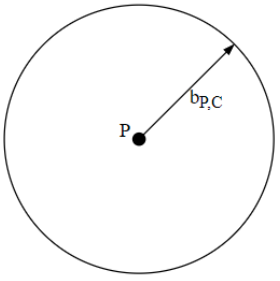

FIGURE 3.1: Ball of plants in uncertainty space U that are stabilised by controller C.

3.1.3 Robust Stability of Repetitive Control

To apply the previous robustness results to RC involves computing operator $\Pi_{P//C}$, given by (3.2). The terms on the bottom have already been computed in (2.12). The remaining two terms can readily be computed using

$$\begin{aligned} u_1(k) =& \frac{Q(q)L(q)}{q^N - Q(q)(I - P(q)L(q))}(y_{ref}(k) + y_0(k)) \\ &+ \frac{q^N - Q(q)}{q^N - Q(q)(I - P(q)L(q))}(u_{dis}(k) + u_0(k)) \ . \end{aligned} \tag{3.9}$$

It can be seen that all four terms of $\Pi_{P//C}$ share identical poles which are the solutions to (2.15). It follows that, if stability criterion (2.16) or (2.17) holds and $P(q)$ is stable, then all four terms will be stable. The operator $\Pi_{P//C}$ is then stable and therefore $\left\|\Pi_{P//C}\right\|_\infty$ is bounded above. Applying Definition 3.1 and Theorem 3.2 then leads to the following result.

Theorem 3.3. *Suppose the standard RC update (2.2) is designed for a stable plant model $P(q)$ such that (2.16) or (2.17) hold. Then the resultant closed-loop system is gain stable and has a robust stability margin $b_{P,C}$.*

This is an important result as it establishes the amount of modeling uncertainty that RC can tolerate and remain stable.

3.2 Repetitive Control Design Procedure

After introducing how to quantitatively measure the robustness of the system, the concepts contained in last section will now be further developed in order to produce a practical design procedure that allows the designer to transparently trade convergence and robustness. The design procedures presented in this chapter build upon existing RC design methods, such as those summarized in (Longman, 2010), which focus on selecting $L(q)$ and $Q(q)$ to satisfy the convergence condition (2.17). The original contribution of this section is the integration of the robust stability margin $b_{P,C}$ into the design process. This allows the designer to quantitatively evaluate the system's robustness to unstructured model uncertainty, a feature not included in previous design procedures. The robust stability margin is used in Steps 4 of Design Procedure 1 and 5 of Design Procedure 2 to guide the selection of $L(q)$ and $Q(q)$ parameters. Specifically, the designer can tune the parameters of $L(q)$ and $Q(q)$ to increase $b_{P,C}$, thereby enhancing robustness, while ensuring that the convergence condition (2.17) is satisfied. This provides a method to trade off convergence speed and tracking accuracy against robustness to model uncertainty.

The first stage of any model-based control design is to identify the plant model P, and a suitable procedure was proposed in (Copur, 2017) for the current application of tremor suppression. This procedure also identifies the period, T, of the tremor. In most previous papers this has been assumed to equal a fixed value, however in practice the period may slowly vary or there may be more than one period. This issue will be addressed later in the thesis, but for now a fixed period is assumed. The number of samples $N = \frac{T}{T_s}$, where T_s is the sampling frequency, then defines the period of disturbance u_{dis} which models the tremor. The reference y_{ref} is set to zero, since this corresponds to ideal tremor suppression.

Having specified the plant model and task parameters, the components $L(q)$ and $Q(q)$ of RC update (2.5) must be selected. This is done by inspecting the LHS term of convergence condition (2.17), which is given by

$$\left|Q(e^{j\omega})(I - P(e^{j\omega})L(e^{j\omega}))\right| \ . \tag{3.10}$$

Chapter 2 showed this term affects both the convergence rate and the converged tracking error. In particular, for each frequency $\omega \in [0, 2\pi]$

- the amplitude of (3.10) dictates the convergence rate, with values closest to zero producing faster convergence (and values over one leading to divergence)
- the amplitude of $Q(e^{j\omega})$ dictates whether convergence to zero tracking error will be achieved, with values closer to one producing lowest error.

Clearly the designer could select $L(q)$ as the inverse RC update (2.21) together with a value of $Q(q) = I$ and thereby achieve maximum convergence speed to zero error at all frequencies. However, this RC update is known to be highly sensitive to plant uncertainty. It is therefore necessary to also consider the robust stability margin $b_{P,C}$ given by (3.2) and (3.8). For greatest robustness, $b_{P,C}$ must be as large as possible. In general, the size of $b_{P,C}$ correlates inversely with the size of (3.10) and also with the norm of $Q(q)L(q)$. This can be seen by inspection of the components of $\Pi_{P//C}$ shown in (2.12) and (3.9).

The above discussion motivates the following design process:

- First select the range of frequencies over which suppression is required. As a minimum, this must capture the fundamental tremor frequency $\frac{1}{T}$, however a slightly larger value would be sensible to include higher harmonics present in the tremor.
- Then $L(q)$ should be selected to achieve rapid convergence over this range of frequencies (termed the 'suppression range'). This can be done by plotting $\left|I - P(e^{j\omega})L(e^{j\omega})\right|$ and ensuring it is close to zero over the suppression range.

- Then $Q(q)$ should be selected as a low-pass zero-phase filter with a sharp cut-off immediately above the suppression range. This filter must have an amplitude of unity over the pass-band to ensure complete tremor suppression, but then should remove higher frequencies. The filter then results in making $\left|Q(e^{j\omega})(I - P(e^{j\omega})L(e^{j\omega}))\right|$ small over all frequencies. Additionally, it has the effect of minimising the norm of $Q(q)L(q)$, thereby increasing $b_{P,C}$. It hence maximises robustness, without causing any deterioration to tremor suppression.

In practice there are trade-offs present in this design procedure since a sharp cut-off for $Q(q)$ will generally extend the length m_Q of its impulse response. This means that the length constraint (2.11) may be difficult to achieve. It may therefore be necessary to reduce the order of the filter, which reduces the sharpness of the cut-off. To address this, the cut-off frequency then may need to be increased to ensure a unity amplitude over the required bandwidth. This will generally lead to a larger $Q(q)L(q)$ and slightly reduced robustness.

The overall design procedure is summarised in Design Procedure 1.

Design Procedure 1 Repetitive control design without feedback controller

Require: Model of plant P, tremor period length N.
Ensure: $m_Q + m_L \leqslant N$.

1: Decide on the suppression range according to the frequencies present in the tremor.
2: Calculate $L(q)$ using an appropriate RC algorithm. The parameters of $L(q)$ should be tuned to minimize the LHS of (2.17) over the suppression range (with $Q(q)$ omitted) to achieve fast convergence. Record the length of $L(q)$, denoted m_L.
3: Design the Q filter. Set the cut-off frequency as the maximum frequency in the suppression range, and design the Q filter to have a flat passband and a sharp cut-off. Try to ensure that the LHS of (2.17) is reduced as much as possible over all frequencies.
4: Compute $b_{P,C}$ to quantitatively evaluate the robustness of the system. If the system is not sufficiently robust (or if $m_Q + m_L \leqslant N$ is not satisfied), return to the Step 2 to retune the parameters or return to Step 3 to retune the filter cut-off frequency to enhance robustness. The robust stability margin provides a direct measure to guide this trade-off between performance and robustness.

3.3 Repetitive Control with Inner Feedback Loop

The above procedure may not deliver a satisfactory solution due to the constraint $m_Q + m_L \leqslant N$. This is because when the tremor frequency increases, the number of samples in each period, $N = \frac{T}{T_s}$, will decrease. Meanwhile, the impulse response of $L(q)$, denoted m_L, is fixed and may be relatively large. In particular, it is often of a similar length as the impulse response of plant model $P(q)$, and in the case of gradient RC, the two lengths are identical (2.24). In (Copur, 2017) for example, the impulse response of

$P(q)$ lasted approximately 0.6 seconds, which therefore restricts the possible tremor frequency to 1.67 Hz, even without adding a filter $Q(q)$. If a 4 Hz tremor needs to be suppressed, m_L has to be reduced, which necessitates truncating $L(q)$. However, this will inevitably produce poor tremor suppression performance, and may not even satisfy stability condition (2.17).

An obvious solution to this problem is to introduce a feedback controller, as demonstrated in (Copur, 2017). From the perspective of the repetitive controller, the resulting plant feedback loop can be regarded as a new plant. The length of the impulse response of this new plant can be reduced by tuning the feedback controller until the corresponding $L(q)$ meets the constraint $m_Q + m_L \leqslant N$. Another potential advantage is that the feedback controller may also be able to provide better suppression performance in the first few cycles of repetitive control or when repetitive control is not applied.

3.3.1 Closed-Loop Feedback Control System

The previous convergence conditions and robustness results must be updated for the new control structure. The proposed arrangement is shown in Figure 3.2 where K represents a general feedback control operator.

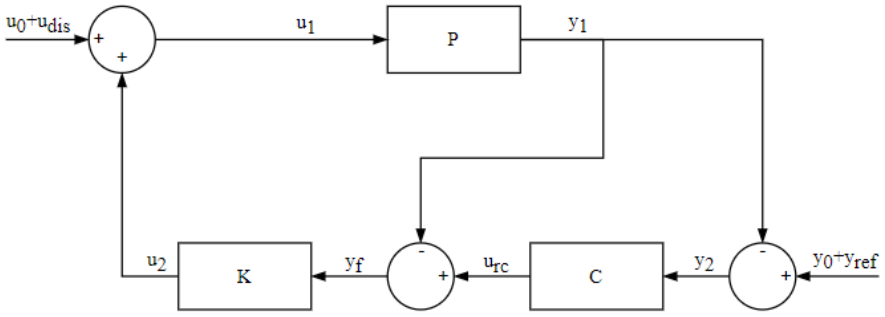

FIGURE 3.2: Closed-loop system with additional feedback controller.

Here y_f is the input of the feedback controller, and u_{rc} is the output of the repetitive controller. As previously stated, the feedback loop composed of K and P can be regarded as a new plant from the perspective of the RC design. This is more clearly shown in Figure 3.3 which has identical connections but the position of K has been rearranged.

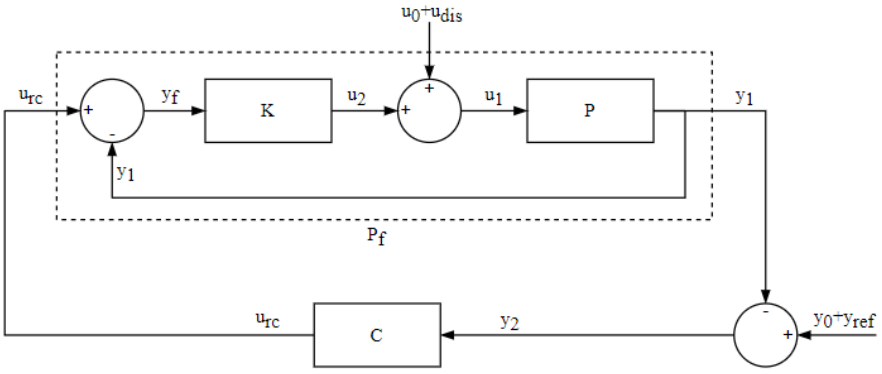

FIGURE 3.3: Closed-loop system with additional feedback controller after rearrangement.

Comparing this layout with the original one of Figure 2.1 it is clear that P has been replaced by the new plant

$$P_f(q) = \frac{y_1(k)}{u_{rc}(k)} = \frac{P(q)K(q)}{I + P(q)K(q)} \tag{3.11}$$

but the position of external input $u_0 + u_{dis}$ now does not occur in front of this new plant. This means it is not possible to simply substitute $P(q)$ for $P_f(q)$ in the robustness results of Chapter 2. Conceptually this is because the new arrangement is impossible to implement as it has been assumed that the controller cannot directly measure the plant output signal y_1.

3.3.2 A Realisable Structure

To place the control scheme in the form of Figure 2.1, it is necessary to introduce a new noise input, denoted v_0, as shown in Figure 3.4.

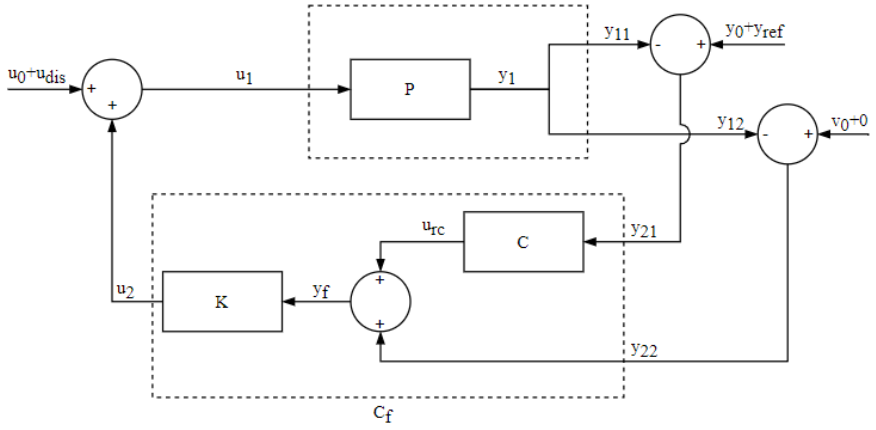

FIGURE 3.4: Realizable closed-loop system with additional feedback controller.

The addition of v_0 has enabled the system to exactly match the required form of Figure 2.1. The substitutions are that C is replaced by (KC, K), P is replaced by $(P, P)^\top$, y_1 is replaced by $(y_{11}, y_{12})^\top$, and y_{ref} is replaced by $(y_{ref}, 0)^\top$. When $v_0 = 0$, Figure 3.4 is identical to Figure 3.2. Robustness conditions derived for the former will always hold for the latter structure.

3.3.3 Convergence Conditions of the New Structure

Ignoring noise, the closed-loop plant output can be obtained from inspection of Figure 3.4 as

$$\begin{aligned} y_1(k) =& \frac{P(q)K(q)Q(q)L(q)}{q^N - Q(q) + P(q)K(q)(Q(q)L(q) + q^N - Q(q))} y_{ref}(k) \\ &+ \frac{P(q)(q^N - Q(q))}{q^N - Q(q) + P(q)K(q)(Q(q)L(q) + q^N - Q(q))} u_{dis}(k) \\ =& \frac{P(q)K(q)Q(q)L(q)y_{ref}(k) + P(q)(q^N - Q(q))u_{dis}(k)}{q^N - Q(q) + P(q)K(q)(Q(q)L(q) + q^N - Q(q))} \end{aligned} \tag{3.12}$$

whose poles are the N solutions to

$$\begin{aligned} q^N &= Q(q)\left(I - \frac{P(q)K(q)L(q)}{I + P(q)K(q)}\right) \\ &= Q(q)(I - P_f(q)L(q)) \, . \end{aligned} \tag{3.13}$$

This is identical to the previous characteristic equation (2.15), except that P is replaced with P_f. Therefore, with the new feedback controller added, the RC convergence conditions are also the same as those derived in Section 2.6.1 but with P replaced with P_f, that is

$$\left\| Q(q)(I - P_f(q)L(q)) \right\|_\infty < 1 \tag{3.14}$$

and

$$\sup_{\omega \in [0, 2\pi]} \left| Q(e^{j\omega})(I - P_f(e^{j\omega})L(e^{j\omega})) \right| < 1 \, . \tag{3.15}$$

3.3.4 Robust Stability Margin of the New Structure

To compute the robust stability margin for the new structure, first substitute the new operator forms into (2.4) to give

$$\begin{pmatrix} u_1 \\ y_{11} \\ y_{12} \end{pmatrix} = \begin{pmatrix} I \\ P \\ P \end{pmatrix} (I + K(C + I)P)^{-1} \begin{pmatrix} I & KC & K \end{pmatrix} \begin{pmatrix} u_0 + u_{dis} \\ y_0 + y_{ref} \\ v_0 \end{pmatrix} \tag{3.16}$$

so that the projection operator $\Pi_{P//C}$ for the new structure is

$$\Pi_{P//C} = \begin{pmatrix} I \\ P \\ P \end{pmatrix} (I + K(C+I)P)^{-1} \begin{pmatrix} I & KC & K \end{pmatrix} . \tag{3.17}$$

This enables gain margin $b_{P,C}$ to be calculated for the new system using (2.6), (3.8) and (3.17). However, (3.17) does not reveal the relative contributions from the feedback controller and the RC action to the robustness of the system. To show this contribution, $\Pi_{P//C}$ can be split up using the relation

$$(I + K(C+I)P)^{-1} = (I + KP)^{-1} - P_f C(I + K(C+I)P)^{-1} \tag{3.18}$$

to become

$$\begin{aligned} \Pi_{P//C} = &\begin{pmatrix} I \\ P \\ P \end{pmatrix} (I + KP)^{-1} \begin{pmatrix} I & 0 & K \end{pmatrix} + \begin{pmatrix} I \\ P \\ P \end{pmatrix} (I + KP)^{-1} \begin{pmatrix} 0 & KC & 0 \end{pmatrix} \\ &- \begin{pmatrix} I \\ P \\ P \end{pmatrix} P_f C \, (I + K(C+I)P)^{-1} \begin{pmatrix} I & KC & K \end{pmatrix} . \end{aligned} \tag{3.19}$$

From (3.11), $P(q) = P_f(q)K(I - P_f(q))^{-1}$ which can be substituted into (3.19) to give

$$\begin{aligned} \Pi_{P//C} = &\underbrace{\begin{pmatrix} I \\ P \\ P \end{pmatrix} (I + KP)^{-1} \begin{pmatrix} I & 0 & K \end{pmatrix}}_{\Pi_{P//K}} \\ &+ \underbrace{\begin{pmatrix} I \\ P \\ P \end{pmatrix} C \, (I - P_f) \, (I + CP_f)^{-1} \begin{pmatrix} -P_f & K & -P_f K \end{pmatrix}}_{\Pi_{P_f//C}} . \end{aligned} \tag{3.20}$$

The first term on the RHS of (3.20) is the projection operator corresponding purely to the feedback connection of plant $P(q)$ and controller $K(q)$, i.e. if RC were removed. It is therefore termed $\Pi_{P//K}$. The second term on the RHS of (3.20) is the additional component due to the repetitive controller and is called $\Pi_{P_f//C}$. Because the robust stability margin $b_{P,C}$ is the reciprocal of the infinity norm of $\Pi_{P//C}$, (3.20) demonstrates the relative contributions from the feedback controller and the repetitive controller to the overall robustness in this system, i.e. $\left\|\Pi_{P//C}\right\|_\infty \leq \left\|\Pi_{P//K}\right\|_\infty + \left\|\Pi_{P_f//C}\right\|_\infty$. This means that when one controller is enhanced, the other controller must be weakened to maintain the robustness of the closed loop system.

3.3.5 Gain Stability of the New Structure

Following the structure of Chapter 2, the next task is to examine the plant input relation

$$\begin{aligned} u_1(k) =& \frac{K(q)C(q)(q^N - Q(q))}{q^N - Q(q) + P(q)K(q)(Q(q)L(q) + q^N - Q(q))}(y_{ref}(k) + y_0(k)) \\ &+ \frac{q^N - Q(q)}{q^N - Q(q) + P(q)K(q)(Q(q)L(q) + q^N - Q(q))}(u_{dis}(k) + u_0(k)) \\ =& \frac{K(q)C(q)(q^N - Q(q))y_{ref}(k) + (q^N - Q(q))u_{dis}(k)}{q^N - Q(q) + P(q)K(q)(Q(q)L(q) + q^N - Q(q))} \, . \end{aligned} \tag{3.21}$$

It can be seen that the poles of the transfer function relating u_1 to the external signals are the same as for output relation (3.12). Therefore, if convergence condition (3.14) holds and $P(q)$ is stable, then all components of $\Pi_{P//C}$ are stable and hence $\left\|\Pi_{P//C}\right\|_\infty$ is bounded. Then, according to Definition 3.1, the closed-loop system is gain stable. Therefore, the new feedback controller structure of Figure 3.4 also satisfies Theorem 3.3 and has a robust stability margin.

3.3.6 Repetitive Control Design Procedure with Feedback Controller

The inclusion of the feedback controller means that the design procedure of Section 3.2 must be updated. In particular, it requires an additional step in which $K(q)$ is selected to produce a closed-loop system $P_f(q)$ which has an impulse response length less than that of $P(q)$. The next RC design step is unchanged, but RC operator $L(q)$ must be designed for system $P_f(q)$ rather than $P(q)$. The subsequent filter design step is also unchanged, but frequency condition (2.17) is replaced by (3.15). The final step is also unchanged, but the designer must return to the new initial step (design of $K(q)$).

With these modifications, the updated design procedure is summarised as follows:

Design Procedure 2 Repetitive control design with additional feedback controller

Require: Model of plant P, tremor period length N.

Ensure: $m_Q + m_L \leqslant N$.

1: Decide on the suppression range according to the frequencies present in the tremor.

2: Design $K(q)$ to reduce the impulse response length and increase the closed-loop bandwidth so that it includes the suppression range determined in Step 1.

3: Calculate $L(q)$ using a desired RC algorithm. The parameters of $L(q)$ should be tuned to minimize the LHS of (3.15) over the suppression range to achieve fast convergence. Record the length of $L(q)$ and denote as m_L.

4: Design the Q filter. Set the cut-off frequency as the maximum frequency in the suppression range, and design the Q filter to have a flat passband and a sharp cut-off. Try to ensure that the LHS of (3.15) is reduced as much as possible.

5: Compute $b_{P,C}$ to quantitatively evaluate the robustness of the system. If the system is not robust enough (or if $m_Q + m_L \leqslant N$ is not satisfied), return to Step 2 to retune $K(q)$, return to Step 3 to retune $L(q)$, or return to Step 4 to retune the filter cut-off frequency. The robust stability margin enables the designer to make informed decisions when trading convergence performance against robustness to model uncertainty.

3.4 Application of Robust Design Procedure

To validate the design procedures proposed in Section 3.2 and Section 3.3, this section applies them to a wrist model. The objective is to demonstrate their feasibility and to expose the robustness limitations of conventional RC schemes.

3.4.1 Establishment of an Idealized Wrist Model

Section 2.4.2 summarized existing RC applications to tremor supression, which included (Copur et al., 2019; Freeman et al., 2015; Verstappen et al., 2012; Zhang et al., 2022b). Based on clinical need, these applied FES to two muscles in the wrist called Flexor Capri Radialis (FCR) and Extensor Carpi Radialis (ECR) to control the angle of the wrist. These papers modelled each muscle as a series combination of a static nonlinearity and linear dynamics. The static nonlinearity represents the static isometric recruitment curve (IRC) and the linear dynamics comprises the linear activation dynamics (LAD) of the muscle. These forms capture the nonlinear recruitment of muscle fibres and subsequent generation of force. The combined output of the two muscles drives the rigid body dynamics (RBD) of the joint and connective tissue, denoted H_{RBD}, as illustrated in Figure 3.5a). Here $h_{IRC,fcr}$, $h_{IRC,ecr}$ and H_{LAD} are the IRC and LAD components respectively.

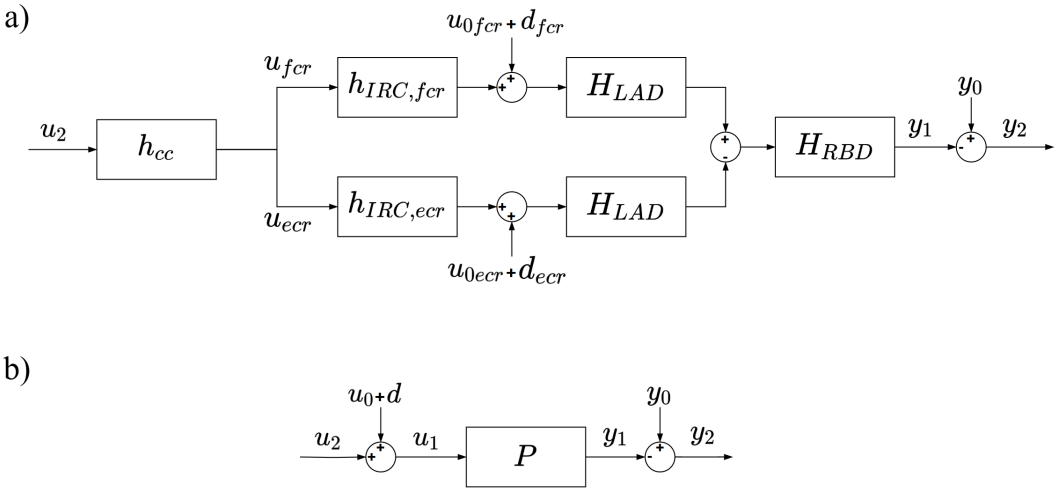

FIGURE 3.5: a) Biomechanical wrist model with coactivation function h_{cc}, b) equivalent wrist model P.

Both $h_{IRC,fcr}$ and $h_{IRC,ecr}$ are increasing functions, and their output becomes zero when inputs are negative. Since the h_{IRC} blocks are only defined for positive inputs, a coactivation function h_{cc} is introduced to divide the control signal u_2 between the FCR and ECR muscle inputs. This enables bidirectional movement and prevents both muscles working against each other. This function maps u_2 to the FES stimulation inputs (u_{fcr}, u_{ecr}) applied to the respective muscles. It is given by (3.22) and illustrated in Figure 3.6a) (Freeman et al., 2015).

$$
\begin{aligned}
h_{cc}(u_2) &= (u_{fcr}, u_{ecr}) : \\
u_{fcr} &= \begin{cases} u_2 + \bar{u}_{fcr} & \text{if } u_2 \in [0, u_{max} - \bar{u}_{fcr}] \\ \bar{u}_{fcr} & \text{if } u_2 \in [\bar{u}_{ecr} - u_{max}, 0] \end{cases} \\
u_{ecr} &= \begin{cases} \bar{u}_{ecr} & \text{if } u_2 \in [0, u_{max} - \bar{u}_{fcr}] \\ \bar{u}_{ecr} - u_2 & \text{if } u_2 \in [\bar{u}_{ecr} - u_{max}, 0] \end{cases}
\end{aligned}
\tag{3.22}
$$

where u_{max} is the maximal stimulation pulsewidth, $\bar{u}_{fcr}$, $\bar{u}_{ecr} \geq 0$ are fixed coactivation levels that satisfy the balance condition $h_{IRC,fcr}(\bar{u}_{fcr}) = h_{IRC,ecr}(\bar{u}_{ecr})$.

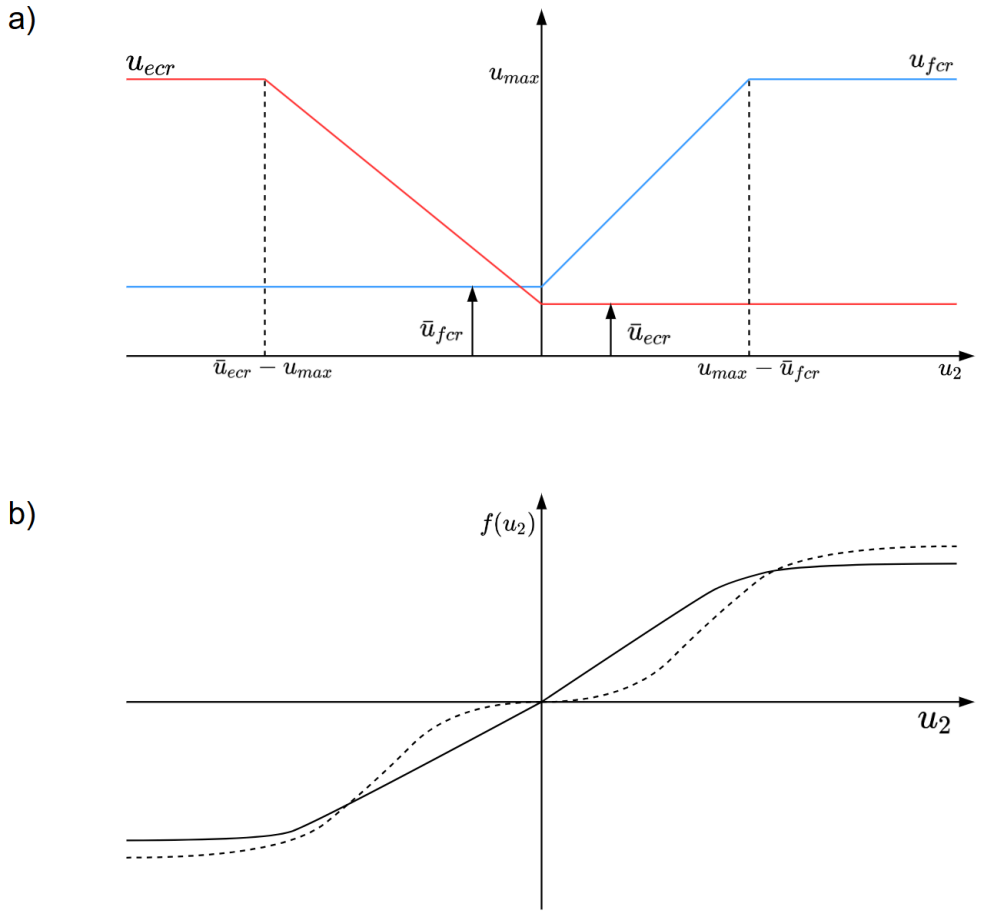

FIGURE 3.6: a) Coactivation mapping h_{cc} with levels $\bar{u}_{fcr}$, $\bar{u}_{ecr}$. b) $f(u_2)$ for cases: zero coactivation ($\bar{u}_{fcr}, \bar{u}_{ecr} = 0$) [dashed line], and non-zero coactivation [solid line].

An additional feature of the co-activation function is that it removes the dead zone that exists in the IRC. The nonlinear part composed of h_{cc} and IRC is defined as $f(u_2) = h_{IRC,fcr}(h_{cc}(u_2)) - h_{IRC,ecr}(h_{cc}(u_2))$, which is illustrated in Figure 3.6b). When the coactivation levels are appropriately selected, the dead zone in the original dashed line is removed and transformed into a continuous, monotonically increasing increasing solid line. This results in the IRC being approximated as a gain c over a certain range of FES.

In tremor suppression study, the disturbance signal is the tremor, and the reference signal is set to zero. The effect of tremor acting on the FCR and ECR muscles is modelled by periodic signals d_{fcr} and d_{ecr} respectively, whose period is the reciprocal of the tremor frequency. For multiple tremor frequencies, they contain the sum of the periodic signals for each frequency. Terms u_{0fcr} and u_{0ecr} represent unknown process noise. It is assumed that similar muscle groups have similar dynamics, H_{LAD}. The LAD and RBD dynamic components were assumed to take a linear form in all previous tremor studies. The signal y_0 denotes unknown measurement noise affecting the wrist angle y_1. Based on the preceding definitions and assumptions, the model in Figure 3.5a)

is simplified to Figure 3.5b), where $P = c \cdot H_{LAD} \cdot H_{RBD}$, $u_0 = u_{0fcr} + u_{0ecr}$, and $d = d_{fcr} + d_{ecr}$. Signal d is the overall periodic disturbance representing the tremor.

When the standard RC structure from Figure 2.1 is implemented on the model in Figure 3.5b), the resulting new system is shown in Figure 3.7. Here G and R represent the linear plant operator and the repetitive controller operator, respectively. The resulting SISO system simplifies the RC design and fits exactly with the structure of Figure 2.1 in Section 2.5.

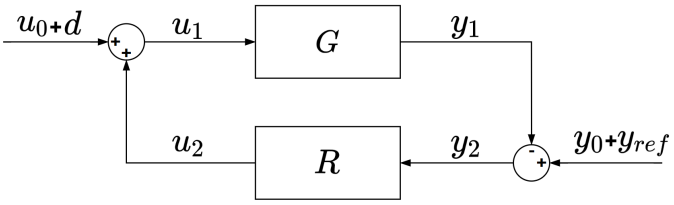

FIGURE 3.7: Linear closed-loop system.

3.4.1.1 Parametrised Wrist Model

Numerous forms exist for the increasing function h_{IRC} and for the first or second order linear dynamics H_{LAD}, and are reviewed in (Le et al., 2010). The linear dynamics can be accurately modeled as a critically damped second order system (Freeman et al., 2009). Consequently, the linear wrist dynamics employed in (Verstappen et al., 2012; Freeman et al., 2015) is given by

$$P(s) = c \cdot \frac{\omega_n^2}{s^2 + 2s\omega_n + \omega_n^2} \cdot \frac{1}{I_p s^2 + bs + k_p} \tag{3.23}$$

where s is the Laplace variable, c is the gain representing the IRC, ω_n is the natural frequency. The second transfer function represents RBD, I_p represents inertia, b represents damping and k_p represents stiffness. Parameters selected from (Copur, 2017) and (Peaden and Charles, 2014), are given in the second column of Table 3.1, where c_o, ω_n, I_{po}, b_o and k_{po} are the original data used to build the model.

Parameter	Modeling data	Variation Range	Unit
c	$c_o = 4.5887$	0.45887-13.7661	–
ω_n	$\omega_{no} = 9.4248$	0.94248-28.2744	rad/s
I_p	$I_{po} = 0.00164$	0.000164-0.00492	$kg \cdot m^2$
b	$b_o = 0.0300$	0.0030-0.0900	$Nm \cdot s/rad$
k_p	$k_{po} = 0.713$	0.0713-2.139	Nm/rad

TABLE 3.1: Values of wrist model parameters.

Applying the second column of Table 3.1 to transfer function (3.23) results in the plant model

$$P(s) = \frac{407.6}{0.00164s^4 + 0.06091s^3 + 1.424s^2 + 16.1s + 63.33} \,. \tag{3.24}$$

The robustness of existing RC schemes in studying parameter uncertainty and time-varying dynamics deserves to be examined. To establish the limitations of these schemes, it is therefore necessary to apply them within the design procedures of Chapter 3 using realistic ranges of model uncertainty. To quantify the range of possible parameter variation, data from muscle fatigue tests and spasticity tests in (Brend, 2014) and (Cha and Arami, 2020) will be used. According to these studies, the range of parameter variation has been added to Table 3.1.

In addition, the tremor considered in (Verstappen et al., 2012; Freeman et al., 2015; Copur et al., 2019) is usually intention tremor, which has a frequency less than 5 Hz. Therefore, the range of tremor frequency in the following experiments is 0 to 5 Hz.

3.5 Application of Design Procedure 1

3.5.1 Design Rationale for RC Algorithm Selection

This section and next section apply the robust design procedures from Chapter 3 to a wrist model, employing two distinct RC algorithms: FMI-RC in Design Procedure 1 and gradient RC in Design Procedure 2. The rationale for this selection is based on the inherent characteristics, assumptions, and advantages of each algorithm, which make them suitable for different design scenarios.

FMI-RC is an approximation of the ideal inverse RC. Its primary advantage is that it aims to minimize $\|I - P(q)L(q)\|_\infty$ over a specified frequency range, which, according to the stability condition in (2.17), leads to fast convergence and high performance within that range. However, this performance is achieved under the assumption of a relatively accurate plant model. It is inherently less robust to significant model uncertainty. Therefore, FMI-RC was selected for Design Procedure 1, which deals with the standard control structure without an additional feedback loop. This scenario represents a baseline case where the potential for high performance is prioritized, and the plant dynamics are not intentionally altered.

3.5.2 Decide on the Suppression Range

The tremor frequency is assumed to be 2 Hz. The sampling interval $T_s = 0.005$ s. The suppression range is set to 0 to 5 Hz as described in Section 3.4.1. The tremor period is $T = \frac{1}{2} = 0.5$ s. Since $T_s = 0.005\,s$, $N = \frac{T}{T_s} = 100$.

3.5.3 Design $L(q)$ to Accelerate the Convergence

Using (2.23) and the plant given by (3.24), $L(q)$ can be calculated. $L(q)$ can be changed by tuning m_L and n_L, thus affecting the convergence. Temporarily set $Q(q) = I$, $n_L = 0$, and plot the stability conditions with different m_L as shown in Figure 3.8.

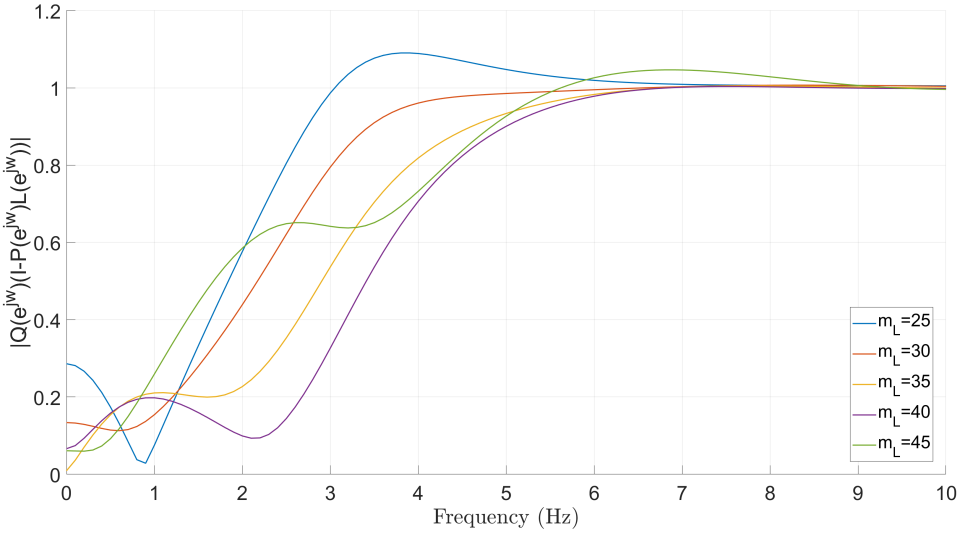

FIGURE 3.8: Stability conditions with different m_L ($Q(q) = I, n_L = 0$).

When m_L is low or high, the system may have poles outside the unit circle. When $m_L = 40$, not only is the stability condition satisfied, but the convergence rate is fast for most frequencies in the suppression range. The next step is to set $m_L = 40$ and plot the stability conditions with different n_L as shown in Figure 3.9.

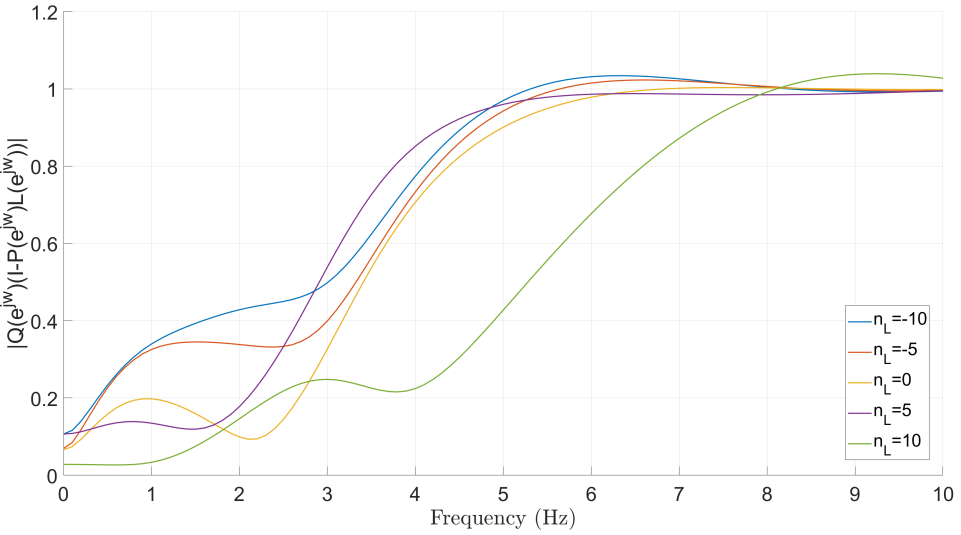

FIGURE 3.9: Stability conditions with different n_L ($Q(q) = I, m_L = 40$).

It can be seen that the stability condition is satisfied when $n_L = 0$, and the convergence of most frequencies within the suppression range is faster. Therefore, m_L and n_L are selected at 40 and 0 respectively.

3.5.4 Design Q Filter to Satisfy the Stability Condition

As the Q filter is a zero-phase low-pass filter, it can be obtained by convolving a low-pass filter with a low-pass filter which has the opposite phase. The cut-off frequency is set to 5 Hz. Note that m_Q should not exceed $N - m_L = 100 - 40 = 60$, i.e. the impulse response length of the low-pass filter cannot exceed $60 \cdot T_s = 0.3$ s. Figure 3.10 shows the impulse responses of several low-pass filters with a cut-off frequency of 5 Hz and different orders.

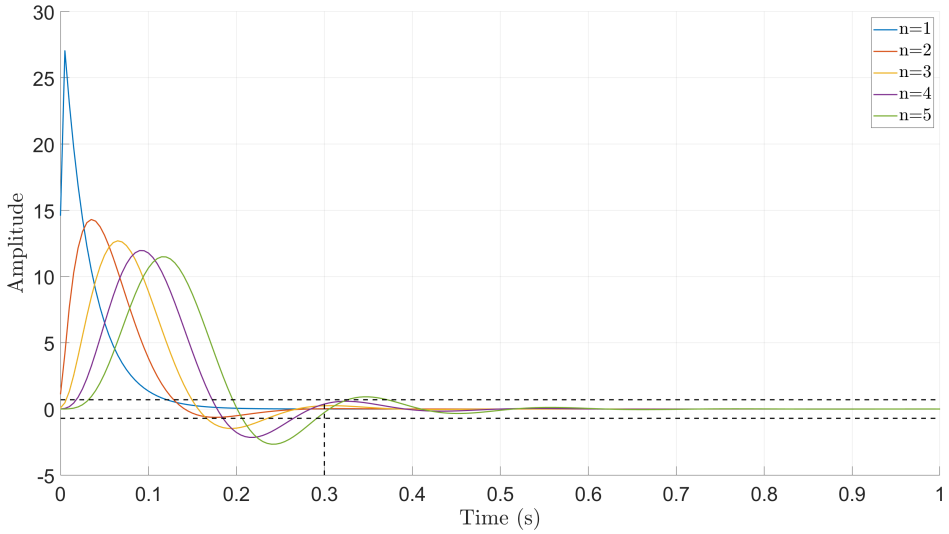

FIGURE 3.10: The impulse response of the low-pass filter with different n ($f_c = 5$ Hz).

From Figure 3.10, the length of the impulse response of the low-pass filter with order $n \leq 4$ is within 0.3 s. Figure 3.11 shows the amplitude response of $Q(q)$ plotted with different n.

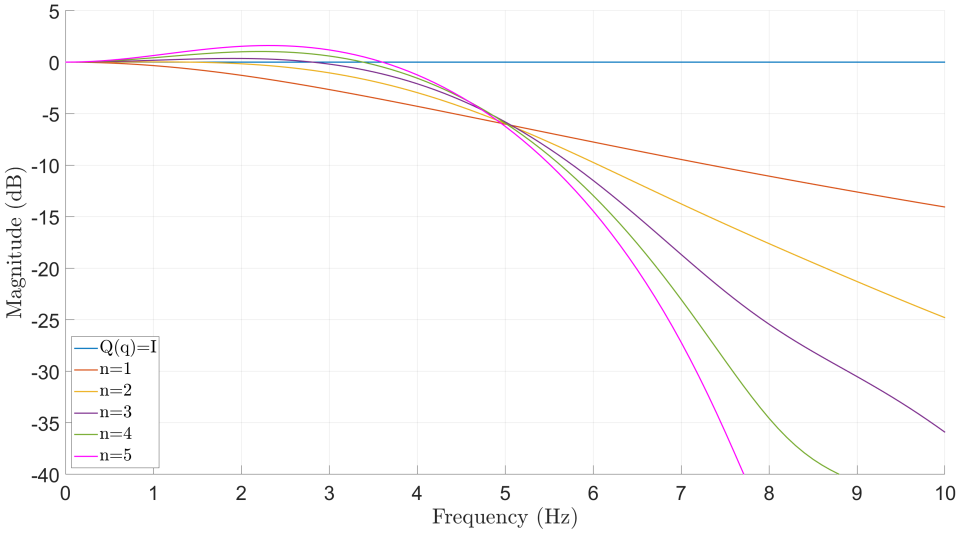

FIGURE 3.11: The amplitude response of the Q filter with different n ($f_c = 5$ Hz).

It is then necessary to plot $\left|Q(e^{j\omega})(I - P(e^{j\omega})L(e^{j\omega}))\right|$ to check if the Q filter satisfies the stability condition.

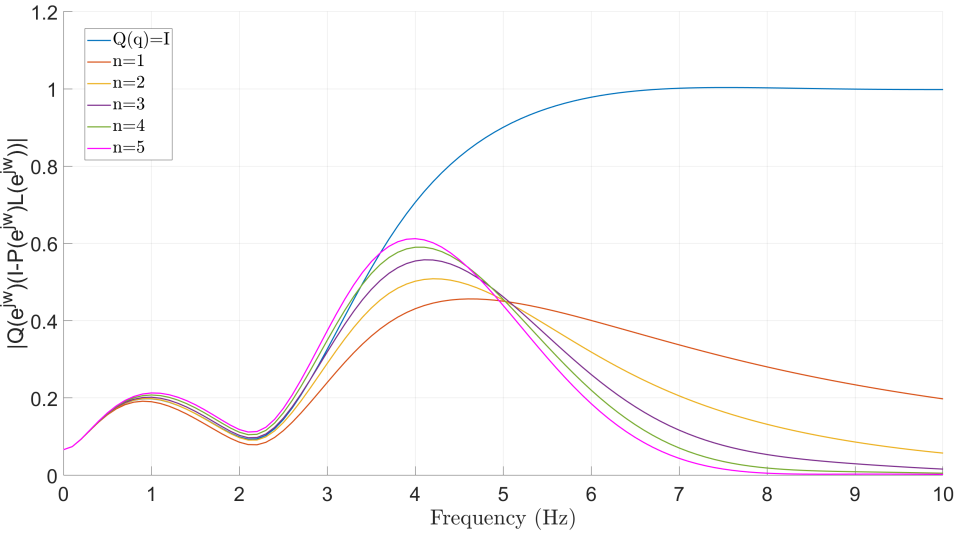

FIGURE 3.12: Stability conditions with different n ($f_c = 5$ Hz).

Figure 3.12 demonstrates that the variation of the convergence rate in the suppression range is not significant due to the different filter orders. In contrast, when the order is $n = 3$, the passband is flatter than when $n = 1, 2, 4$, and the edge is sharper than when $n = 1, 2$. Therefore $n = 3$ and $f_c = 5$ Hz are suitable parameters.

3.5.5 Robustness of the FMI-RC to Parametric Uncertainty

The next step is to introduce parametric uncertainty to check whether the controller is sufficiently robust. To better quantify the tremor suppression performance of the controller, the performance index is defined as

$$\text{performance index} = \begin{cases} 1 - \frac{\|y_c\|}{\|y\|} & \text{if } 1 - \frac{\|y_c\|}{\|y\|} \geqslant 0 \\ 0 & \text{if } 1 - \frac{\|y_c\|}{\|y\|} < 0 \end{cases} \tag{3.25}$$

where $\|y_c\|$ represents the 2-norm of all wrist angular movements under the control of RC, and $\|y\|$ represents the 2-norm of all wrist angular movements without RC control.

- If the tremor is not well suppressed, $1 - \frac{\|y_c\|}{\|y\|}$ is close to 0. In this case, the performance index is close to 0.
- If the tremor is well suppressed, $1 - \frac{\|y_c\|}{\|y\|}$ is close to 1. In this case, the performance index is close to 1.
- If the unstable output tends to infinity, $1 - \frac{\|y_c\|}{\|y\|}$ is a negative number. In this case, the performance index is 0.

The designed repetitive controller is now applied to plants with different b and k_p values. The variation range of b and k_p are shown in Table 3.1, from 10% to 300% of their original values b_o and k_{po}. Figure 3.13 shows the performance index of each test. The blue point represents the original plant P. When k_p is below 50% of k_{po}, the performance indices of most tests are close to 0, indicating that the repetitive controller cannot stabilize the system.

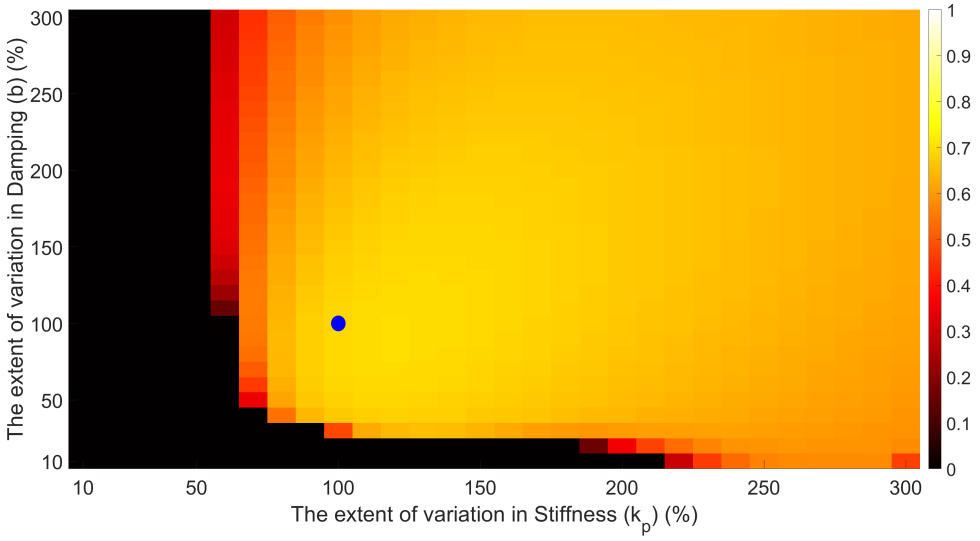

FIGURE 3.13: Performance index of FMI-RC with different b, k_p.

Using (3.2) and (3.8), $b_{P,C} = 0.0896$, Figure 3.14 shows the stability condition and gap metric for each plant with different b and k_p values. If the stability condition is satisfied, it is shown in yellow. If the gap metric between true plant and original plant does not exceed 0.0896, it is shown in cyan. Those that neither satisfy the stability conditions nor remain within the robust stability margin are shown in dark blue. Comparing Figure 3.14 and Figure 3.13, it is clear that the robust stability margin is conservative.

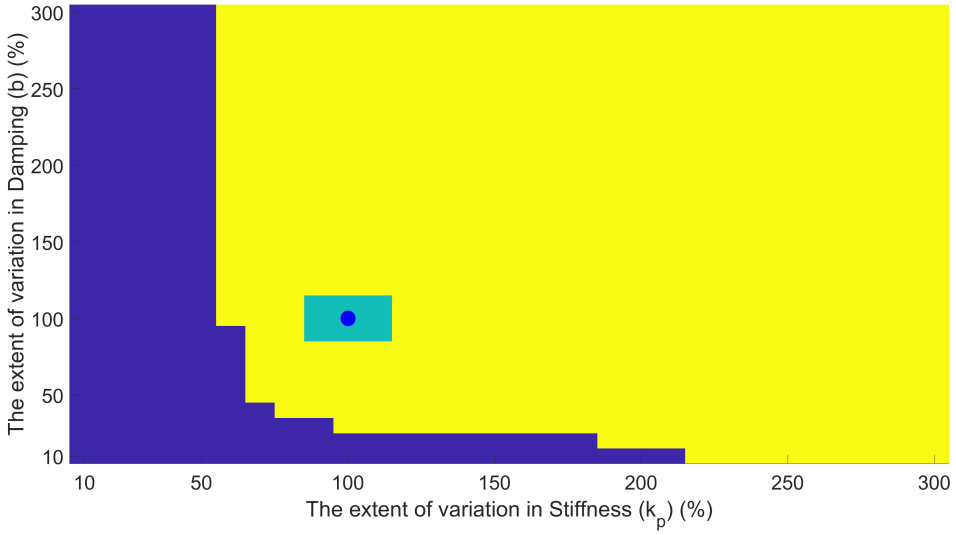

FIGURE 3.14: Stability condition and gap metric of FMI-RC with different b, k_p.

The variation range of I_p and w_n are shown in Table 3.1, from 10% to 300% of their original value I_{po} and w_{no}. The designed repetitive controller is then applied to plant with different I_p and w_n values. Figure 3.15 shows the performance index of each test. The designed repetitive controller cannot stabilize the system for a large range of w_n.

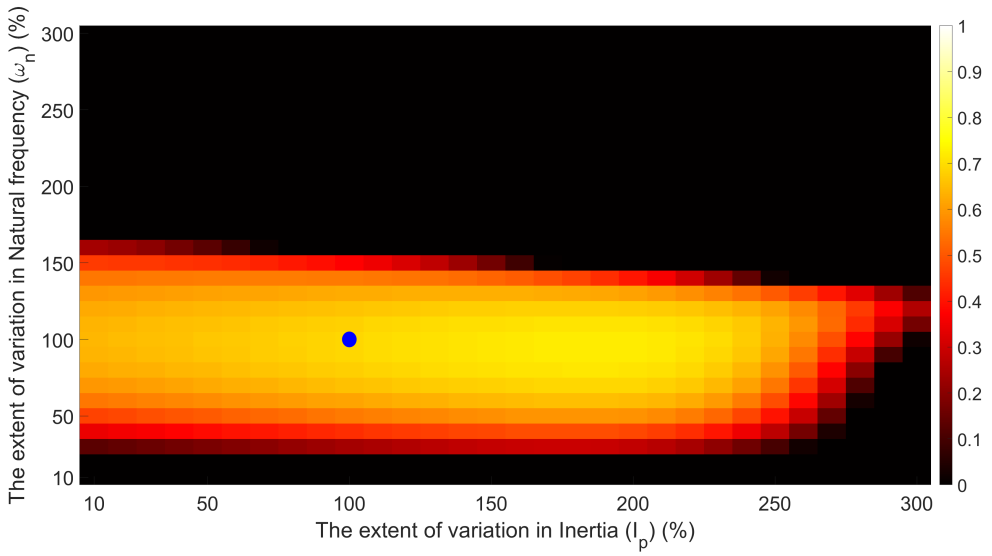

FIGURE 3.15: Performance index of FMI-RC of FMI-RC with different I_p, w_n.

Figure 3.16 shows the stability condition and gap metric for each plant with different I_p and w_n values. It again demonstrates that the robust stability margin is conservative.

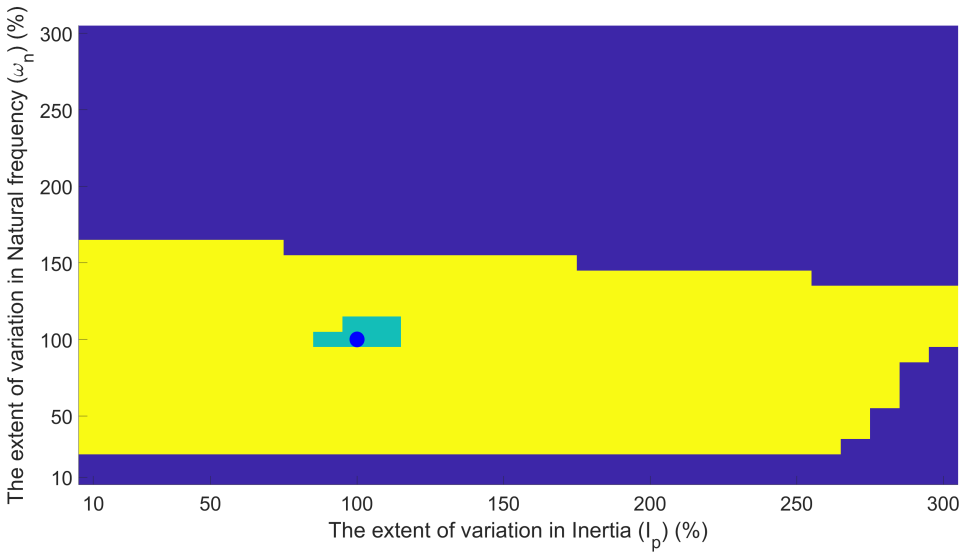

FIGURE 3.16: Stability condition and gap metric of FMI-RC with different I_p, w_n.

The variation range of c are shown in Table 3.1, from 10% to 300% of their original value c_o. The designed controller was then applied to plants with different values of c, yielding the results shown in Figure 3.17. The performance index (blue solid line with circles) shows the performance index. If the performance index curve is close to 0, it means that the system is unstable, otherwise, if it is close to 1, it means that the tremor is well suppressed. The stability condition (red dashed line with squares) indicates theoretical stability. The gap metric (black dash-dot line with diamonds) measures the distance to the nominal model. When the stability condition and the gap metric curve approach 1, it means that the system does not satisfy the stability condition and exceeds the robust stability margin. When the two curves approach 0, it means that the system satisfies the stability condition, and the gap metric between the true plant and the original model is in the robust stability margin. Figure 3.17 shows that the stability conditions are satisfied in the range of $c = 10\%c_o$ to $c = 160\%c_o$, and the system is stable when stability condition is satisfied. However, the system lacks robustness to models with c above $170\%c_o$. In addition, the gap metric is still conservative. It shows that the system is stable only when the difference between true plant and the original model is small.

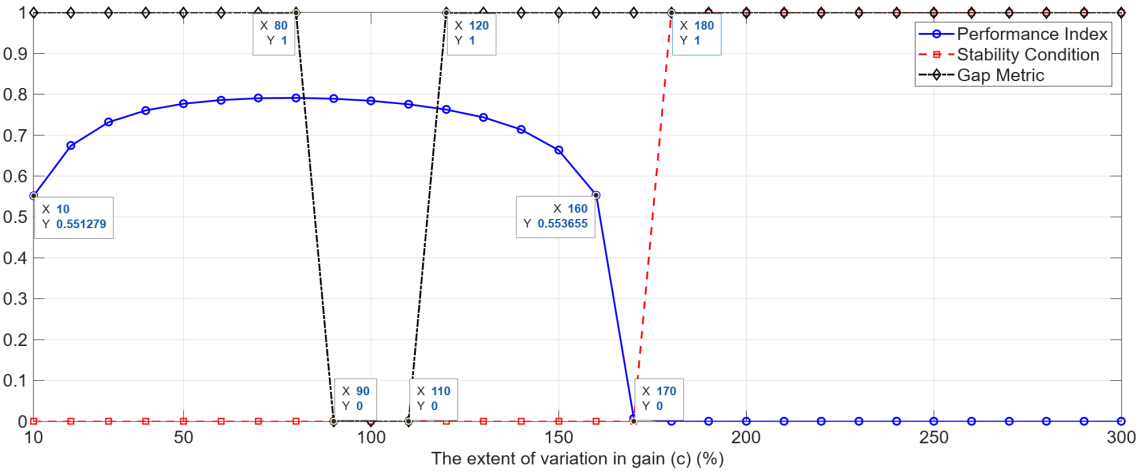

FIGURE 3.17: Performance index, stability condition and gap metric of FMI-RC with different c.

Varying the frequency of the tremor and applying the designed controller, the calculated performance index is plotted in Figure 3.18. When the frequency of the tremor varies, the controller can only suppress the tremor within a small range centered around 2 Hz, and a portion of the tremor around the second harmonic at 4 Hz. This demonstrates that the designed controller with only a single internal model has poor robustness to changing frequencies.

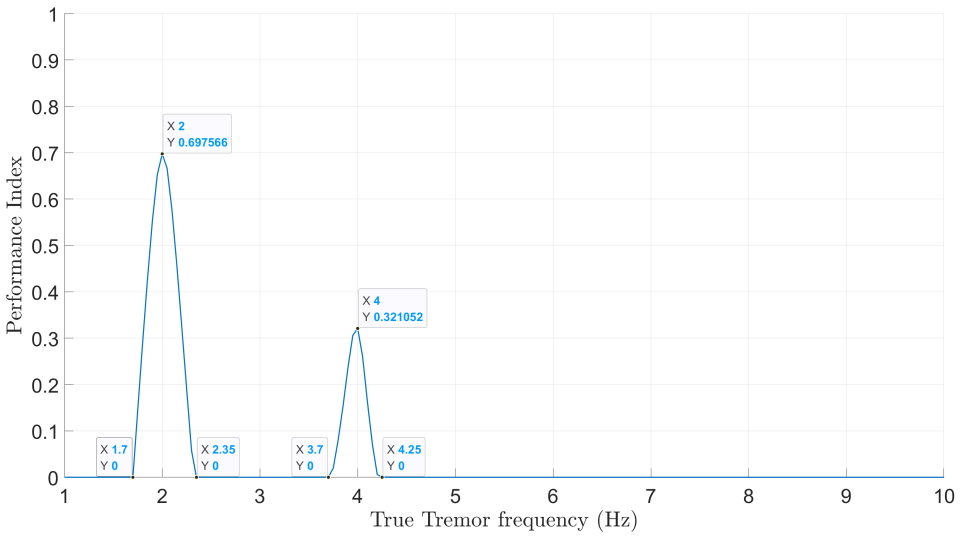

FIGURE 3.18: Performance index of FMI-RC with different f.

3.6 Application of Design Procedure 2

3.6.1 Design Rationale for RC Algorithm Selection

Gradient RC takes a different approach. It uses the adjoint of the plant model, which cancels the phase of the plant in the frequency domain. Its primary advantage is enhanced robustness. The tuning parameter, the learning gain, provides a straightforward mechanism to satisfy the stability condition without relying on a precise plant inverse. This makes it more suitable for situations where model uncertainty is higher or when the plant dynamics are modified. Consequently, the gradient RC algorithm was chosen for Design Procedure 2, which incorporates an additional feedback controller. As mentioned in Section 3.2.3 and Section 4.3, the application of gradient RC may require introducing an additional feedback controller to reduce the impulse response length of the plant. Furthermore, the introduced feedback controller also creates a new controlled plant. The robustness of gradient RC is beneficial for managing the increased complexity and potential uncertainty associated with this modified system.

3.6.2 Decide on the Suppression Range

In this section, gradient RC is used to design the controller. The tremor frequency is assumed to be 1.25 Hz. The sampling interval $T_s = 0.005$ s. The suppression range is set from 0 to 2.5 Hz. The tremor period is $T = \frac{1}{1.25} = 0.8$ s. Since $T_s = 0.005\,s$, $N = \frac{T}{T_s} = 160$. However, the plant impulse response approaches 0 at about 0.63 s. Ignoring the length m_Q of the Q filter, $N \geqslant m_L = \frac{0.63}{T_s} = 126$, resulting in the maximum suppression frequency $f_{max} = \frac{1}{T} = \frac{1}{N \times T_s} \approx 1.59$ Hz. This does not include 2.5 Hz. So an additional feedback controller needs to be introduced and therefore design procedure 2 is applied.

3.6.3 Design $K(q)$ to Improve the Suppression Range to Include Tremor Frequency f

A proportional controller is employed as the additional feedback controller and therefore

$$K(q) = K_p \tag{3.26}$$

where K_p is a proportional gain. The length of the IR of the original plant P and P_f varying with K_p is shown in Figure 3.19. The amplitude of all impulse responses is normalized.

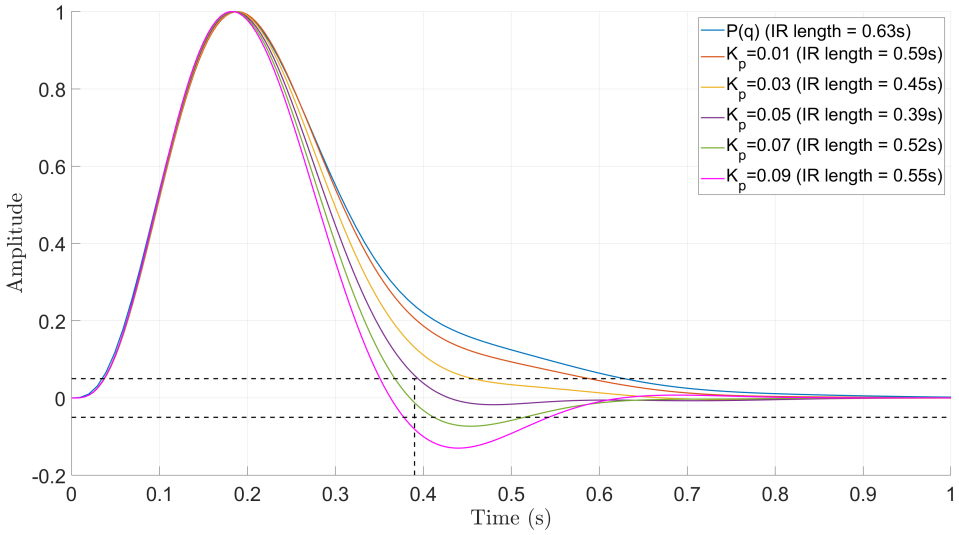

FIGURE 3.19: The impulse response of P and P_f with different K_p.

When $K_p = 0.05$, the IR reaches the minimum length of 0.39 s, resulting in $f_{max} = \frac{1}{0.39} \approx 2.57$ Hz. The suppressed frequency is included in this range.

3.6.4 Design $L(q)$ to Accelerate the Convergence

Using (2.24) and the plant given by (3.24), $L(q)$ can be calculated. The value of the learning gain γ is computed by temporarily setting $Q(q)$ to I. Substituting (2.24) into (2.17), the range of γ is as follows

$$0 < \gamma < \frac{2}{\sup_{\omega \in [0,2\pi]} |P(e^{j\omega})|^2} . \tag{3.27}$$

Hence the maximum learning gain γ_{max} is calculated as 33.25. Setting 0 to 30 as the range of γ produces the stability condition curves shown in Figure 3.20.

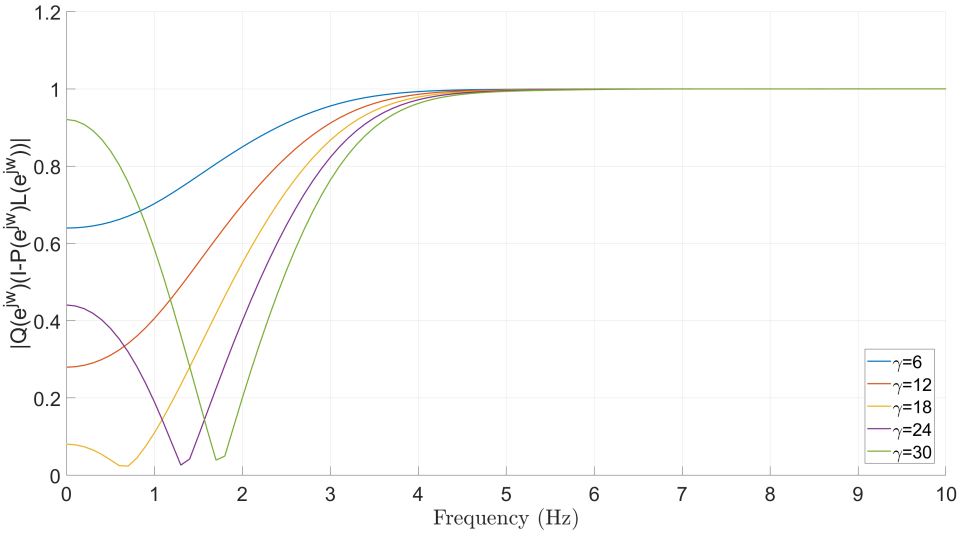

FIGURE 3.20: Stability conditions with different γ ($Q(q) = I$).

In the suppression range 0 to 2 Hz, the curve with $\gamma = 18$ is lowest. This suggests using $\gamma = 18$.

3.6.5 Design Q Filter to Satisfy the Stability Condition

The cut-off frequency is set to 2.5 Hz. Note that m_Q should not exceed $N - m_L = 160 - \frac{0.39}{T_s} = 82$, i.e. the impulse response length of the low-pass filter must not exceed $82 \cdot T_s = 0.41$ s. The impulse responses of low-pass filters with a cut-off frequency of 2.5 Hz and different orders are plotted in Figure 3.21.

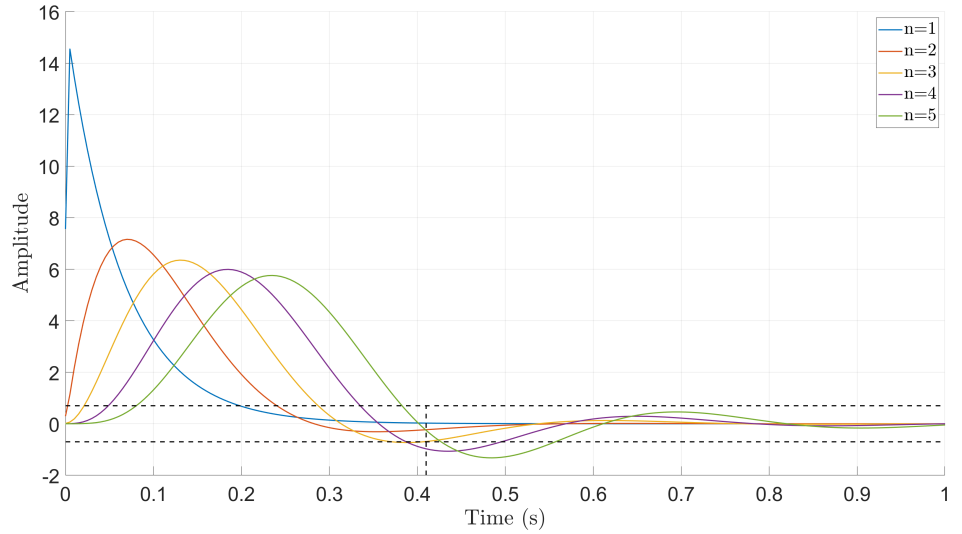

FIGURE 3.21: The impulse response of the low-pass filter with different n ($f_c = 2.5$ Hz).

Figure 3.21 shows that the impulse response length of the low-pass filter with order $n \leq 3$ is within 0.41 s. The amplitude response of $Q(q)$ with different n is plotted in Figure 3.22.

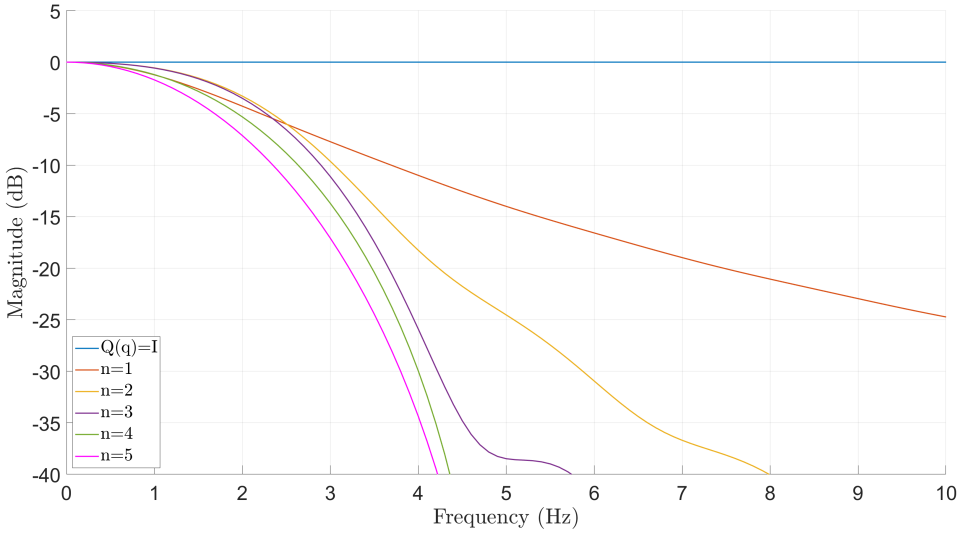

FIGURE 3.22: The amplitude response of the Q filter with different n ($f_c = 2.5$ Hz).

The convergence rate $\left|Q(e^{j\omega})(I - P(e^{j\omega})L(e^{j\omega}))\right|$ is plotted in Figure 3.23 to check if the Q filter satisfies the stability condition.

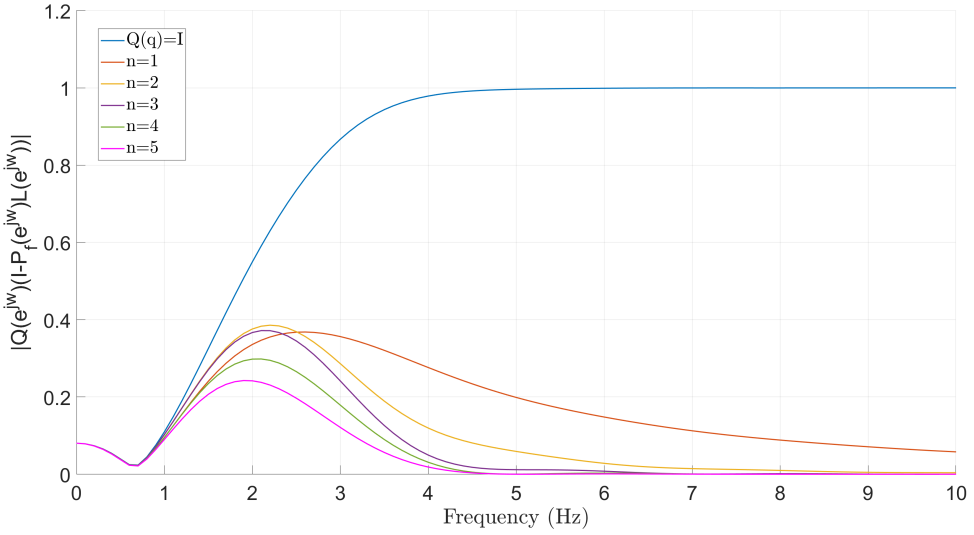

FIGURE 3.23: Stability conditions with different n ($f_c = 2.5$ Hz).

Figure 3.23 demonstrated that the variation of the stability condition in the suppression range is not significant due to the different order. In contrast, when $n = 3$, the passband is flat and the edges are sharper than those of the $n = 1, 2$. Therefore $n = 3$ and $f_c = 2.5$ Hz are suitable parameters.

3.6.6 Robustness of the Gradient RC to Parametric Uncertainty

The next step is to introduce parametric uncertainty to examine controller robustness. The designed repetitive controller is now applied to plants with different b and k_p values. Figure 3.24 shows the performance index of each test. When k_p is below 40% of the original value k_{po}, the designed repetitive controller cannot stabilize the system.

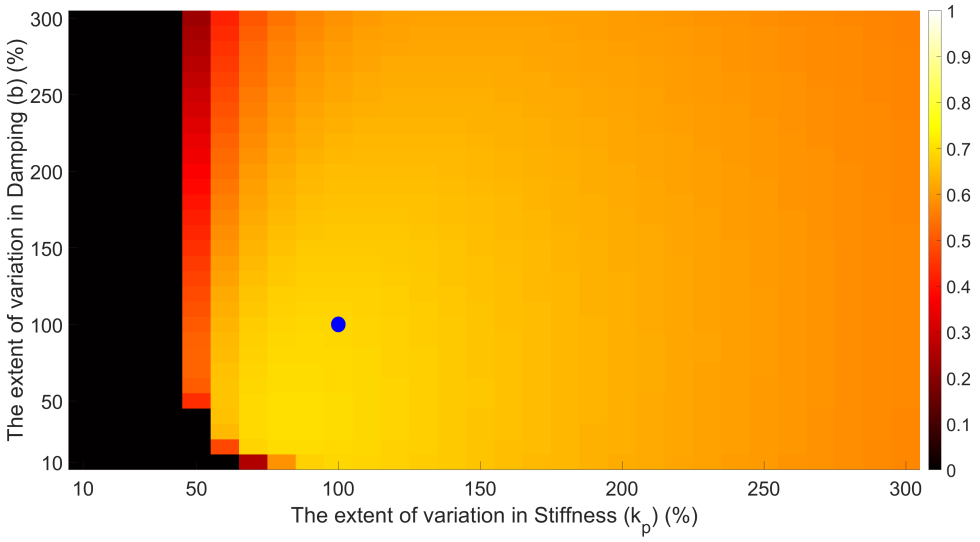

FIGURE 3.24: Performance index of gradient RC with different b, k_p.

Using (3.17) and (3.8), $b_{P,C} = 0.0074$, Figure 3.25 shows the stability condition and gap metric for each plant with different b_o and k_{po} values. It again demonstrates that the robust stability margin is conservative.

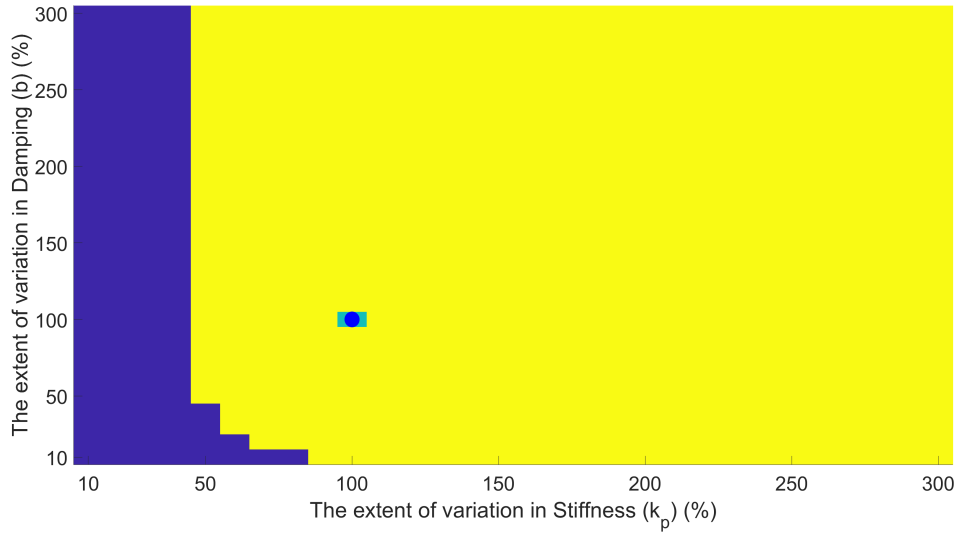

FIGURE 3.25: Stability condition and gap metric of gradient RC with different b, k_p.

The designed repetitive controller is then applied to plant with different I_p and w_n values. Figure 3.26 shows the performance index of each test. The controller can stabilize the system except when w_n is small.

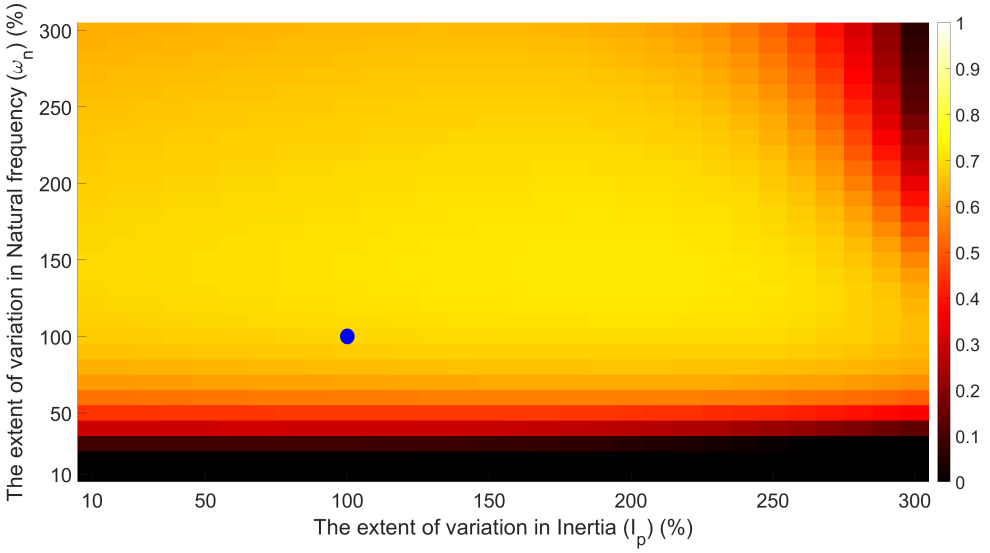

FIGURE 3.26: Performance index of gradient RC with different I_p, w_n.

Figure 3.27 shows the stability condition and gap metric for each plant with different I_p and w_n. It demonstrates that the stability condition and robust stability margin are conservative.

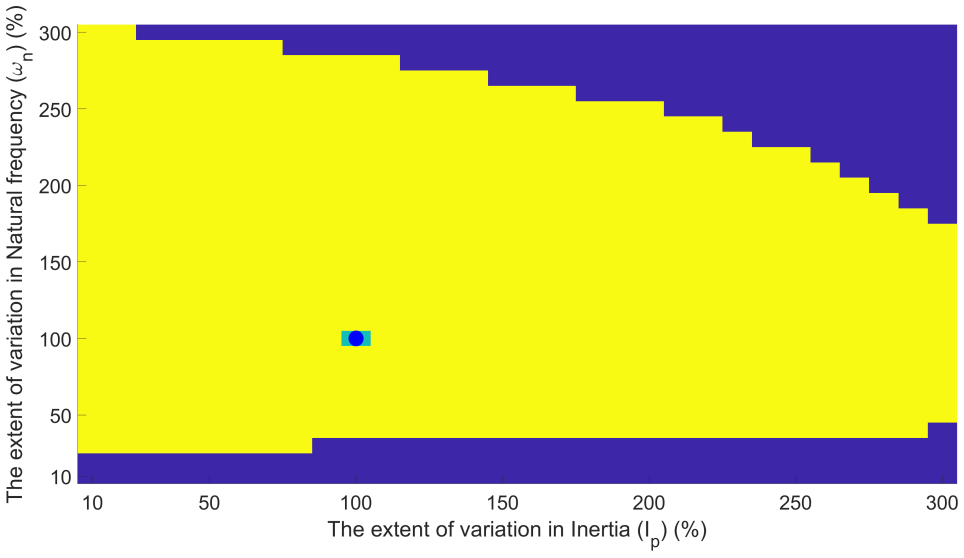

FIGURE 3.27: Stability condition and gap metric of gradient RC with different I_p, w_n.

Changing c and applying the designed controller, yields Figure 3.28. The gap metric curve shows that only if the plant does not change, the system is stable. The stability condition curve and performance index curve show that the stability conditions are

satisfied in the range of $c = 10\%c_o$ to $c = 250\%c_o$, and the system is stable when the stability condition is satisfied. However, in the stable range, the performance index is very low, indicating the controller does not achieve good tremor suppression.

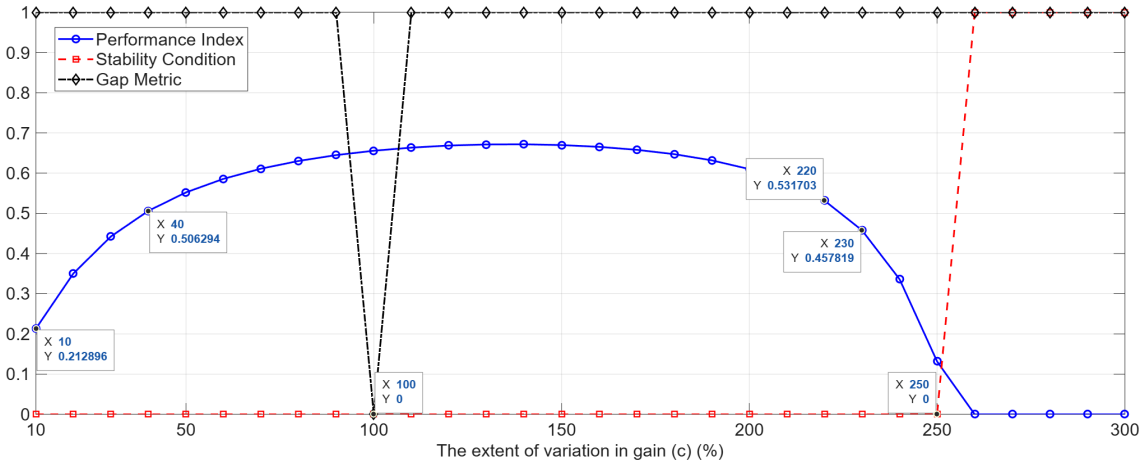

FIGURE 3.28: Performance index, stability condition and gap metric of gradient RC with different c.

Varying the frequency of the tremor and applying the designed controller, the calculated performance index is plotted in Figure 3.29. When the frequency of the tremor varies, the controller can only suppress the tremor in a small range around 1.25 Hz. Only a small range of tremors around the second harmonic of 2.5 Hz can be weakly suppressed. This demonstrates that the designed controller with only a single internal model has poor robustness to changing frequencies.

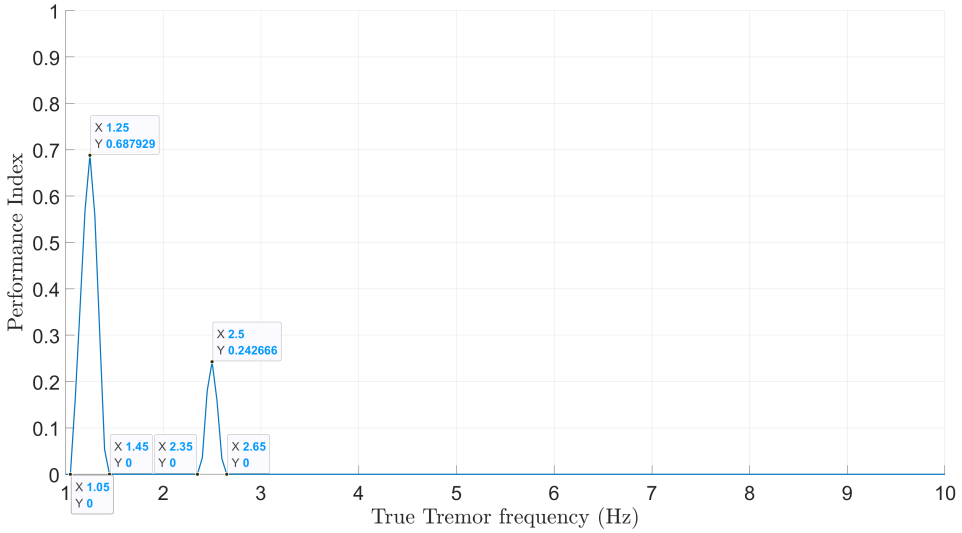

FIGURE 3.29: Performance index of gradient RC with different f.

3.7 Conclusion of Simulation Tests and Summary

The chapter first introduced robust stability margin. Then a design procedure for standard RC structure shown in Figure 2.1 was developed. This procedure is constrained by the plant impulse response length, and so the idea of introducing an additional feedback controller is proposed. The new structure is fitted into the standard framework used to analyse robust performance, and new stability conditions are derived. These are used to expand the design procedure to enable the feedback controller to be designed in a manner that transparently trades convergence and robustness. The inclusion of the robust stability margin $b_{P,C}$ provides a tool for designers to quantitatively assess and trade off robustness against convergence performance.

To validate the effectiveness of these theoretical developments and design procedures, they are applied to a realistic model of the tremulous wrist under simulated conditions. A realistic wrist model has been established, and a realistic range of parameter variation is determined. Using the design procedures, two kinds of repetitive controllers are designed, and their robustness is evaluated. The simulation results confirm the feasibility of the proposed design procedures. The stability condition and robust stability margin theorems were also validated, but the latter was found to be conservative. However, they also reveal that conventional RC lacks robustness to parametric uncertainty and time-varying tremor frequencies. These limitations motivate the development of the MMSRC framework in the following chapter.

Chapter 4

Multiple Model Switched Repetitive Control

Chapter 3 demonstrated that RC can only stabilise a subset of the prescribed plant uncertainty space $\mathcal{U}$ because of the small robust stability margin $b_{P,C}$ and limited stability condition range. To address this lack of robustness, the MMSRC framework introduced in (Freeman, 2017) is summarised. Then a principled design procedure is proposed to enable the framework to be applied to practical problems. Following this, the architecture is applied in simulation and compared with conventional RC. The primary contributions of this chapter are as follows:

- A practical, lower computational cost design procedure for MMSRC is proposed, which replaces the complex robust stability margin calculation with a performance index-based model selection criterion.
- The proposed design procedure is computationally less demanding than the theoretical framework in (Freeman, 2017), as it avoids the need for gap metric-based coverage verification in high-dimensional uncertainty spaces.
- The feasibility of the design procedure is validated through simulation, demonstrating that MMSRC is more robust to model uncertainty than conventional RC, and that increasing the number of candidate models further enhances robustness.

4.1 Multiple Model Control

The last chapter showed that the performance of conventional RC degraded significantly in the presence of modelling uncertainty. One approach to address this is multiple model control (MMC), a well-established control method for systems with unknown and potentially varying dynamics. The basic idea is to create multiple models that

represent different possible system behaviors, and design a controller for each one. Then the controllers are combined or switched in some manner in order to achieve superior performance than using any of the original controllers on their own. Many multiple model control approaches have been proposed and are now briefly summarised.

Amongst the earliest MMC methods were multiple model adaptive estimation (Lainiotis, 1976a) and multiple model adaptive control (Lainiotis, 1976b; Saridis and Dao, 1972) which 'blend' together state control signals from various models to form a resultant control signal. A similar method is robust multiple model adaptive control (Fekri et al., 2004a,b), however this uses output feedback controllers instead of state controllers. This idea was later modified to produce multiple model switched adaptive control (Morse, 1996, 1997), an approach which switches between control signals instead of blending them. It also uses the observed error as the performance criterion to determine when the switching occurs. A similar approach is adaptive switching control (Zhou et al., 1996), which uses many pre-designed controllers and switches controllers based on whether the tracking error or system energy exceeds a threshold. However, this method requires prior knowledge of system dynamics. Then a multiple model implementation of model reference adaptive control was proposed in (Ji et al., 2005). This uses fuzzy logic to select the most suitable model, which is then used by a model reference adaptive control scheme. However, the approach lacks rigorous analysis and performance guarantees to ensure the robustness of the system.

More recently, estimation based multiple model switched adaptive control (EMMSAC) was developed in (Buchstaller and French, 2016), and uses optimal disturbance estimation to measure the performance of each model. It then switches in the controller corresponding to the model that best matches the measured data. Unlike previous approaches, EMMSAC has the advantage of robust stability bounds that do not get larger when the number of plant models in increased. Its analysis was underpinned by the gap metric, ensuring that overall stability was guaranteed for a general class of uncertainty. EMMSAC was applied to FES control in (Brend, 2014), where it was used to switch between optimal controllers. Experiments were conducted applying FES to control elbow torque under isometric conditions. These demonstrated its ability to compensate for the time-varying characteristics of human muscle.

In (Freeman, 2017), the EMMSAC framework was applied to repetitive control. The result was termed MMSRC. Like its non-RC counterpart, MMSRC delivered performance bounds that did not degrade as models were added. However, despite showing stability and robust performance, only a basic simulation using a simple dynamic system was performed, and no practical guidelines were provided to aid the designer. There remain no experimental implementations of multiple model RC schemes.

4.2 Basic Principle of MMSRC

The basic idea is to first define a set of 'candidate' plant models, $\mathcal{P} = \{P_1, \cdots, P_n\}$, that may represent the true plant. A repetitive controller is designed for each P_i, and given by $\mathcal{C} = \{C_1, \cdots, C_n\}$. This is done by defining a design procedure that maps plant models to controllers, $K : \mathcal{P} \to \mathcal{C}$. An estimator $E(P_i)$ is then applied to each plant model to quantify how well it fits the measured data (u_2, y_2). This computes a residual r_{P_i} which equals the size of the smallest disturbance signal (u_0, y_0) that needs to exist assuming that model P_i is the true plant. Minimiser W selects the index i of the plant model with the smallest residual, which is then used to switch the corresponding repetitive controller C_i into closed-loop. A time delay D is added to prevent the controllers switching too rapidly. The overall MMSRC framework is illustrated by Figure 4.1, where P^* is the unknown true plant.

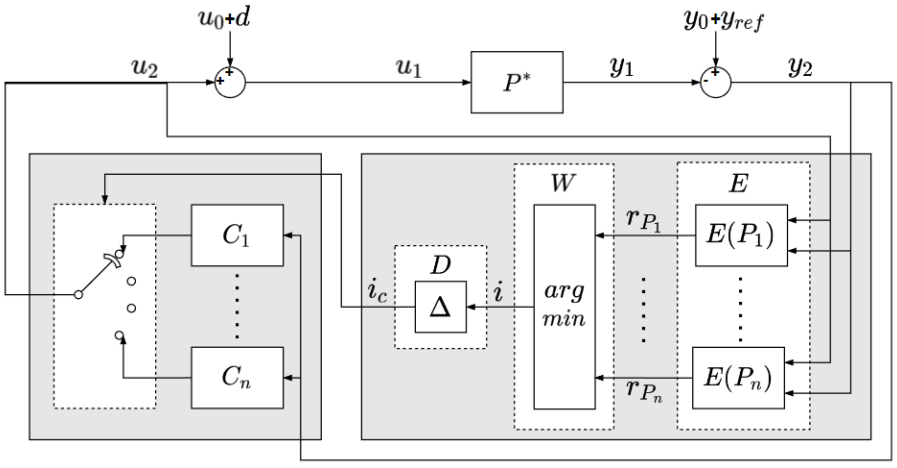

FIGURE 4.1: MMSRC structure showing uncertain plant, estimator bank, and switched controller.

4.2.1 MMSRC Robust Performance Conditions

The next theory defines conditions for the stability of MMSRC, based on the results of Freeman (2017).

Theorem 4.1. *Let the true plant $P^* \in \mathcal{U}$. Let $\mathcal{P}$ be a candidate model set and $C_i = K(P_i)$, $P_i \in \mathcal{P}$ be a control design procedure defined by (2.5). Then the MMSRC implementation stabilises the true plant provided the following two conditions are met:*

1. **Candidate plant condition:**

$$\exists P_i \in \mathcal{P},\ s.t.\ \delta_{\bar{w}_1,\tilde{w}_1}(P_i, P^*) < \rho(\mathcal{P}, \mathcal{C}, \mathcal{U}, \Delta) \tag{4.1}$$

where ρ is a positive scalar function dependent on the sets $\mathcal{C}$, $\mathcal{P}$, $\mathcal{U}$ and delay Δ.

2. **Candidate controller condition:**

$$\exists C_i \in \mathcal{C},\ s.t.\ \left\|\Pi_{P_i//C_i}\right\|_\infty < \infty,\ \forall P_i \in \mathcal{U} \tag{4.2}$$

Criterion 1 is illustrated in Figure 4.2. For an unknown true plant, there must be a candidate model that is a distance of less than $\rho(\mathcal{P},\mathcal{C},\mathcal{U},\Delta)$ away, as measured by gap metric. Criterion 1 therefore specifies a minimum radius of gap balls covering the uncertainty space, and hence dictates the number of plant models required.

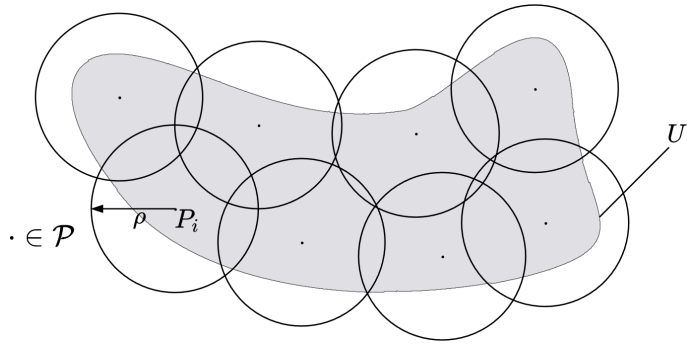

FIGURE 4.2: Criterion (4.1): Uncertainty space $\mathcal{U}$ is covered by gap metric balls of radius ρ and centre $P_i \in \mathcal{P}$.

Criterion 2 is illustrated in Figure 4.3. For each plant P_i in the uncertainty space, a controller must exist that stabilises it.

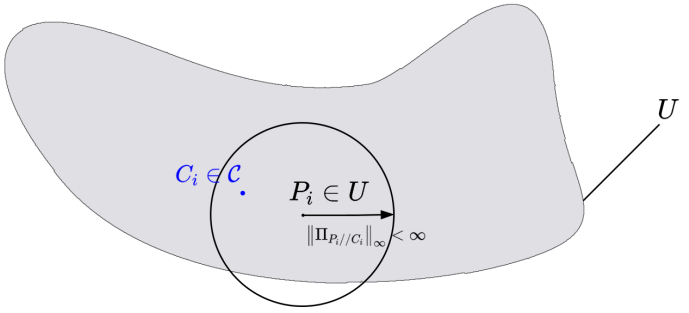

FIGURE 4.3: Criterion (4.2): $\forall P \in \mathcal{U}$, there exists $C_i \in \mathcal{C}$ that stabilises it.

Unfortunately, $\rho(\mathcal{P},\mathcal{C},\mathcal{U},\Delta)$ is very difficult to compute, and the results are also conservative (i.e. more candidate plants are specified than required). To address this, (Freeman, 2017) proposes using as many plant models as hardware allows, but does not give practical guidelines for design.

4.3 General MMSRC Design Procedure

This section formulates a new design procedure that satisfies the above criteria while limiting the number of models and controllers.

4.3.1 Design of Candidate Model Set and Controller set

Criterion 2 requires that all plants in the uncertainty set $\mathcal{U}$ are stabilised by at least one of the controllers in set $\mathcal{C}$. In principle, this can be addressed by using Theorem 3.3. It states that for a stable plant P, one can design an RC satisfying (2.16) or (2.17), which stabilizes a ball of plants with a radius of $\left|\Pi_{P_i//C_i}\right|_\infty^{-1}$ centered at P_i. Therefore, a sufficient condition to satisfy Criterion 2 is to ensure that the candidate model set $\mathcal{P}$ and controller set $\mathcal{C}$ are chosen such that the union of these balls covers $\mathcal{U}$. However, the problem is that Criterion 1 may not be satisfied, since the plants may be too spread out. This can be addressed simply by applying a gain $0 < \alpha \leq 1$ to the radius of this ball, such that reducing the weight ensures that the models move closer together. The designer can treat this gain as a tunable weight that they reduce to trade computational load for performance.

This gives rise to the practical algorithm shown in Design Procedure 3.

Design Procedure 3 Building a candidate model set

Require: Control design procedure K, uncertainty space $\mathcal{U}$, gain α, tremor period length N.

1: Compute a set of candidate models $\mathcal{P} = \{P_1, \ldots, P_n\}$ covering $\mathcal{U}$ with fine resolution.

2: For each P_i, apply design K to generate an RC update C_i that satisfies the stability condition (2.16) or (2.17).

3: For each P_i, C_i, compute robust stability margin $\alpha b_{P_i,C_i}$ using (3.8).

4: Check whether the uncertainty space $\mathcal{U}$ is covered by the union of gap balls, each with centre P_i and radius $\alpha b_{P_i,C_i}$. This step is implemented by discretizing the uncertainty space $\mathcal{U}$ into a grid of test points. For each test point $P^* \in \mathcal{U}$, compute the gap metric $\delta(P^*, P_i)$ to every candidate model $P_i \in \mathcal{P}$. If there exists at least one P_i such that $\delta(P^*, P_i) < \alpha b_{P_i,C_i}$, then P^* is considered to be covered. If all test points in $\mathcal{U}$ are covered, then $\mathcal{U}$ is covered. If the coverage is incomplete, the designer may:

- Return to Step 2 to redesign C_i to increase b_{P_i,C_i},
- Or return to Step 1 to increase the resolution of $\mathcal{P}$ by adding more candidate models in the uncovered regions.

5: Implement MMSRC. If the performance is poor, return to step 3 to reduce the gain α.

4.3.2 Estimator Design

As described, each plant model, $P_i \in \mathcal{P}$, requires an estimator $E(P_i)$ to compute a residual r_{P_i} which equals the size of the smallest disturbance signal (u_0, y_0) that needs to exist given that that model P_i is the true plant. The smaller the residual, the closer the candidate model is to the real plant. This can be achieved using a Kalman Filter, as described next.

Let P_i be implemented by the state-space triplet $(A_{P_i}, B_{P_i}, C_{P_i})$,

$$\begin{aligned} x_{P_i}(k+1) =& A_{P_i} x_{P_i}(k) + B_{P_i} u_1(k) \\ y_1(k) =& C_{P_i} x_{P_i}(k) \end{aligned} \tag{4.3}$$

where x_{P_i} is the state of the plant P_i. Then, from (Freeman, 2017), the residual can be computed recursively at each time step k using

$$r_{P_i}(k) = \left[\sum_{\tau=0}^{k} \lambda^{k-\tau} \left\| y_2(\tau) - y_{ref}(\tau) + \tilde{y}_{P_i}(\tau) \right\|^2_{\left[C_{P_i} \Sigma_{P_i}(\tau) C_{P_i}^\top + I\right]^{-1}} \right]^{\frac{1}{2}} \tag{4.4}$$

where $0 < \lambda \leq 1$ is a tunable weight used to place less emphasis on residuals which occurred further back in time. Here $\tilde{y}_{P_i}$ is the estimated output of P_i which is generated by the Kalman Filter update equations

$$\begin{aligned} \hat{x}_{P_i}(\tau + \frac{1}{2}) =& \hat{x}_{P_i}(\tau) + \Sigma_{P_i}(k) C_{P_i}^\top \left[C_{P_i} \Sigma_{P_i}(\tau) C_{P_i}^\top + I \right]^{-1} \\ & \left[y_{ref}(\tau) - y_2(\tau) - C_{P_i} \hat{x}_{P_i}(\tau) \right] \\ \Sigma_{P_i}(\tau + \frac{1}{2}) =& \Sigma_{P_i}(\tau) - \Sigma_{P_i}(k) C_{P_i}^\top \left[C_{P_i} \Sigma_{P_i}(\tau) C_{P_i}^\top + I \right]^{-1} \\ & C_{P_i} \Sigma_{P_i}(\tau) \\ \hat{x}_{P_i}(\tau + 1) =& A_{P_i} \hat{x}_{P_i}(\tau + \frac{1}{2}) + B_{P_i}(u_2(\tau) + d(\tau)) \\ \Sigma_{P_i}(\tau + 1) =& A_{P_i} \Sigma_{P_i}(\tau + \frac{1}{2}) \hat{A}_{P_i}^\top + B_{P_i} B_{P_i}^\top \\ \tilde{y}_{P_i}(\tau) =& C_{P_i} \hat{x}_{P_i}(\tau) \end{aligned} \tag{4.5}$$

where $\hat{x}_{P_i}$ is the estimated state of the plant P_i, Σ_{P_i} is the covariance of $\hat{x}_{P_i}$. Their initial conditions are $\Sigma_{P_i}(0) = 0$, $\tilde{x}_{P_i}(0) = 0$ and sample $\tau \in [0, k-1]$. This process requires knowing the tremor signal d. If d is unknown, an augmented estimator structure is required and will be developed in Section 6.2.

4.3.3 Switching Algorithm and Delay

The residuals $\{r_{P_1}, r_{P_2}, \ldots, r_{P_n}\}$ are fed back to the switching operator W, which computes the switching signal as the minimiser

$$i(k) = \underset{1 \leq i \leq n}{\operatorname{argmin}}\, r_{P_i}(jN), \quad jN \leq k < (j+1)N, \quad j \in \mathbb{N}. \tag{4.6}$$

The switching signal is then passed to operator D, which applies a delay Δ that must elapse before a switch is allowed. This delay is computed in (Freeman, 2017), but can be treated as a tunable gain. Together these elements ensure switching only occurs at the start of each period and is sufficiently delayed to prevent instability. The introduction of a switching delay Δ is essential to prevent overly frequent controller switching, which could otherwise lead to instability due to transient mismatches between the plant and controller dynamics. A small delay may cause the system to switch prematurely before the current controller has stabilized, while an excessively large delay could hinder the system's ability to adapt to rapid changes in plant dynamics. Therefore, the choice of Δ involves a trade-off between responsiveness and stability. In practice, Δ can be initially selected as several sample points to allow the current controller to converge and allow the estimator to reliably identify the optimal model. Then, this value can be adjusted experimentally based on the observed switching behavior and system performance. If the system exhibits jitter or instability, then Δ should be increased; if the system cannot adapt to dynamic changes, then Δ can be cautiously decreased.

When the new RC controller C_{i_c} is switched into closed-loop at the start of a new period by MMSRC, it computes the new control output using the stored error and the previous sequence of controller states. The latter are transferred between the old and new RC updates (rather than being reset to zero), therefore maintaining continuity. This prevents abrupt jumps which may cause discomfort to participants.

4.4 Application of MMSRC Design Procedure

Design Procedure 3 will now be applied to the application considered in the previous chapter. The first step is to specify the uncertainty set containing the true plant. From the form of (5.2) and the parameters in Table 5.1, this is given by

$$\mathcal{U} := \left\{ P(s) \text{ given by (5.1)} \;\middle|\; \begin{array}{l} c \in [10\%c_o, 300\%c_o],\ \omega_n \in [10\%\omega_{no}, 300\%\omega_{no}], \\ I_p \in [10\%I_{po}, 300\%I_{po}]\ b \in [10\%b_o, 300\%b_o], \\ k_p \in [10\%k_{po}, 300\%k_{po}] \end{array} \right\} \tag{4.7}$$

It is important to clarify the nature of this uncertainty set. As defined above, $\mathcal{U}$ is a structured (parametric) uncertainty set, since it is constructed from bounded variations in the physical parameters of the wrist model $(c, \omega_n, I_p, b, k_p)$. This approach may appear to contradict the critique in Section 2.7, where existing robust RC methods were noted for their reliance on structured uncertainty descriptions and their inability to handle general unstructured uncertainty.

The key distinction lies in the purpose and scope of the MMSRC framework. While the individual candidate models within $\mathcal{P}$ are defined using parametric uncertainty, the overall set $\mathcal{U}$ is designed to be sufficiently rich to capture the dominant effects of the real-world, unstructured uncertainty encountered in the biomedical application (e.g., effects of fatigue, spasticity, and electrodes movement). The MMSRC framework does not assume a specific structure for the uncertainty (like $P^* = (I + \Delta)P$); instead, it uses a collection of locally structured models to cover an uncertainty region that can include unstructured effects. The gap metric, which is central to the MMSRC stability theory, then provides a general measure of distance between these models and the true plant, regardless of whether the mismatch is due to parametric or unstructured dynamics.

Since this has five parameters, Design Procedure 3 still carries a high computational load since checking that the union of gap balls contains $\mathcal{U}$ must be conducted in five dimensional space within Step 4. To address this, two modifications will be made to the procedure. However, the modified procedure still possesses the required properties as it guarantees that Criterion 1 and Criterion 2 can still be satisfied.

First, Design Procedure 3 will be applied to each of the five uncertain parameters individually. For example, the uncertainty set purely associated with c is the set

$$\mathcal{U}_c := \{P(s) \text{ given by (5.1) } | c \in [10\%c_o, 300\%c_o],\ \omega_n = \omega_{no},\ I_p = I_{po},\ b = b_o,\ k_p = k_{po}\} \tag{4.8}$$

Applying Design Procedure 3 to this set then generates a set of plant models $\{P_1, \ldots, P_n\}$ that cover $\mathcal{U}_c$. The corresponding c parameters are $\{c_1, \ldots, c_n\}$. As explained previously, the designer has the choice of adding to and moving these models closer together by reducing α. This design process is then repeated for the other uncertainty sets $\mathcal{U}_{\omega_n}, \mathcal{U}_{I_p}$, $\mathcal{U}_b$ and I_{k_p} which are defined likewise. Every combination of elements in the resulting five parameter sets is then applied to produce the final model set $\mathcal{P}$. Clearly the distance between models in $\mathcal{P}$ can be made arbitrarily small via reduction of α and stability of each controller then guarantees that the entire space $\mathcal{U}$ is covered. This modified design process therefore satisfies Criterion 1 and Criterion 2 as required.

Secondly, in Step 3 of Design Procedure 3, the robust stability margin b_{P_i,C_i} is exchanged for the performance index given by (3.25) to simplify computation. The performance index provides a practical and computationally efficient alternative to the robust stability margin. In implementation, this is calculated by:

1. Simulating the closed-loop system with controller C_i applied to plant P_i to obtain the controlled output y_c.
2. Computing the 2-norm ratio $\frac{\|y_c\|}{\|y\|}$, where $\|y\|$ is the norm of the uncontrolled tremor output.
3. Applying the threshold to ensure tremor suppression performance.

This simulation-based approach directly quantifies tremor suppression effectiveness, making it more intuitive for designers while avoiding the computational complexity of gap metric calculations. This performs exactly the same role of measuring the robust stability of the system $[P_i, C_i]$, but is easier to compute. The role of α remains the same. With these refinements, Design Procedure 3 is replaced by Design Procedure 4.

Design Procedure 4 Building a candidate model set

Require: Model of plant P, uncertainty space $\mathcal{U}$, tremor period length N.

1: Choose one parameter in the model, c. Then define set $\{c_1 = 10\%c_o, c_2 = 20\%c_o, \ldots, c_{30} = 300\%c_o\}$ covering the variation range in c at a fine resolution. Keep the other parameters unchanged and construct the model set $\mathcal{P}_c = \{P_{c1}, \ldots, P_{c30}\}$.
2: For each P_{ci}, design an RC update C_{ci} that satisfies the stability condition (2.16) or (2.17).
3: Then apply C_{ci} to every $P_{ci} \in \mathcal{P}_c$, and compute the performance index. Plot the performance index against c for the full range of uncertainty, $c_1 \leq c \leq c_{30}$.
4: Check the variation range of c that each C_{ci} can stabilize. Choose a minimum set of model parameters (e.g. $c_3 = 30\%c_o, c_{25} = 250\%c_o$) whose controllers collectively cover the entire variation range of c and have a high performance index as the individual parameter set. The controllers must ensure performance index $> 1 - \alpha$. If not, return to Step 2 to tune the RC update to increase the performance index or to Step 1 to increase the parameter resolution.
5: For other parameters ω_n, I_p, b, k_p, repeat Step 1 to 4.
6: Combine all the combinations of individual parameter sets to form the final candidate model set $\mathcal{P}$. Design a RC update for each one.
7: Implement MMSRC. If the performance is poor, return to Step 4 to increase the number of parameters in individual parameter set or reduce α.

The theoretical design procedure in (Freeman, 2017) requires checking whether the uncertainty space $\mathcal{U}$ is covered by the union of gap metric balls, which involves high-dimensional optimization and gap metric computations for each candidate model. This is computationally expensive, especially when the uncertainty space has multiple parameters. In contrast, the proposed practical Design Procedure 4 replaces the gap metric with a performance index, which is easier to compute and does not require iterative

gap metric evaluations. This significantly reduces the computational load, making the design process more feasible for practical applications.

Figure 4.4 and Figure 4.5 illustrates Step 3 and Step 4 of Design Procedure 4. If α is preset to 0.1, the controller must ensure that the performance index is greater than 0.9. A FMI-RC designed for P_{c3} with $c = 30\%c_o$ is applied to $\mathcal{P}_c$. It can be seen from Figure 4.4 that this controller is sufficient to cover the variation range of c from $c = 10\%c_o - 40\%c_o$. In Figure 4.5, the FMI-RC designed for P_{c25} with $c = 250\%c_o$ stabilizes the model with c varying from $c = 30\%c_o - 300\%c_o$. Since the combination of two controllers designed for these two parameters is sufficient to stabilize the entire range of c, $\{c_3 = 30\%c_o, c_{25} = 250\%c_o\}$ is chosen as an individual parameter set.

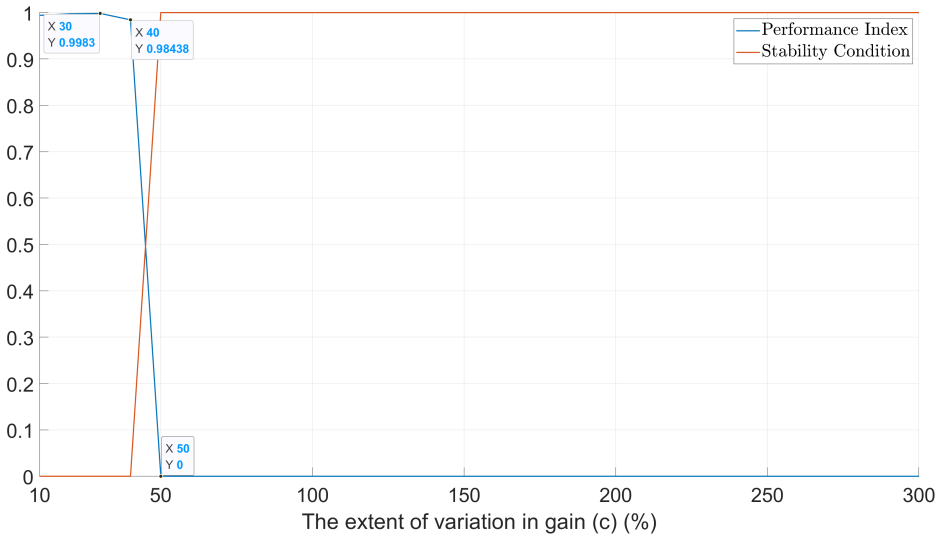

FIGURE 4.4: Performance index and stability condition with different c (FMI-RC is designed for the plant with $c = 30\%c_o$).

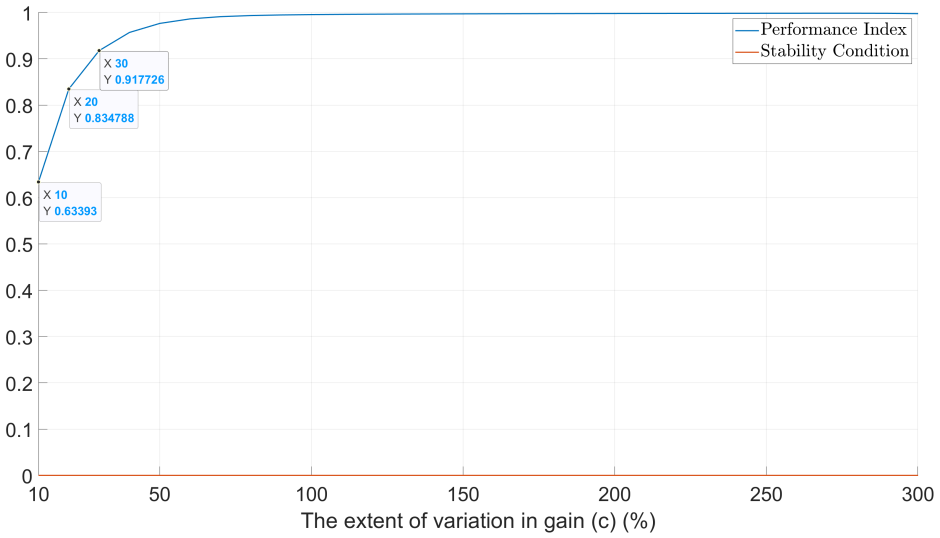

FIGURE 4.5: Performance index and stability condition with different c (FMI-RC is designed for the plant with $c = 250\%c_o$).

The parameter sets shown in Table 4.1 result from applying Steps 4 and 5 of Design Procedure 4 to the uncertainty set (4.7). Designing controllers with performance index greater than $1 - \alpha$ for each individual parameter set in Table 4.1 is sufficient to cover the variation range of this parameter.

Parameter	Individual parameter set	Unit
c	$30\%c_o, 250\%c_o$	$-$
ω_n	$10\%\omega_{no}, 30\%\omega_{no}, 60\%\omega_{no}, 220\%\omega_{no}$	rad/s
I_p	$280\%I_{po}$	$kg \cdot m^2$
b	$10\%b_o, 120\%b_o$	$Nm \cdot s/rad$
k_p	$10\%k_{po}, 150\%k_{po}$	Nm/rad

TABLE 4.1: Parameter sets (33 models case).

Thirty-two models are built using all combinations of the parameter sets. After adding the original nominal model, a candidate model set with 33 models $\mathcal{P} = \{P_1, \ldots, P_{33}\}$ is obtained. Then in Step 6 the controller set $\mathcal{C}$ is obtained by designing the FMI-RC update with the highest performance index and satisfying the stability condition (2.17) for each P_i. For each mode $P_i \in \mathcal{P}$, equations (5.27) and (4.5) are used to implement the corresponding estimator $E(P_i)$.

4.5 Robustness of MMSRC to Parametric Uncertainty

The same experimental framework as in Chapter 3 is now used to verify the effect of MMSRC, and compare it with the results of FMI-RC in Section 3.5.5. The model of the wrist and its parameter range are the same as those in Section 3.4.1. The tremor frequency is set to 2 Hz. The parameter value of the true plant P^* will be changed to observe the performance of MMSRC for different levels of model uncertainty.

4.5.1 Robustness of MMSRC (33 models) to Parametric Uncertainty

MMSRC is now applied to a true plant P^*, in which there is a large variation in b and k_p values. The variation range of b and k_p are shown in Table 3.1, and range from 10% to 300% of their original value. Figure 4.6 shows the performance index of each P^*. Each coloured square represents a whole experiment in which EMMSRC is applied to a different true plant (with parameters shown on the axes).

The blue point represents the original, nominal, plant model P. Comparing Figure 4.6 and Figure 3.13, true plants with k_p less than 50% of the nominal value are also stabilised under the control of MMSRC (33 models). Most of the performance indices are higher than those of single model FMI-RC, demonstrating that MMSRC improves the suppression performance on plants with uncertainty. However, since a relatively course initial plant set in Step 1 and high value of α have been selected in some cases, Design Procedure 4 cannot guarantee complete coverage of the uncertainty space. Hence there are still some models in Figure 4.6 that have not been stabilized.

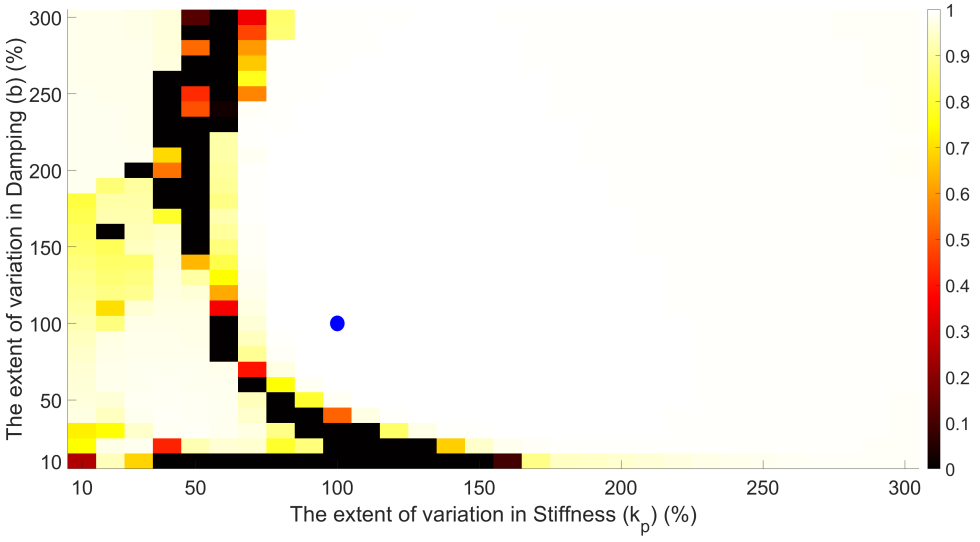

FIGURE 4.6: Performance index of MMSRC (33 models) with different b, k_p.

MMSRCs is next designed for a true plant P^* in which there is a large variation in I_p and w_n values. The variation range of I_p and w_n are shown in Table 3.1, and range from 10% to 300% of their original, nominal, value. Compared with Figure 4.6 and Figure 3.15, MMSRC (33 models) stabilized more plants when I_p is greater than $150\%I_{po}$ and w_n is greater than $150\%\omega_{no}$. However, due to the lack of candidate models, MMSRC still has not stabilized most of the models with I_p less than $150\%I_{po}$ and w_n greater than $150\%\omega_{no}$ and a small number of models with very small w_n.

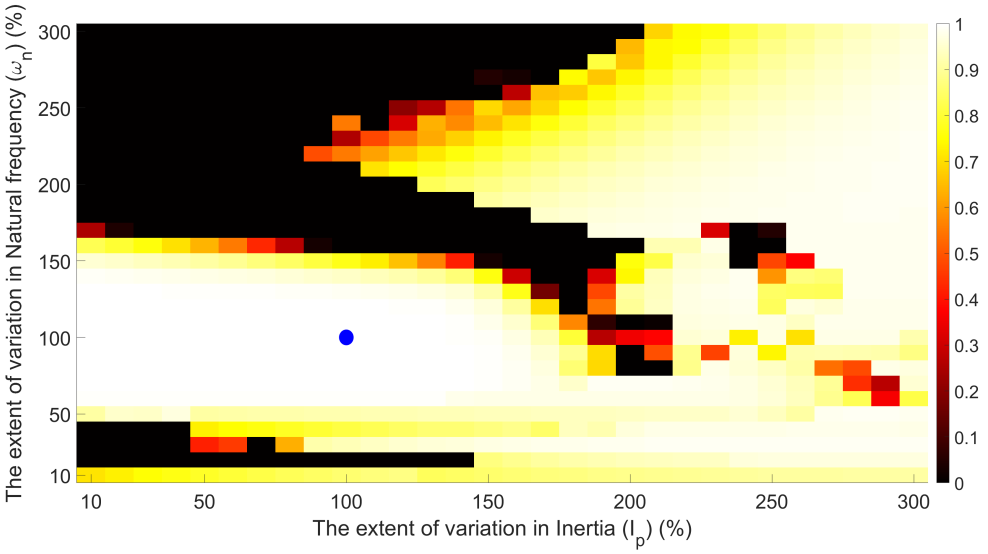

FIGURE 4.7: Performance index of MMSRC (33 models) with different I_p, w_n.

Next MMSRC is applied to true plant P^* in which there is a large variation in c values. Compared with Figure 3.17, although MMSRC (33 models) failed to stabilize the plants with $c = 10\%c_o$ and $c = 160\%c_o$, MMSRC (33 models) suppresses tremors in plants with c greater than $200\%c_o$. Furthermore, MMSRC achieves a higher performance index when plants are stabilized.

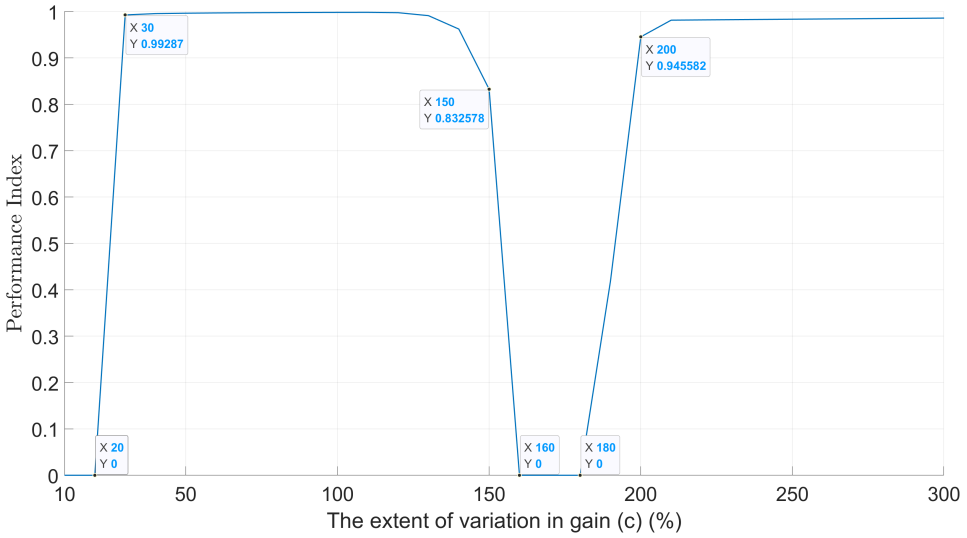

FIGURE 4.8: Performance index of MMSRC (33 models) with different c.

4.5.2 Effect of Adding Candidate Models

In order to verify the effect of increasing the number of candidate models, the size of the parameter sets computed in Step 4 are increased as shown in Table 4.2. The number of candidate models is increased to 145. Based on the new candidate model set, controllers and estimators are then designed.

Parameter	Representative value	Unit
c	$30\%c_o, 250\%c_o$	–
ω_n	$10\%\omega_{no}, 30\%\omega_{no}, 60\%\omega_{no}, 220\%\omega_{no}$	rad/s
I_p	$100\%I_{po}, 280\%I_{po}$	$kg \cdot m^2$
b	$10\%b_o, 120\%b_o, 220\%b_o$	$Nm \cdot s/rad$
k_p	$10\%k_{po}, 150\%k_{po}, 260\%k_{po}$	Nm/rad

TABLE 4.2: Parameter sets (145 models case).

Having increasing the number of candidate models to 145, MMSRC is again applied to true plant P^* in which there is a large variation in b and k_p values. Comparing Figure 4.6 and Figure 4.9, it can be seen that adding candidate models allows more plants to be stabilized, and the overall performance indices are still higher than that of single model FMI-RC.

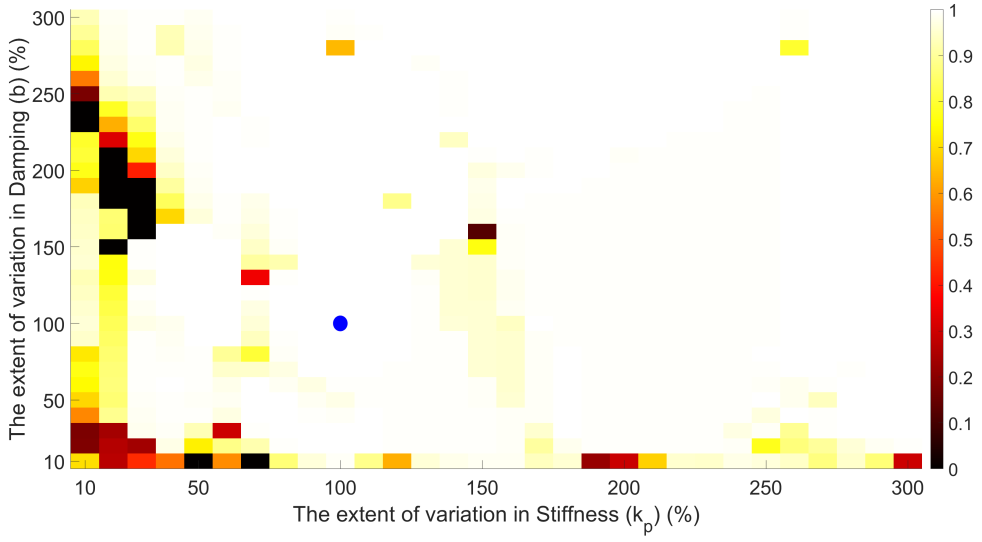

FIGURE 4.9: Performance index of MMSRC (145 models) with different b, k_p.

Increasing the number of candidate models to 145, MMSRC is again applied to true plant P^* in which there is a large variation in I_p and w_n values. Figure 4.10 shows that most true plants can now be stabilized after adding more models.

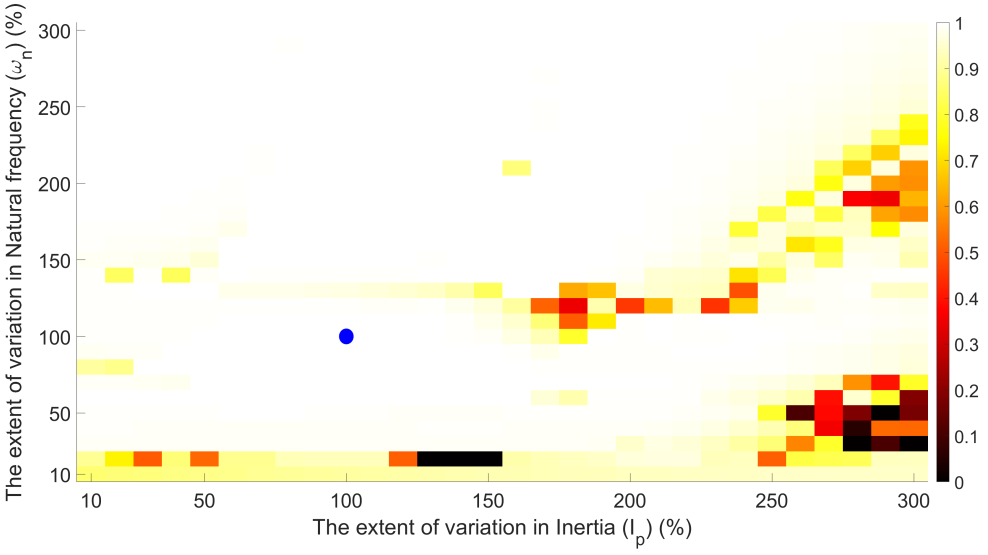

FIGURE 4.10: Performance index of MMSRC (145 models) with different I_p, w_n.

By increasing the number of models to 145, all models with c uncertainty are stabilized.

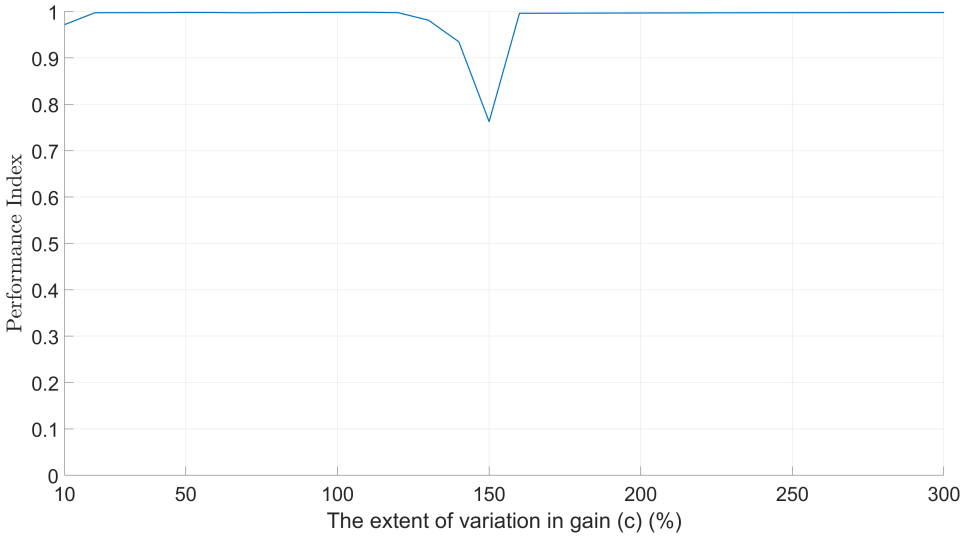

FIGURE 4.11: Performance index of MMSRC (145 models) with different c.

4.6 Conclusion of Simulation Tests

The simulation results presented in this chapter clearly demonstrated the superior robustness of the MMSRC framework compared to conventional RC. Across a wide range of parametric uncertainties, MMSRC maintained effective tremor suppression where conventional RC failed or exhibited significantly degraded performance.

A key finding is the relationship between robustness and the size of the candidate model set. The results substantiate that increasing the number of candidate models within the MMSRC framework further enhances its robustness to model uncertainty. This is evidenced by the performance improvement observed when expanding the candidate set from 33 models to 145 models, which allowed a larger portion of the uncertainty space $\mathcal{U}$ to be stabilized with high performance indices.

The simulation results confirmed that the performance index-based design procedure was not only effective in enhancing robustness but also computationally efficient. For example, using Design Procedure 4 in MATLAB to design and establish an MMSRC (containing 145 candidate models) sufficient to cover most of the uncertainty space took approximately 60 minutes, whereas the theoretical gap metric approach, due to its conservative value and high computational load, still failed to yield suitable results even after running for 7 hours. This demonstrated the practical viability of the proposed method.

However, the Design Procedure 4 employed to manage computational load does not provide a formal guarantee of complete uncertainty space coverage unless the tuning parameter α is driven to a very small value, necessitating a large number of models.

This highlights an inherent trade-off: while increasing the number of candidate models enhances robustness, it also increases computational complexity. Consequently, the designer must strike a balance between the desired level of robust performance and the acceptable computational load when implementing MMSRC in practice.

4.7 Summary

This chapter introduced the MMSRC framework and its theoretical foundations. A key contribution was the development of a practical design procedure that significantly reduced computational cost by replacing the gap metric with a performance index for model selection. Simulation results validated that MMSRC was more robust to model uncertainty than conventional RC, and that increasing the number of candidate models further enhanced robustness. The proposed design procedure provided a feasible and efficient approach for real-world implementations where computational resources were limited.

Chapter 5

MMSRC for Hammerstein Systems

Chapter 4 demonstrated the feasibility of the MMSRC for tremor suppression and showed its robustness in the face of model uncertainty. The controller formulation and robustness results used were for linear systems. However, in practical applications the controlled plant may possess nonlinear components. Therefore, it is necessary to extend both the developed wrist model and the linear MMSRC components so that they support Hammerstein systems. This chapter will first establish why a Hammerstein system structure is appropriate for tremor suppression, and then go on to derive the relevant robustness theory, laying the foundation for subsequent applications. The primary contributions of this chapter are as follows:

- Robust stability theory for nonlinear RC: The robust stability analysis tool introduced in Chapter 3 for linear systems is formally extended to handle the Hammerstein system structure. This provides theoretical guarantees for a broader class of systems.
- Generalization of the MMSRC framework: The entire MMSRC framework, including its stability conditions and design procedures, is expanded from linear systems to Hammerstein systems. This significant extension greatly enhances the practical applicability of the proposed control strategy.

These developments collectively form a comprehensive theoretical foundation that enables the application of MMSRC to nonlinear systems, as will be validated experimentally in the following chapter.

5.1 Modeling of Wrist Dynamics

Section 3.4.1 assumed that, under ideal conditions with appropriate co-activation levels, the IRC can be considered approximately linear within the intended FES range. Recall the general model structure introduced in Section 3.4.1, which is duplicated in Figure 5.1.

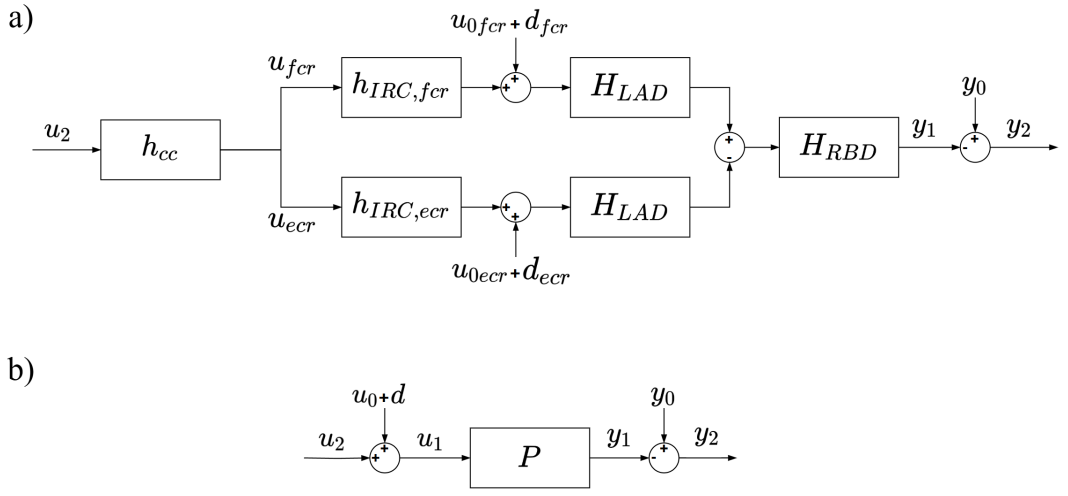

FIGURE 5.1: a) Biomechanical wrist model with coactivation function h_{cc}, b) simplified wrist model P.

However, in practice, due to potentially inappropriate coactivation levels setting and variations in participants' wrist parameters, the assumption that the h_{cc} block and IRC blocks form a static gain may not be valid. Therefore, this assumption will now be removed. Instead, the combination of the two IRC functions and the coactivation function (3.22) produce the form

$$f(u_2) = \begin{cases} h_{IRC,fcr}(u_2 + \bar{u}_{fcr}) - h_{IRC,ecr}(\bar{u}_{ecr}), & u_2 \in [0, u_{max} - \bar{u}_{fcr}] \\ h_{IRC,fcr}(\bar{u}_{fcr}) - h_{IRC,ecr}(-u_2 + \bar{u}_{ecr}), & u_2 \in [\bar{u}_{ecr} - u_{max}, 0) \end{cases} \tag{5.1}$$

It is shown in Figure 3.6b). Combined with the other components defined previously in Section 3.4.1, the overall system can be represented in a single Hammerstein form, $P = (f, G)$, as illustrated in Figure 5.2, where

$$G = H_{LAD} \cdot H_{RBD} \tag{5.2}$$

As in Section 3.4.1, periodic signals d_{fcr} and d_{ecr} represent tremor effects on the FCR and ECR muscles respectively. Their period equals the inverse of the tremor frequency. The combined periodic disturbance $d = d_{fcr} + d_{ecr}$ represents the overall tremor. Similarly, u_{0fcr} and u_{0ecr} denote the unknown process noise with $u_0 = u_{0fcr} + u_{0ecr}$. Additionally, unknown measurement noise y_0 affects the wrist angle y_1.

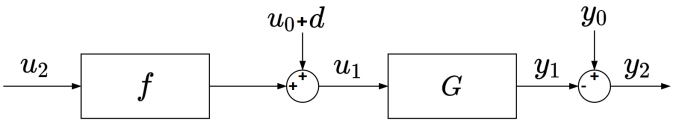

FIGURE 5.2: Equivalent Hammerstein wrist model $P = (f, G)$.

5.2 Extended Hammerstein RC Control System

As introduced in Section 2.5, since RC is designed to control linear plants, it is necessary to introduce the inverse function ϕ of f to counteract the nonlinear portion of the wrist. Figure 5.3 illustrates the closed loop system with system $P = (f, G)$ and repetitive control components $C = (\phi, R)$. When $f = I$ and $\phi = I$, this simplifies to the linear structure of Figure 3.7. The distinction lies in the composition of G: in Figure 5.3, G denotes the cascade of LAD and RBD systems, expressed as $G = H_{LAD} \cdot H_{RBD}$; whereas in Figure 3.7, G incorporates the ideal linearized IRC gain c, yielding $G = c \cdot H_{LAD} \cdot H_{RBD}$.

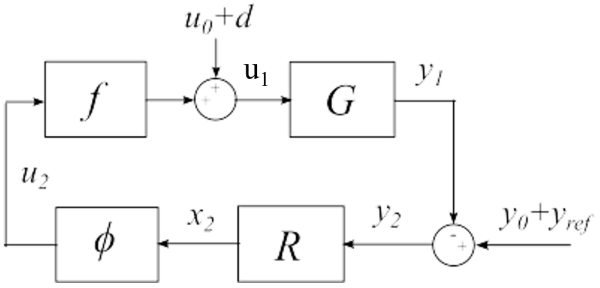

FIGURE 5.3: Closed-loop nominal RC system.

If full model information is available, $\phi(x_2)$ can be chosen as a linearising function such that

$$f(\phi(x_2)) = x_2, \quad x_{min} \leq x_2 \leq x_{max}. \tag{5.3}$$

where $x_{min} = -h_{IRC,ecr}(u_{max}) + h_{IRC,fcr}(\bar{u}_{fcr})$ and $x_{max} = h_{IRC,fcr}(u_{max}) - h_{IRC,ecr}(\bar{u}_{ecr})$. The operator R represents the RC update designed for the linear component G. Its update law and stability conditions are described in Section 2.6.

5.3 The Robust Stability of Hammerstein RC System

The robust stability theory in Section 3.1 needs to be extended to address the nonlinearities and uncertainties introduced by the Hammerstein system.

The standard gap analysis framework expresses system performance with respect to its ideal, disturbance-free operating points (termed 'biases') (Georgiou and Smith, 1997). Thus, Figure 5.3 is equivalently depicted as Figure 5.4a) by introducing biases on the internal signals. Similar to the definition of the basis in Section 3.1.1, the signal $\bar{w}_0 = (d, y_{ref})^\top$ denotes the external bias, $w_0 = (u_0, y_0)^\top$ denotes the external disturbance, and $\bar{w}_i = (\bar{u}_i, \bar{y}_i)^\top$ denotes the internal bias for the plant ($i = 1$) and controller ($i = 2$). Similarly, $w_i = (u_i, y_i)^\top$ are the internal disturbances with respect to the biases.

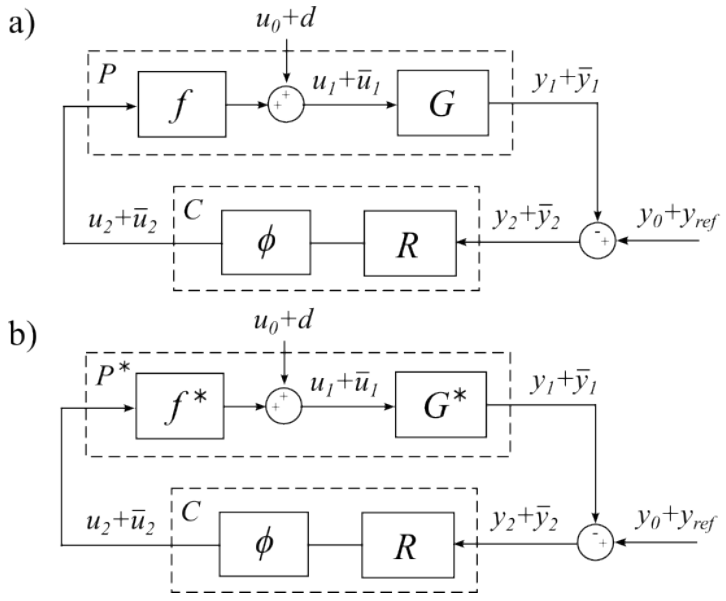

FIGURE 5.4: a) Closed-loop nominal RC system $[P, C]$, b) True RC closed loop system $[P^*, C]$.

Using these definitions, the parallel projection operator maps external signals to internal signals and is defined as

$$\Pi_{P//C} : (w_0 + \bar{w}_0) \mapsto (w_1 + \bar{w}_1) \tag{5.4}$$

with internal plant bias $\bar{w}_1 = \Pi_{P//C}\bar{w}_0$.

Based on the above definitions, the gain stability in Definition 4.1. is extended to the robust stability condition in Theorem 7.1.

Theorem 5.1. *Consider the nominal system $P = (f, G)$ with repetitive controller $C = (\phi, R)$ shown in Figure 5.3, where f is an increasing function, $\phi = f^{-1}$, and RC update*

(2.5) *satisfies* (2.16) *or* (2.17). *Then the closed-loop RC system* $[P, C]$ *is gain stable with a biased operator norm*

$$\|\Pi_{P//C}\|_{\bar{w}_0} < \infty. \tag{5.5}$$

where

$$\Pi_{P//C} = \begin{pmatrix} I \\ G \end{pmatrix} (I + RG)^{-1}(I, R). \tag{5.6}$$

In particular, an upper bound is given by

$$\|\Pi_{P//C}\|_{\bar{w}_0} \leq \|D_\Pi\| + \frac{\|(I - C_\Pi)V_\Pi\|\|V_\Pi^{-1}B_\Pi\|}{1 - \eta} \tag{5.7}$$

where $(A_\Pi, B_\Pi, C_\Pi, D_\Pi)$ *are a state-space representation of* $\Pi_{P//C}$ *and* V_Π *contains the eigenvectors of* A_Π. *Moreover the deviation of the plant signals from their ideal values is bounded as* $\|w_1\| \leq \|\Pi_{P//C}\|_{\bar{w}_0}\|w_0\|$. *Finally, closed-loop system* $[P, C]$ *has a robust stability margin.*

Proof. The standard analysis framework of (Georgiou and Smith, 1997) assumes the form of Figure 5.5b), where M and N are operators.

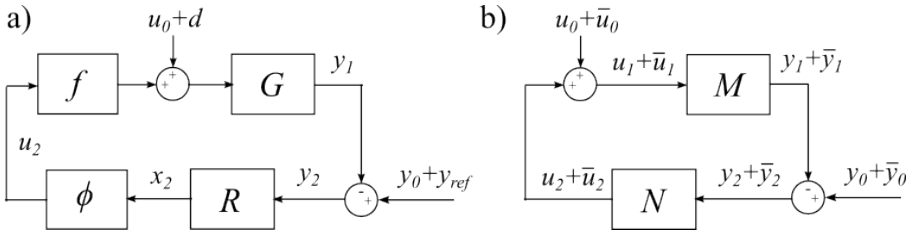

FIGURE 5.5: a) Closed-loop nominal RC system and b) standard form $[M, N]$.

The RC system of Figure 5.5a) can be placed in this form by adopting the augmented structure shown in Figure 5.6 so that $\bar{w}_0 = (d, 0, y_{ref})^\top$, $w_0 = (u_0, x_0, y_0)^\top$, $\bar{w}_1 = \Pi_{M//N}\bar{w}_0$, $w_1 = (u_1, x_1, y_1)^\top$. Both nonlinear terms are placed in M to reduce conservativeness.

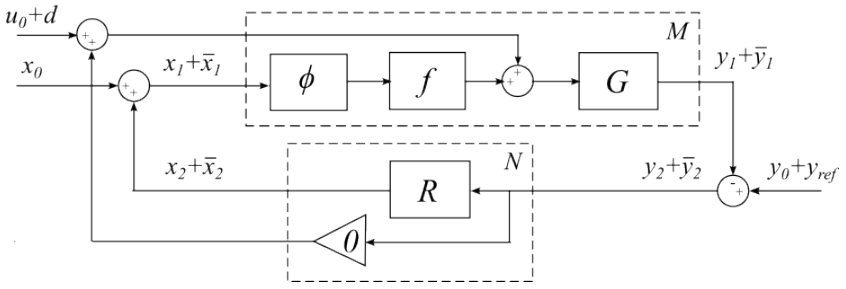

FIGURE 5.6: Nominal RC system in standard form with additional disturbance x_0.

For this system, the parallel projection operator maps external signals to internal signals and is defined as

$$\Pi_{M//N} : (w_0 + \bar{w_0}) \mapsto (w_1 + \bar{w_1}) \tag{5.8}$$

and the standard gain stability criterion (Georgiou and Smith, 1997) is $\|\Pi_{M//N}\|_{\bar{w}_0} < \infty$. Now $\|\Pi_{M//N}\|_{\bar{w}_0} =$

$$\begin{aligned} &\left\| \begin{pmatrix} I & 0 & 0 \\ (I+RG)^{-1}RG & (I+RG)^{-1} & (I+RG)^{-1}R \\ G(I+RG)^{-1} & G(I+RG)^{-1} & G(I+RG)^{-1}R \end{pmatrix} \right\|_\infty \\ =&\left\| \begin{pmatrix} (I+RG)^{-1} & (I+RG)^{-1}R \\ G(I+RG)^{-1} & G(I+RG)^{-1}R \end{pmatrix} \right\|_\infty = \left\|\Pi_{P//C}\right\|_{\bar{w}_0} \end{aligned} \tag{5.9}$$

The terms on the bottom have already been computed in (2.12). The remaining two terms have also been computed in (3.9). It can be seen that (2.12) and (3.9) share identical poles, and both are solutions to (2.15). It follows that, if stability criterion (2.16) or (2.17) holds and $P(q)$ is stable, then all four terms will be stable. The operator $\Pi_{P//C}$ is then stable and therefore $\|\Pi_{P//C}\|_\infty$ is bounded above.

The bound on $\Pi_{P//C}$ follows by expressing the signal $w_1(k)$ as a sum of $w_0(i)$ terms, $i \leq k$, using the state-space form of $\Pi_{P//C}$. This expression is then partitioned and bounded and to generate the required upper bound on the operator norm $\|\Pi_{P//C}\|$. Applying structured singular value analysis is required to yield the bound $\rho(A_\Pi) < \eta$. This leads to (5.7).

Finally note that stability of $[M, N]$ guarantees stability of $[P, C]$ since the latter is the special case $x_0 = 0$. □

The robust stability margin in Section 3.1.2 also needs to be extended to incorporate unstructured uncertainties and nonlinearities.

Suppose the true plant is denoted $P^* = (f^*, G^*)$ and differs from the model $P = (f, G)$ used for control design. In this case, the controller $C = (\phi, R)$ designed for P might not stabilise P^*. To derive robust stability margins for the resultant closed-loop system, it is first necessary to quantify the difference between the two plants. This can be achieved through the gap metric mentioned in Section 3.1.2.

In particular, the nonlinear biased gap metric is defined by the following well-known measure of distance between their graphs, $\mathcal{G}_{P,\bar{w}_1}$ and $\mathcal{G}_{P^*,\tilde{w}_1}$.

$$\vec{\delta}_{\bar{w}_1,\tilde{w}_1}(P, P^*) = \begin{cases} \inf\{\|(\Psi - I)|_{\mathcal{G}_{P,\bar{w}_1}}\|_{\bar{w}_1} |\ \Psi \text{ is a causal} \\ \text{ surjective map from } \mathcal{G}_{P,\bar{w}_1} \text{ to } \mathcal{G}_{P^*,\tilde{w}_1} \\ \text{ with } \Psi(\bar{w}_1) = \tilde{w}_1\}, \\ \infty \text{ if no such operator } \Psi \text{ exists.} \end{cases} \tag{5.10}$$

The specific meaning of each component in (5.10) is as follows:

- $\vec{\delta}_{\bar{w}_1,\bar{w}_1}(P, P^*)$ is the directed biased gap between plants P and P^*, quantifying how well P approximates P^* under operating conditions defined by the bias $\bar{w}_1$.
- $\mathcal{G}_{P,\bar{w}_1}$ and $\mathcal{G}_{P^*,\bar{w}_1}$ are the graphs of plants P and P^* respectively, representing the set of all possible input-output signal pairs (u_1, y_1) that satisfy each plant's dynamics, centered around their respective bias operating points $\bar{w}_1 = (\bar{u}_1, \bar{y}_1)^\top$.
- Ψ is a causal surjective mapping that transforms signals from the graph of P to the graph of P^*. The requirement that $\Psi(\bar{w}_1) = \bar{w}_1$ ensures that the steady-state operating points (biases) are preserved under this mapping.
- $(\Psi - I)|_{\mathcal{G}_{P,\bar{w}_1}}$ represents the deviation operator, which measures how much the mapping Ψ differs from the identity mapping I when restricted to the graph of P.
- $\|\cdot\|_{\bar{w}_1}$ denotes the biased norm, which evaluates the size of signals relative to the bias $\bar{w}_1$, providing a local measure of distance around the operating point.
- The infimum is taken over all possible causal surjective mappings Ψ that preserve the bias, thus finding the smallest possible distance between the two plants' behaviors.

In essence, this metric finds the best possible causal mapping that transforms the behavior of plant P into that of plant P^* while preserving steady-state operation, and then measures how different this mapping is from doing nothing (the identity mapping). A smaller gap value indicates that the two plants are more similar in their input-output behavior around the operating point defined by $\bar{w}_1$.

Using this measure, the sufficient conditions for stability of the closed-loop system formed by connecting P^* and C in Theorem 4.2. are extended as Theorem 7.2. and illustrated in Figure 5.4b).

Theorem 5.2. *Consider the true system $P^* = (f^*, G^*)$ with a repetitive controller $C = (\phi, R)$ designed for model $P = (f, G)$ where R satisfies* (2.16) *or* (2.17)*, and both f and f^* are increasing functions, with $\phi = f^{-1}$. Then the closed-loop system $[P^*, C]$ is gain stable if the gap between systems satisfies*

$$\vec{\delta}_{\bar{w}_1,\tilde{w}_1}(P, P^*) < \epsilon \|\Pi_{P//C}\|^{-1}_{\bar{w}_0}, \tag{5.11}$$

and f satisfies the lower sector bound

$$\epsilon|x| \leq |f(x + \bar{x}) - f(\bar{x})|, \qquad \forall x, \bar{x} \in dom(f), \quad \epsilon > 0. \tag{5.12}$$

Proof. First place the nominal system in standard $[M, N]$ form as shown in Figure 5.6. Likewise the true system is denoted M^* and is shown in Figure 5.7.

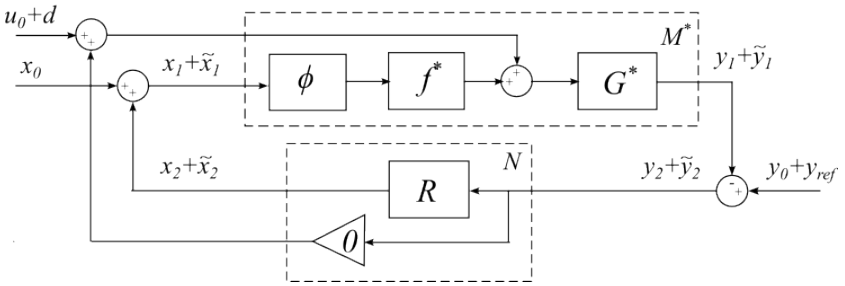

FIGURE 5.7: True RC closed loop system $[M^*, N]$ in standard form with internal biases $\tilde{w}_i = (\tilde{u}_i, \tilde{y}_i)^\top$, $i = 1, 2$.

Since these are in standard form, results from (Georgiou and Smith, 1997) state that stability holds if

$$\vec{\delta}_{\bar{w}_1,\tilde{w}_1}(M, M^*) < \|\Pi_{M//N}\|_{\tilde{w}_0}^{-1}. \tag{5.13}$$

Since G and G^* are stable, their graphs simplify to

$$\mathcal{G}_{M,\bar{w}_1} := \left\{ \begin{pmatrix} \begin{pmatrix} u_0 + \bar{u}_0 \\ x_1 + \bar{x}_1 \end{pmatrix} \\ M \begin{pmatrix} u_0 + \bar{u}_0 \\ x_1 + \bar{x}_1 \end{pmatrix} \end{pmatrix} : \left\| \begin{matrix} u_0 \\ x_1 \end{matrix} \right\| < \infty \right\},$$

$$\mathcal{G}_{M^*,\tilde{w}_1} := \left\{ \begin{pmatrix} \begin{pmatrix} u_0 + \tilde{u}_0 \\ x_1 + \tilde{x}_1 \end{pmatrix} \\ M^* \begin{pmatrix} u_0 + \tilde{u}_0 \\ x_1 + \tilde{x}_1 \end{pmatrix} \end{pmatrix} : \left\| \begin{matrix} u_0 \\ x_1 \end{matrix} \right\| < \infty \right\}.$$

Hence there exists the surjective map $\Psi : \mathcal{G}_{M,\bar{w}_1} \to \mathcal{G}_{M^*,\tilde{w}_1}$

$$\Psi \begin{pmatrix} \begin{pmatrix} u_0 + \bar{u}_0 \\ x_1 + \bar{x}_1 \end{pmatrix} \\ M \begin{pmatrix} u_0 + \bar{u}_0 \\ x_1 + \bar{x}_1 \end{pmatrix} \end{pmatrix} = \begin{pmatrix} \begin{pmatrix} u_0 + \tilde{u}_0 \\ x_1 + \tilde{x}_1 \end{pmatrix} \\ M^* \begin{pmatrix} u_0 + \tilde{u}_0 \\ x_1 + \tilde{x}_1 \end{pmatrix} \end{pmatrix} \tag{5.14}$$

Likewise, the graphs of P and P^* can be written as

$$\mathcal{G}_{P,\bar{w}_1} := \left\{ \begin{pmatrix} \begin{pmatrix} u_0 + \bar{u}_0 \\ \phi(x_1 + \bar{x}_1) \end{pmatrix} \\ M \begin{pmatrix} u_0 + \bar{u}_0 \\ \phi(x_1 + \bar{x}_1) \end{pmatrix} \end{pmatrix} : \left\| \begin{matrix} u_0 \\ x_1 \end{matrix} \right\| < \infty \right\},$$

$$\mathcal{G}_{P^*,\tilde{w}_1} := \left\{ \begin{pmatrix} \begin{pmatrix} u_0 + \tilde{u}_0 \\ \phi(x_1 + \tilde{x}_1) \end{pmatrix} \\ M^* \begin{pmatrix} u_0 + \tilde{u}_0 \\ \phi(x_1 + \tilde{x}_1) \end{pmatrix} \end{pmatrix} : \left\| \begin{matrix} u_0 \\ x_1 \end{matrix} \right\| < \infty \right\}.$$

The connection between graphs means their gaps satisfy

$$\begin{aligned} \delta_{\bar{w}_1,\tilde{w}_1}(M, M^*) &= \inf_{\Psi} \sup_{x \in \mathcal{G}_{M,\bar{w}_1}} \frac{\|(\Psi - I)x\|_{\bar{w}_1}}{\|x\|} \qquad (5.15) \\ &= \inf_{\Psi} \sup_{x \in \mathcal{G}_{P,\bar{w}_1}} \frac{\|(\Psi - I)\phi(x)\|_{\bar{w}_1}}{\|\phi(x)\|} \\ &\leq \inf_{\Psi} \sup_{x \in \mathcal{G}_{P,\bar{w}_1}} \frac{\|(\Psi - I)x\|_{\bar{w}_1}}{\|x\|} \sup_{x \neq 0} \frac{\|\phi(x)\|_{\bar{w}_1}}{\|x\|} \\ &\leq \inf_{\Psi} \sup_{x \in \mathcal{G}_{P,\bar{w}_1}} \frac{\|(\Psi - I)x\|_{\bar{w}_1}}{\|x\|} \frac{1}{\epsilon} \\ &= \delta_{\bar{w}_1,\tilde{w}_1}(P, P^*) \frac{1}{\epsilon} \qquad (5.16) \end{aligned}$$

where we have used from (5.12)

$$\begin{aligned} \frac{1}{\epsilon}|x| \geq & |f^{-1}(x + \bar{x}) - f^{-1}(\bar{x})|, \qquad \forall x, \bar{x} \qquad (5.17) \\ \Rightarrow \frac{1}{\epsilon}|x| \geq & |\phi(x + \bar{x}) - \phi(\bar{x})|, \qquad \forall x, \bar{x} \qquad (5.18) \\ \Rightarrow \frac{1}{\epsilon} \geq & \sup_{x,\bar{x}} \frac{|\phi(x + \bar{x}) - \phi(\bar{x})|}{|x|}. \qquad (5.19) \end{aligned}$$

So stability criterion (5.13) is satisfied if

$$\delta_{\bar{w}_1,\tilde{w}_1}(P, P^*) \frac{1}{\epsilon} < \|\Pi_{M//N}\|_{\bar{w}_0}^{-1} \qquad (5.20)$$

which yields (3.7). □

Theorem 5.2 states that the gap metric between plant P^* and plant P must be less than $\epsilon\|\Pi_{P//C}\|_{\bar{w}_0}^{-1}$ to ensure stability of the closed-loop $[P^*, C]$. Similar to the robust stability margin in (3.8), this therefore defines a 'ball' of plants that are stabilised by C with centre P and radius

$$b_{P,C} = \begin{cases} \epsilon\|\Pi_{P//C}\|_{\bar{w}_0}^{-1} & \text{for } \epsilon\|\Pi_{P//C}\|_{\bar{w}_0}^{-1} > 0, \\ 0 & \text{otherwise} \end{cases} \qquad (5.21)$$

as shown in Figure 5.8. The bound (5.7) shows how the size of the ball's radius depends on the RC update convergence rate η, and operator norms. For example, as η is reduced, the radius grows and the system is more robust to modelling error.

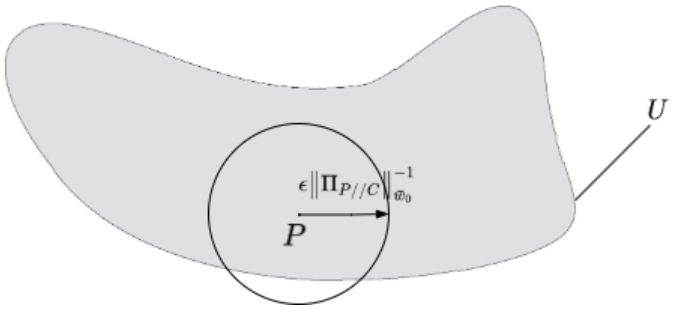

FIGURE 5.8: Ball of true plants in uncertainty space $\mathcal{U}$ that are stabilised by controller C.

The robustness results derived in this section are now used to develop the Hammerstein MMSRC framework.

5.4 Hammerstein MMSRC Structure

The robust stability margin $b_{P,C}$ in (5.21) is also small, limiting RC to stabilizing only a small subset of the plant uncertainty set $\mathcal{U}$. To enhance this robustness, the MMSRC framework developed in Chapter 4 is now extended to apply to Hammerstein systems, grounded in the preceding gap metric analysis.

Figure 5.9 illustrates the Hammerstein structure of MMSRC. The core idea is still select a set of 'candidate' plant models $\mathcal{P} = \{P_1, \cdots, P_n\}$, each potentially representing the true plant and structured as a Hammerstein system $P_i = (f_i, G_i)$. A design procedure, $C_i = K(P_i)$, assigns a RC scheme $C_i = (\phi_i, R_i)$ to each plant P_i. This produces the controller set $\mathcal{C} = \{C_1, \cdots, C_n\}$. The true plant $P^* = (f^*, G^*)$ represents the unknown true plant. The estimator $E(P_i)$ computes a residual, r_{P_i}, for each plant model $P_i \in \mathcal{P}$, which quantifies how closely the model aligns with the observed data (u_2, y_2). The minimiser W selects the index i of the plant model with the smallest residual, which is then used to switch the corresponding linearising RC scheme $C_i = (\phi_i, R_i)$ into closed-loop. A switching delay operator D is included to prevent overly rapid switching between controllers.

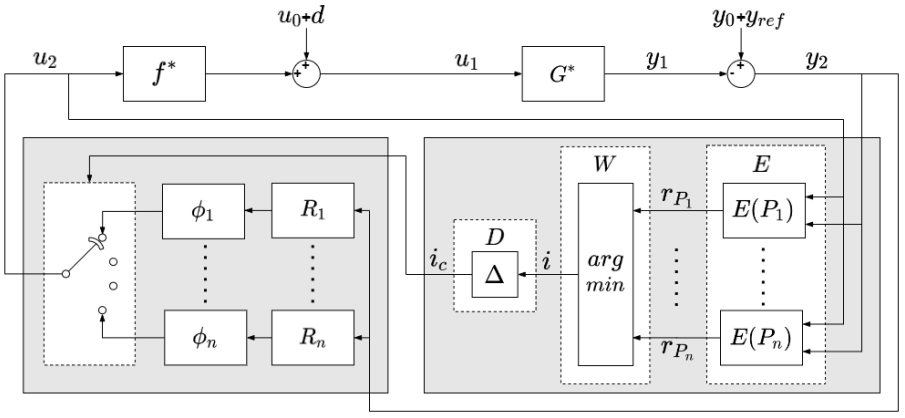

FIGURE 5.9: MMSRC structure showing true plant $P^* = (f^*, G^*)$, estimator bank, and switched controller.

5.4.1 MMSRC Robust Performance Conditions

Similar to Section 4.2.1, the stability conditions for Hammerstein MMSRC need to be defined (Freeman, 2017).

Theorem 5.3. *Let the true plant $P^* \in \mathcal{U}$. Let $\mathcal{P}$ be a candidate model set and $C_i = K(P_i)$, $P_i \in \mathcal{P}$ be a control design procedure defined by (5.3), (2.5). Then the Hammerstein MMSRC implementation stabilises the true plant provided the following two conditions are satisfied:*

1. **Candidate plant condition:**

$$\exists P_i \in \mathcal{P},\ s.t.\ \vec{\delta}_{\bar{w}_1,\tilde{w}_1}(P_i, P^*) < \rho(\mathcal{P},\mathcal{C},\mathcal{U},\Delta) \tag{5.22}$$

where ρ is a positive scalar function dependent on the $\mathcal{C}$, $\mathcal{P}$, $\mathcal{U}$ and delay Δ.

2. **Candidate controller condition:**

$$\exists C_i \in \mathcal{C},\ s.t.\ \|\Pi_{P//C_i}\|_{\bar{w}_0} < \infty,\ \forall P \in \mathcal{U} \tag{5.23}$$

In particular, the plant signals of the switched closed-loop system $[P^*, K(P_{i_c})]$ are bounded as

$$\|w_1\| < \upsilon(\mathcal{P},\mathcal{C},\mathcal{U})\|w_0\|, \tag{5.24}$$

where υ is a positive scalar function.

Criterion 1 specifies a minimum radius of gap balls covering the uncertainty space, and hence dictates the number of plant models required. This concept is similar to

Criterion 1 in Theorem 6.1., except that Theorem 7.3 describes Hammerstein plants and Hammerstein uncertainty space. Criterion 1 of Theorem 7.3. is illustrated in Figure 5.10.

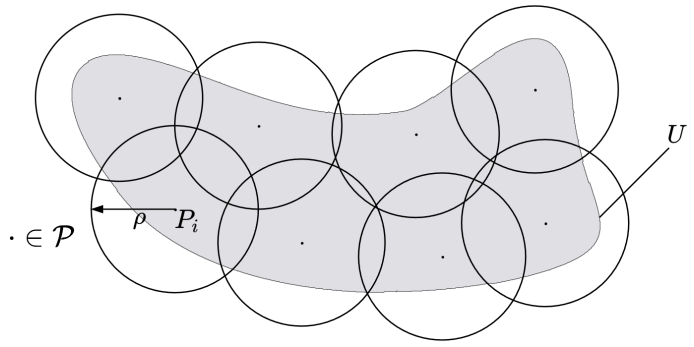

FIGURE 5.10: Criterion (5.22): Uncertainty space $\mathcal{U}$ is covered by gap metric balls of radius ρ and centre $P_i \in \mathcal{P}$.

Criterion 2 states that a stabilizing controller must exist for each plant within the uncertainty space $\mathcal{U}$. It is illustrated in Figure 5.11. Note that for the Hammerstein structure, the robust stability margin of the controller is given by (5.7), rather than by (3.2) and (3.8) employed in Criterion 2 of Theorem 6.1.

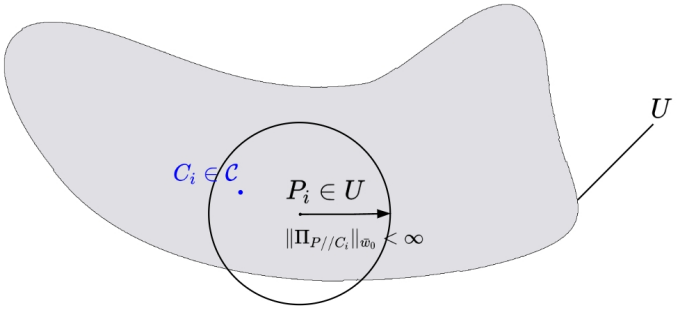

FIGURE 5.11: Criterion (5.23): $\forall P \in \mathcal{U}$, there exists $C_i \in \mathcal{C}$ that stabilises it.

5.4.2 Candidate Model Set Design

Computing $\rho(\mathcal{P}, \mathcal{C}, \mathcal{U}, \Delta)$ entails a large computational burden, and is also conservative (i.e. more candidate plants are specified than required). To address this, an efficient design procedure is now developed that avoids calculating ρ.

Firstly, criterion (5.23) stipulates that each plant within the uncertainty set $\mathcal{U}$ must be stabilized by at least one controller from $\mathcal{C}$. The straightforward approach to satisfy this is using Theorem 5.2 to design a minimal candidate plant set $\mathcal{P}$ whose gap balls (each with radius $b_{P_i,K(P_i)}$ given by (5.21)) cover the uncertainty space $\mathcal{U}$. This satisfies criterion (5.23), however, criterion (5.22) may not be satisfied.

As in Section 4.3.1, (5.22) can be satisfied by introducing a tunable weight. Suppose the radius is reduced to

$$\rho = \alpha b_{P_i,K(P_i)}, \tag{5.25}$$

using the tuning parameter $0 < \alpha \leq 1$, then as $\alpha \to 0$, more gap balls will be included to cover the same set $\mathcal{U}$, and there will always come a points at which (5.22) is satisfied. By treating α as a tunable gain, there is no need to calculate ρ. This leads to a pragmatic procedure for constructing a candidate model set $\mathcal{P}$ given in Design Procedure 5.

Design Procedure 5 Build a candidate model set for Hammerstein structure

Require: Uncertainty set $\mathcal{U}$ containing P^*, RC design K, gain α, tremor period length N.

1: Compute a set of n candidate models $\mathcal{P} = \{(f_1, G_1), \ldots, (f_n, G_n)\}$ covering $\mathcal{U}$ with fine resolution.
2: For each $P_i = (f_i, G_i)$, design a function ϕ_i and a RC update R_i that satisfies the stability condition (2.16) or (2.17).
3: For each P_i, C_i, compute robust performance radius $\alpha b_{P_i,K(P_i)}$, where $0 < \alpha \leq 1$ is a tunable gain.
4: Check whether the union of gap balls covers $\mathcal{U}$. If not, return to step 2 to tune the RC update to increase the radius or to step 1 to increase the candidate set resolution.
5: Implement MMSRC. If the performance is poor, return to step 3 to reduce the gain α.

This is similar to Design Procedure 1 in Section 4.3.1, but both the plants and controllers are extended into Hammerstein structures, with the robust stability margin defined by (5.21).

5.4.3 Estimator Design

For each plant model, $P_i = (f_i, G_i) \in \mathcal{P}$, an estimator computes a residual, r_{P_i}, equal to the size of the minimum disturbance (u_0, y_0) necessary to explain the measurement (u_2, y_2) assuming that P_i is the true plant. Specifically, suppose $\mathcal{N}_{P_i}^{[0,k]}(u_2, y_2)$ is the set of all disturbances (u_0, y_0) compatible with plant P_i, the measured signals (u_2, y_2) and the signal connections in Figure 5.2 over samples $[0, k]$. The residual on sample k is then defined as

$$r_{P_i}[k] = \inf\{r \geq 0 | r = \|v_0\|, v_0 \in \mathcal{N}_{P_i}^{[0,k]}(u_2, y_2)\}. \tag{5.26}$$

If G_i is represented by the state-space triplet $(A_{P_i}, B_{P_i}, C_{P_i})$, then it is shown in (Willems, 2004) that the residual can be computed as

$$r_{P_i}(k) = \left[\sum_{\tau=0}^{k} \lambda^{k-\tau} \left\|y_2(\tau) - y_{ref}(\tau) + \tilde{y}_{P_i}(\tau)\right\|^2_{\left[C_{P_i}\Sigma_{P_i}(\tau)C_{P_i}^\top + I\right]^{-1}}\right]^{\frac{1}{2}} \tag{5.27}$$

where $0 < \lambda \leq 1$ is a tunable weight used to place less emphasis on residuals which occurred further back in time. The term $\tilde{y}_{P_i}$ is generated by the infinite-horizon Kalman

filter

$$\begin{aligned}
\hat{x}_{P_i}(\tau+\frac{1}{2}) =& \hat{x}_{P_i}(\tau) + \Sigma_{P_i}(k)C_{P_i}^\top \left[C_{P_i}\Sigma_{P_i}(\tau)C_{P_i}^\top + I\right]^{-1} \\
& [y_{ref}(\tau) - y_2(\tau) - C_{P_i}\hat{x}_{P_i}(\tau)] \\
\Sigma_{P_i}(\tau+\frac{1}{2}) =& \Sigma_{P_i}(\tau) - \Sigma_{P_i}(k)C_{P_i}^\top \left[C_{P_i}\Sigma_{P_i}(\tau)C_{P_i}^\top + I\right]^{-1} \\
& C_{P_i}\Sigma_{P_i}(\tau) \\
\hat{x}_{P_i}(\tau+1) =& A_{P_i}\hat{x}_{P_i}(\tau+\frac{1}{2}) + B_{P_i}(f_i(u_2(\tau)) + d(\tau)) \\
\Sigma_{P_i}(\tau+1) =& A_{P_i}\Sigma_{P_i}(\tau+\frac{1}{2})\hat{A}_{P_i}^\top + B_{P_i}B_{P_i}^\top \\
\tilde{y}_{P_i}(\tau) =& C_{P_i}\hat{x}_{P_i}(\tau)
\end{aligned} \tag{5.28}$$

with initial conditions $\Sigma_{P_i}(0) = 0$, $\tilde{x}_{P_i}(0) = 0$ and sample $\tau \in [0, k-1]$. Since the controlled plant is extended to a Hammerstein structure, $u_2(\tau)$ in (4.5) is replaced by $f_i(u_2(\tau))$. This also requires knowing d. If d is unknown, an augmented estimator structure is required and is developed in Section 6.2.

The switch algorithm is consistent with that described in Section 4.3.3.

5.5 Summary

In this chapter, the previously used idealized linear wrist model for simulation is extended into a more realistic Hammerstein model. Building upon this foundation, a Hammerstein system is established, comprising a wrist model with nonlinear components and a controller featuring a nonlinear inverse function. Based on this Hammerstein system, a new robust stability theory is derived. This provides guiding principles for the stability conditions of the Hammerstein MMSRC structure and the design of the candidate model set. The extended nonlinear system also informs the design of the new estimator. These results collectively lay the groundwork for experimental testing.

Chapter 6

Experiment Procedure and Results

Chapter 5 introduced the Hammerstein wrist model and extended RC design for this class of system. It derived robust performance guarantees and expanded the MMSRC framework for application to Hammerstein systems. This chapter focuses on applying this framework in practice. To do this, it will extend the previous model identification approach, and establish how an uncertainty space can be built for Hammerstein systems. It will then specify an augmented estimator structure that removes the need for the tremor signal to be known or identified in advance. The experimental system and set-up procedures will then be presented, followed by comparative real-world tests evaluating the effectiveness of both RC and MMSRC in suppressing artificial wrist tremors, with comprehensive performance assessments.

6.1 Model Identification and Uncertainty Space Design

This section develops procedures to identify the nominal model needed to design conventional RC, as well as establishing the uncertainty set, $\mathcal{U}$, for use in MMSRC.

6.1.1 Parameterized Model

The wrist model structure was defined in Figure 5.1, and the first step is to determine a practical procedure to identify the parameters appearing within it. Within FES research, the nonlinear muscle activation dynamics are consistently characterized as a cascade of static nonlinearity and linear dynamics (Le et al., 2010). This static IRC nonlinearity

can be precisely described by the following form (Freeman et al., 2009):

$$\begin{aligned} h_{IRC,fcr}(u_{fcr}) &= c_{1,fcr}\left(\frac{e^{c_{2,fcr}u_{fcr}}-1}{e^{c_{2,fcr}u_{fcr}}+c_{3,fcr}}\right), \\ h_{IRC,ecr}(u_{ecr}) &= c_{1,ecr}\left(\frac{e^{c_{2,ecr}u_{ecr}}-1}{e^{c_{2,ecr}u_{ecr}}+c_{3,ecr}}\right), \end{aligned} \tag{6.1}$$

where $\{c_{i,fcr}, c_{i,ecr}\}_{i=1,2,3}$ are constant parameters. These forms then are combined to give function f, defined by (5.1).

The linear part of the muscle H_{LAD} is a critically damped second order system (Freeman et al., 2009) given by

$$H_{LAD}(s) = \frac{\omega_n^2}{s^2 + 2s\omega_n + \omega_n^2} \tag{6.2}$$

where ω_n is the natural frequency (Verstappen et al., 2012).

The RBD of the joint and connective tissue takes the transfer function form (Verstappen et al., 2012; Freeman et al., 2015)

$$H_{RBD}(s) = \frac{1}{I_p s^2 + bs + k_p} \tag{6.3}$$

where I_p represents inertia, b represents damping and k_p represents stiffness. Forms (6.2) and (6.3) are the same as used in the linear model of Section 3.4.1.1. Their series connection then gives operator G, defined by (5.2).

Based on (6.1), (6.2), and (6.3), along with the artificially set coactivation levels, all parameters required for identifying the model $P = (f, G)$ illustrated in Figure 5.2 have been determined.

6.1.2 Identification of Nominal Model

Parameters $\{c_{i,fcr}, c_{i,ecr}\}_{i=1,2,3}$ of f can be fitted using the approach of (Freeman et al., 2009) which involves using a torque sensor to measure the intermediate signal u_1. Specifically, $\bar{u}_{fcr} = \bar{u}_{ecr} = 0$ are set in function h_{cc} and an FES signal $\tilde{u}_2$ is used to slowly activate each muscle across the domain of f, $[-u_{max}, u_{max}]$. The isometric torque around the wrist, $\tilde{u}_1$, is measured and the model parameters are identified by solving

$$\min_{\{c_{i,fcr}, c_{i,ecr}\}_{i=1,2,3}} \sum_{t=1}^{N} \left(f(\tilde{u}_2(t)) - \tilde{u}_1(t)\right)^2 \tag{6.4}$$

where $t = 1, \ldots, N$ represents the number of sampling points within the identification test.

Appropriate coactivation levels satisfying $h_{IRC,fcr}(\bar{u}_{fcr}) = h_{IRC,ecr}(\bar{u}_{ecr})$ are then chosen to equalize the opposing torques. As mentioned in Section 3.4.1, the dead zone of the IRC is removed when $\bar{u}_{fcr}, \bar{u}_{ecr}$ reaches appropriate levels. In this case, f becomes continuous, monotonically increasing, and has a well defined inverse function.

Having identified f, the components of G are identified by applying a sufficiently exciting FES sequence, $\tilde{u}_2(t)$, and recording the resulting angular movement $\tilde{y}_2(t)$ over samples $t = 1, \ldots, N$. The parameters of (6.2) and (6.3) are then computed by minimising the cost function

$$\min_{(\omega_n, I_p, b, k_p)} \sum_{t=1}^{N} \left(G(q)f(\tilde{u}_2(t)) - \tilde{y}_2(t)\right)^2 \tag{6.5}$$

where $G(q)$ is the discretised form of $G(s)$.

6.1.3 Establishing the Model Uncertainty Set

The model uncertainty set $\mathcal{U}$ is computed by conducting the above identification tests multiple times to capture the maximum possible variation in all parameters.

Suppose a collection of M sufficiently varied identification data sets has been collected. For each data set (6.4) and (6.5) are solved to obtain optimum parameter sets $\{\{c_{i,fcr,j}, c_{i,ecr,j}\}_{i=1,2,3}, \omega_{n,j}, I_{p,j}, b_j, k_{p,j}\}_{j=1,\ldots,M}$.

Then the uncertainty set is computed to contain all these individual models:

$$\begin{aligned}\mathcal{U} := \big\{ & P = (f, G) \mid f = (3.22), (6.1), (5.1),\ G = (6.2), (6.3), (5.2), \\ & \{c_{i,fcr} \in [c^m_{i,fcr}, c^M_{i,fcr}], c_{i,ecr} \in [c^m_{i,ecr}, c^M_{i,ecr}]\}_{i=1,2,3}, \\ & \omega_n \in [\omega_n^m, \omega_n^M], I_p \in [I_p^m, I_p^M], b \in [b^m, b^M], k_p \in [k_p^m, k_p^M]\big\}\end{aligned} \tag{6.6}$$

where $\omega_n^m := \min\{\omega_{n,i}\}$, $\omega_n^M := \max\{\omega_{n,i}\}$ and likewise for I_p, b, k_p, $c_{i,fcr}$ and $c_{i,ecr}$.

6.2 Estimator Design for Uncertain Tremor

Tremor signal d can be identified in practice by direct measurement of the uncontrolled wrist angle and Fourier decomposition. However, its amplitude or even frequency may vary over time, and re-identification may not be feasible. To address this, it is possible to design a different estimator (5.27), (5.28) for every conceivable signal d, however this would quickly become computationally impractical. Instead the tremor variation can be subsumed within the plant model structure, so that selecting the 'best' plant also includes selecting the tremor signal that most closely matches measured data.

This is achieved by replacing the plant structure of Figure 5.2 by the augmented structure of Figure 6.1. This mimics how the tremor is propagated physiologically by the nervous system.

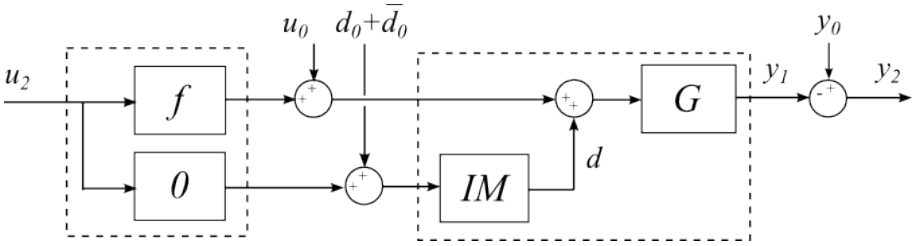

FIGURE 6.1: Augmented plant (f, G) embedding disturbance in tremor.

Here IM is an N-periodic internal model without a Q filter, i.e. $IM(q) = (I - q^{-N})^{-1}$. Bias term $\bar{d}_0$ provides the initial conditions needed to generate the tremor d, i.e.

$$\bar{d}_0(k) = \begin{cases} d(k), & k = 1, \ldots, N, \\ 0, & k > N \end{cases} \tag{6.7}$$

which produces the sustained oscillation $(IM\bar{d}_0)(k) = d(k)$, $k > N$. The key idea is that the additional disturbance d_0 is then able to fine-tune the tremor, allowing it to slowly vary over time. This signal will be estimated by the Kalman filter, in exactly the same way as the plant disturbances u_0, y_0. This model of tremor is attractive since it only requires a small disturbance signal d_0 to modify the shape of tremor d, meaning that it will not interfere with the normal operation of the Kalman Filter to select the 'best' plant model P_i.

This structure fits into MMSRC in Figure 5.9, by replacing f, G, with augmented versions $(f, 0)^\top$, $G(I, IM)$ respectively. Signals u_0, d are replaced by $(u_0, d_0)^\top$, $(0, \bar{d}_0)^\top$. The estimator then has the additional disturbance variable d_0 which means it can better match the observed tremor. In (5.26) the term $\mathcal{N}_{P_i}^{[0,k]}(u_2, y_2)$ is now the set of all disturbances (u_0, d_0, y_0) compatible with plant P_{P_i}, the measured signals (u_2, y_2) and the signal connections in Figure 6.1 over samples $[0, k]$.

To solve (5.26), the state-space triple for G_i is modified from $(A_{P_i}, B_{P_i}, C_{P_i})$ to

$$\left(\begin{bmatrix} A_{P_i} & B_{P_i} C_N \\ 0 & A_N \end{bmatrix}, \begin{bmatrix} B_{P_i} & 0 \\ 0 & B_N \end{bmatrix}, \begin{bmatrix} C_{P_i} & 0 \end{bmatrix} \right), \tag{6.8}$$

where the state-space triple (A_N, B_N, C_N) implements IM. These new forms are substituted into (5.27), (5.28) and the term $f_i(u_2(\tau)) + d(\tau)$ is replaced by $\begin{bmatrix} f_i(u_2(\tau)) \\ \bar{d}_0 \end{bmatrix}$.

Remark 6.1. A scalar gain can be applied to IM to adjust its sensitivity, effectively varying how quickly the tremor is allowed to deviate from its initial value. It is also

possible to add more internal models in parallel, each with a different period to account for multiple frequencies.

6.3 Experimental System

This section presents the experimental setup designed to evaluate the performance and robustness of the proposed MMSRC framework under realistic, variable conditions. The primary objective is to test whether MMSRC can maintain effective tremor suppression in the presence of model uncertainty, muscle fatigue, and electrode misalignment—scenarios commonly encountered in practical FES applications. To achieve this, a controlled experimental environment was established using a wrist rig and artificially induced tremor, enabling repeatable and quantifiable assessments of controller performance. This experimental test scenario closely matches previous studies using RC for tremor suppression (Verstappen et al., 2012; Freeman et al., 2015; Copur et al., 2019; Zhang et al., 2022a,b, 2024). This system is described next.

6.3.1 Wrist Rig

The experimental equipment comprises four parts: a PC and real-time computing hardware (Speedgoat target machine, Speedgoat Inc. USA), FES stimulator (Odstock Medical Limited, UK), surface electrodes (Pals PLUS, $5 \times 5cm$) and the instrumented wrist rig described in (Turk et al., 2008) and shown in Figure 6.2a) which supports the participant's arm and restricts movement to only the horizontal plane.

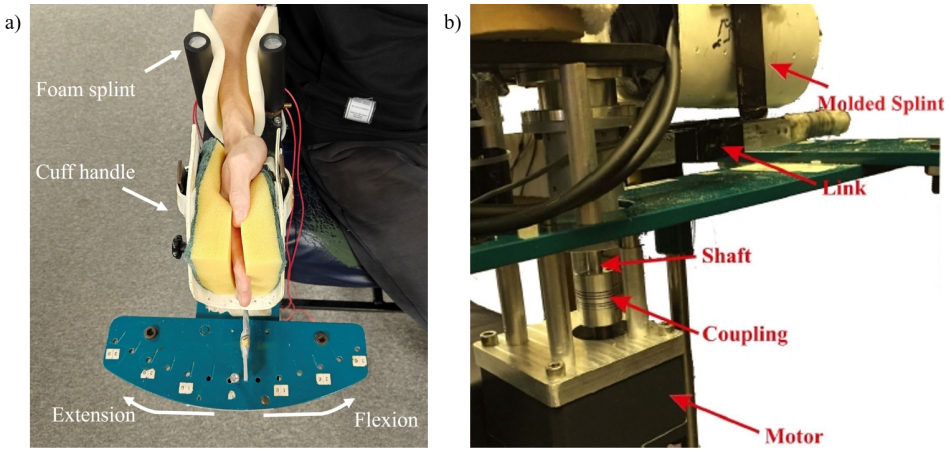

FIGURE 6.2: a) Experimental set-up showing test participant seated in the wrist rig, b) artificially induced tremor device.

The wrist angle is measured by a resolver with a range of $[-90°, 90°]$, and transmitted in real-time to the PC via Speedgoat hardware. The controller generated by compiling code and simulation files on the PC produces two $40Hz$ pulse-width modulated (PWM)

square wave signals based on these inputs. The pulse widths correspond to the control signals u_{fcr} and u_{ecr} in Figure 5.1. These signals have a maximum value of $u_{max} = 300\mu$s and are sent to the stimulator which outputs the two channels of high voltage FES pulse-trains. The sampling frequency in all tests is $40Hz$.

6.3.2 Induced Tremor

Since the study aimed to evaluate controller performance under controlled and repeatable conditions, healthy participants were recruited to avoid the variability and ethical complexities associated with patient populations. This allowed for systematic testing of controller robustness without confounding factors such as medication effects or comorbid neurological symptoms.

Since the experiment was conducted on healthy participants, tremor was artificially introduced using a DC motor (Davitu Z5D40) mounted beneath the armrest, as shown in Fig. 6.2b). A tremor frequency of 1 Hz was selected for the artificially induced tremor primarily because it falls within the typical range of pathological tremors, such as intention tremor. Secondly, since MMSRC employs the gradient RC algorithm, a 1 Hz tremor corresponds to a period of $N = 200$ samples when the sampling time is $T_s = 0.005$ s. This ensures that the impulse response length m_L of the $L(q)$ filter within each controller C_i is sufficient, thus preventing truncation of the plant model P_i's impulse response. Thereby ensuring that the controller's performance does not degrade. Furthermore, this low tremor frequency facilitates clearer observation of the suppression dynamics and controller adaptation. The motor controller (Maxon Motor ESCON) operated in current model to apply a prescribed torque profile whose frequency was 1 Hz and whose amplitude was set individually for each participant to produce a tremor amplitude of 20°-30°. These parameters replicate low frequency tremors, consistent with damage to the cerebellum. The use of a motor matches the approach used in (Copur et al., 2019), and was found to be much more reliable and comfortable than by stimulating additional muscles, as in (Padilha Lanari Bó et al., 2011). It therefore provides a controllable, repeatable experimental platform. As described in Section 2.4.2, the artificial tremor only approximates pathological tremor: the real tremor has a more complex composition and is characterized by superimposed multi-frequency components, spontaneous amplitude fluctuations, and intricate directional patterns. These differences will be addressed in future studies with people from impaired populations.

6.4 Experimental Procedure

Ethical approval was granted by University of Southampton Ethics and Research Governance Online, ID 82268. Four healthy individuals without motor function impairments

were recruited, meeting the criteria: 1) no motor function impairments or diagnosed systemic diseases; 2) no cardiac pacemaker or other implanted electronic devices; 3) no cognitive or visual impairments; 4) no diagnosed skin conditions; 5) able to provide informed consent. All participants signed a consent form. Participants are denoted A, B, C and D. The physiological information of the participants is presented below. Where

TABLE 6.1: Participant physical characteristics

Participant	Gender	Age (years)	Height (cm)	Weight (kg)	BMI (kg/m^2)
A	Male	45	177	74	23.6
B	Male	27	175	54	17.6
C	Male	30	175	80	26.1
D	Male	28	186	106	30.6

BMI stands for body mass index. It is a numerical value calculated from a person's weight and height, providing a standardized measure of body size and composition. The formula is BMI = weight (kg) / [height (m)]^2 (Zierle-Ghosh and Jan, 2023). It demonstrated a diverse range of participant physiques. The calculated BMI values showed that the participant pool covered a spectrum from the lower end of the underweight category (Participant B, BMI = 17.6) to the obese category (Participant D, BMI = 30.6).

The specific process of the experiment is as follows:

1) Test setup: Each participant placed their arm in the wrist rig and two pairs of FES surface electrodes were applied to their FCR and ECR muscles. The amplitude of each stimulation signal was then set to a comfortable level. Each participant was instructed to relax and apply no volitional action throughout subsequent tests.

2) Identification of nominal wrist model: A nominal plant model was identified for each participant using the tests described in Section 6.1.2. In particular, f was found by locking the wrist rig and applying a slow FES ramp to each muscle, with $\tilde{y}_1$ measured via a strain gauge. Then G was found by applying a series of sine wave inputs $\{x_2(t)\}_{t=1}^{N}$ composed of frequencies ranging from 0.9 to 1.1 Hz.

3) RC design: For comparison with MMSRC regarding suppression effectiveness, standard RC updates were designed using the nominal models of the four participants identified above. The gradient RC algorithm in Section 2.6.3 was selected for designing the controller because it demonstrated better robustness in the simulations presented in Chapter 3. The design procedure for the RC is shown in Design Procedure 1. However, since the robust stability margin is overly conservative, the performance index described in (3.25) was selected as the criterion for choosing controller parameters. While satisfying stability condition (2.17), the learning gain γ of the gradient RC was tuned through simulations to maximize the performance index as much as possible. The designed conventional repetitive controller is denoted as **RC**.

4) Establishing the uncertainty space: uncertainty set $\mathcal{U}$ was established for each participant by repeating the identification test of Section 6.1.2 approximately every 3 minutes, for a total of $M = 5$ sets. Nearly 15 minutes of electrical stimulation was sufficient to induce muscle fatigue, causing the model to change. Then an uncertainty space with $M = 5$ described in Section 6.1.3 was established.

5) MMSRC design: Design MMSRC for each participant's uncertainty space.

- In step 1 of Design Procedure 5, five models identified in the previous experimental procedure were selected to establish the candidate model set, obtaining $\mathcal{P} = \{(f_1, G_1), \ldots, (f_5, G_5)\}$.
- In step 2 of Design Procedure 5, for each $P_i = (f_i, G_i)$, inverse function ϕ_i was designed to cancel the nonlinear part f_i. Then the learning gain γ of the gradient RC was tuned to satisfy the stability condition (2.17).
- In step 3 and step 4 of Design Procedure 5, the robust stability margin was replaced by the performance index due to its excessive conservatism. It was ensured that the performance index for each controller was greater than $1-\alpha$. This computation was performed for each participant using two different values of α. A value of $\alpha = 1$ was used to produce a coarse candidate model set formed of $n = 5$ models. Then α was reduced to produce a set of 24 candidate models. The MMSRC controllers designed using these model sets will be denoted **MMSRC5** and **MMSRC24** respectively.
- To mimic realistic conditions in which the tremor may be unknown or change over time, the approach of Section 6.2 was used to design the estimator for each $P_i \in \mathcal{P}$.

6) Experimental tests: The artificial tremor was then activated, and the following experimental tests were conducted on four participants using **RC**, **MMSRC5** and **MMSRC24**:

- The **ideal conditions test** simply applied three controllers to the identified wrist with the artificial tremor for 120 seconds.
- The prolonged **muscle fatigue test** implemented controllers on each participant's wrist for tremor suppression testing lasting up to 15 minutes (sufficient to induce muscle fatigue in the wrist).
- Finally, the **misaligned electrodes test** involved changing the position of both sets of electrodes by approximately 2.5–3.5 cm. The electrodes were deliberately displaced along the longitudinal axis of the arm, rather than circumferentially around the arm. This specific displacement direction was chosen for two important reasons: First, in practical future applications, users are most likely to

inadvertently shift the electrodes up or down along the arm while donning or adjusting the wearable device. Second, and more critically, since the electrodes must maintain contact with the specific motor points of the ECR and FCR muscles to effectively generate opposing torques, longitudinal displacement represents the most physiologically relevant misalignment scenario. Circumferential displacement would likely place the electrodes over entirely different muscle groups, fundamentally altering the system dynamics beyond the scope of the intended uncertainty space $\mathcal{U}$. Following electrode repositioning, wrist tremor suppression testing was conducted for 120 seconds.

In the above experiments, a rest period of 15 minutes occurred between all tests to ensure fair comparison. These tests produced the realistic variability that would occur in a clinic or the participant's own home.

6.5 Experimental Results and Analyses

This section will present the results after executing the experimental procedure from the previous section on participants A, B, C, and D. Analyses will be conducted to evaluate the robustness and energy consumption of the different controllers.

6.5.1 Tremor Suppression Performance

To quantify the tremor suppression of any controlled wrist angle measurements, the performance index described by (3.25) was applied, which is duplicated below:

$$\text{performance index} = \max\left\{1 - \frac{\|y_2\|}{\|\hat{y}_2\|}, 0\right\} \tag{6.9}$$

where $\|y_2\|$ is the 2-norm of all wrist angular movements under the control of RC, and $\|\hat{y}_2\|$ represents the 2-norm of all wrist angular movements with no controller employed. If the tremor is completely suppressed, the performance index is 1, and if it not suppressed or unstable, it is 0. In order to exclude the initial transient response, this will be applied to data after the first 30 seconds of any test. The performance indices were computed for all the experiments of all the participants and the results are shown in Table 6.2. The 'Average' row contains the mean performance of the same controller across experiments involving all four participants. The highest mean values are highlighted in green.

TABLE 6.2: Performance indices for different controllers in different test scenarios

Participant	Ideal Conditions Test			Muscle Fatigue Test			Misaligned Electrodes Test		
	RC	MMSRC5	MMSRC24	RC	MMSRC5	MMSRC24	RC	MMSRC5	MMSRC24
A	0.9313	0.9407	0.9509	0.6572	0.9237	0.9345	0.4807	0.9562	0.9701
B	0.9463	0.9451	0.9617	0.2319	0.9562	0.9635	0	0.9457	0.9633
C	0.9583	0.9608	0.9843	0.2498	0.9542	0.9548	0	0.9646	0.9813
D	0.9140	0.9295	0.9526	0.1421	0.9494	0.9453	0	0.9634	0.9676
Average	0.9375	0.9440	0.9624	0.3203	0.9459	0.9495	0.1202	0.9575	0.9706

A 1 Hz artificial tremor with an amplitude ranging from 20°-30° was introduced to each test in Table 6.2, as illustrated in Figure 6.3.

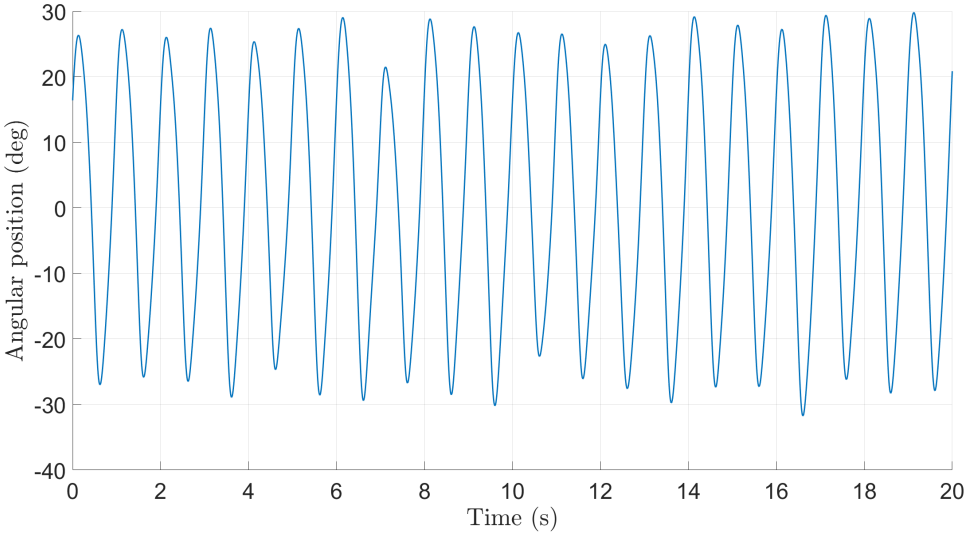

FIGURE 6.3: Artificially induced tremor.

In most **ideal conditions tests**, MMSRC outperformed RC and an increased number of models further improved accuracy. MMSRC5 improved by about 0.7% over RC and MMSRC24 improved by 2.6% over RC.

In the **ideal conditions tests**, the error norms for each period obtained using conventional RC and MMSRC for the four participants are shown in Figure 6.4, Figure 6.5, Figure 6.6 and Figure 6.7.

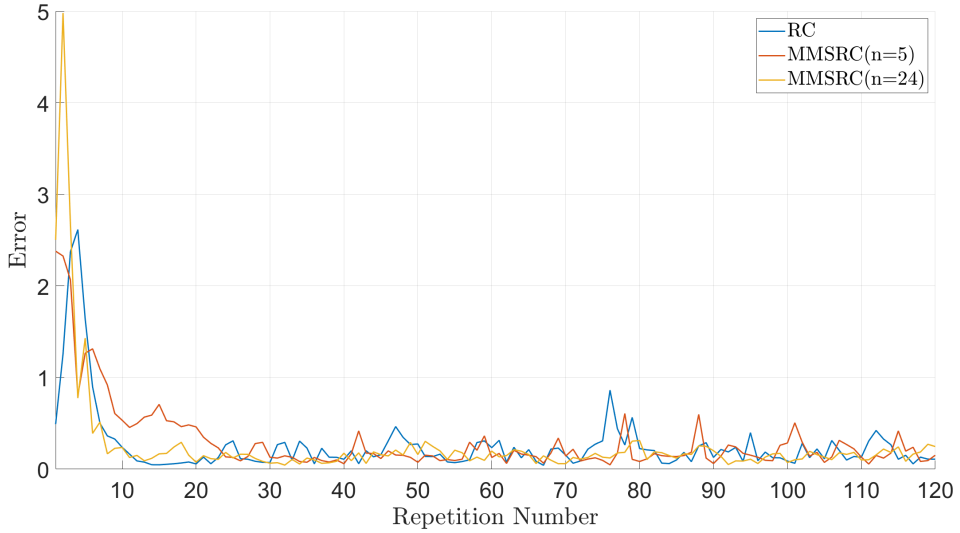

FIGURE 6.4: RC and MMSRC error norms plotted against the period number for the ideal conditions test (Participant A).

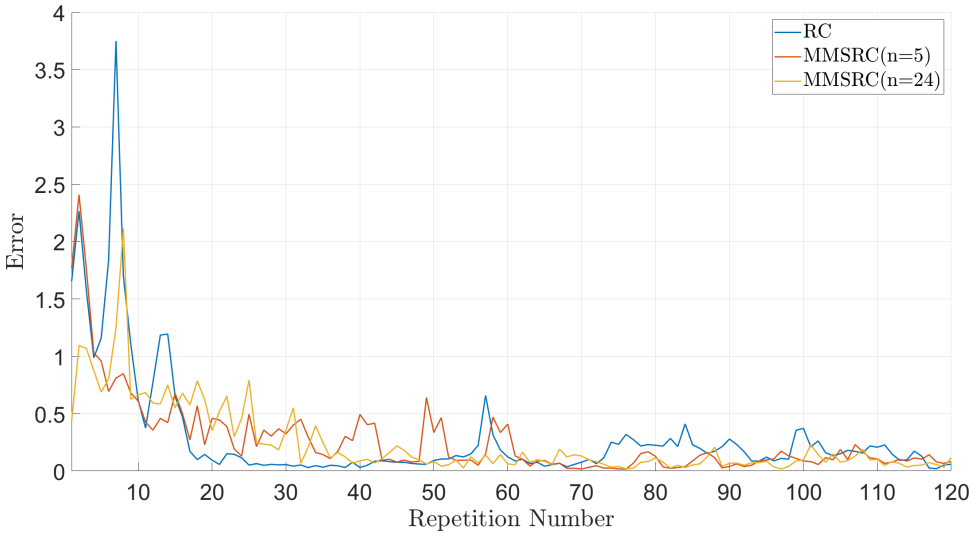

FIGURE 6.5: RC and MMSRC error norms plotted against the period number for the ideal conditions test (Participant B).

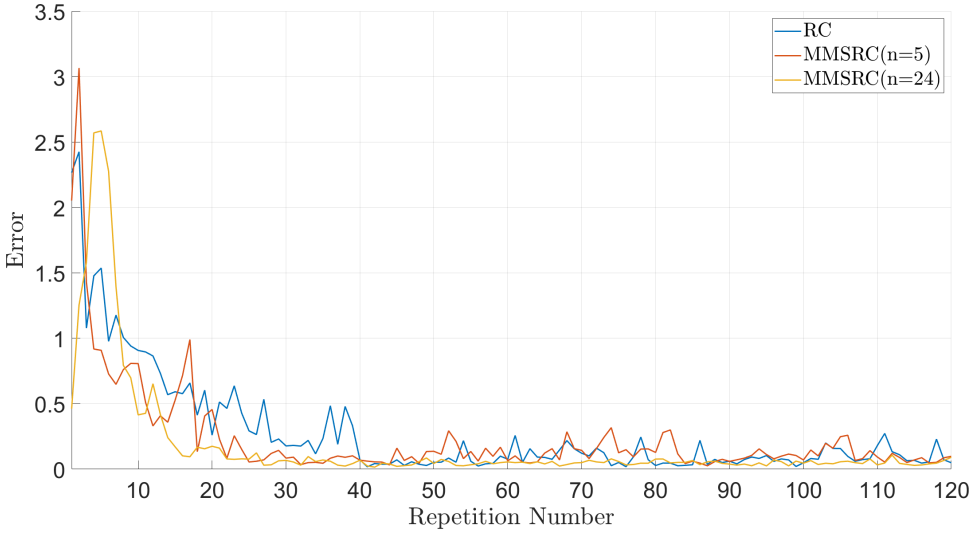

FIGURE 6.6: RC and MMSRC error norms plotted against the period number for the ideal conditions test (Participant C).

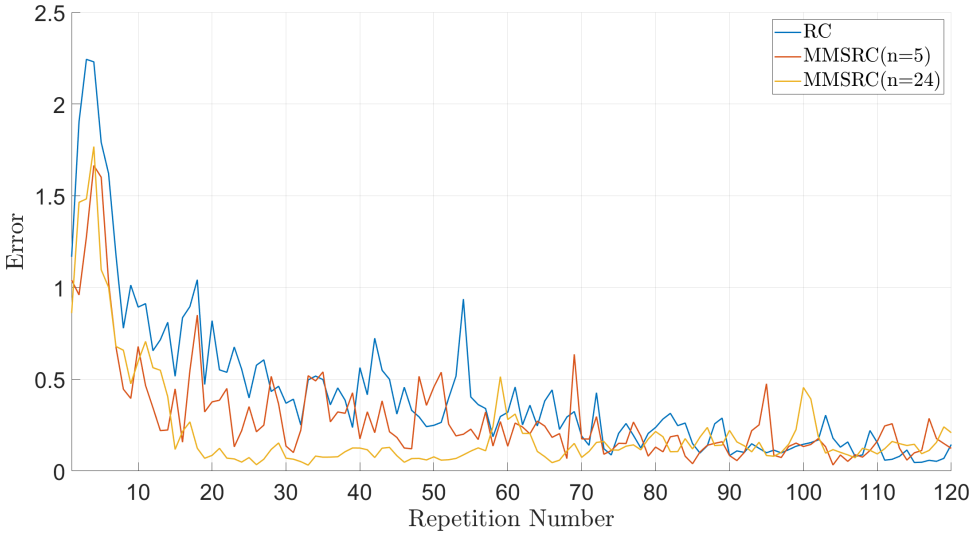

FIGURE 6.7: RC and MMSRC error norms plotted against the period number for the ideal conditions test (Participant D).

The above four figures reveal that, despite varied initial error fluctuations, the three controllers exhibit no significant difference in errors after convergence. Although MMSRC outperforms conventional RC in terms of performance index, this superiority becomes negligible when the model has been identified.

In the **muscle fatigue test**, the performance of standard RC is severely degraded, confirming the findings of Section 5.3 that it lacks robustness and is sensitive to changes in

muscle dynamics. MMSRC adapts to muscle fatigue scenarios through dynamic matching of candidate models, but the increase in the number of models has limited performance enhancement (only 0.3%).

In the **muscle fatigue tests**, the error norms for each period obtained using conventional RC and MMSRC for the four participants are shown in Figure 6.8, Figure 6.9, Figure 6.10 and Figure 6.11.

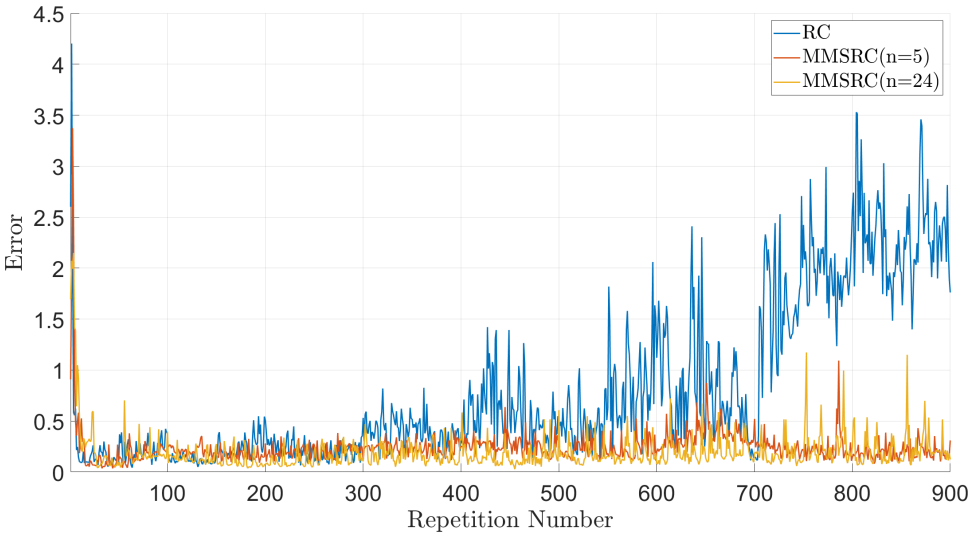

FIGURE 6.8: RC and MMSRC error norms plotted against the period number for the muscle fatigue test (Participant A).

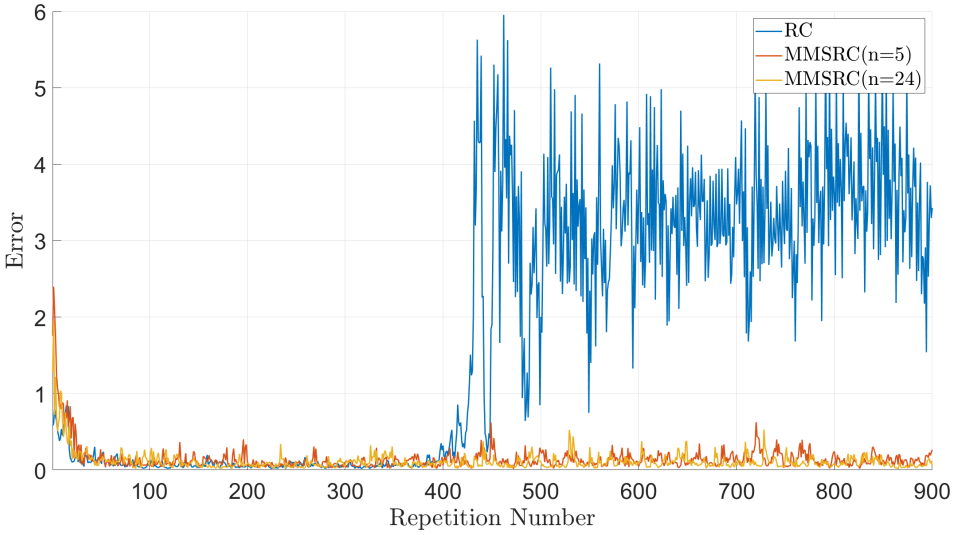

FIGURE 6.9: RC and MMSRC error norms plotted against the period number for the muscle fatigue test (Participant B).

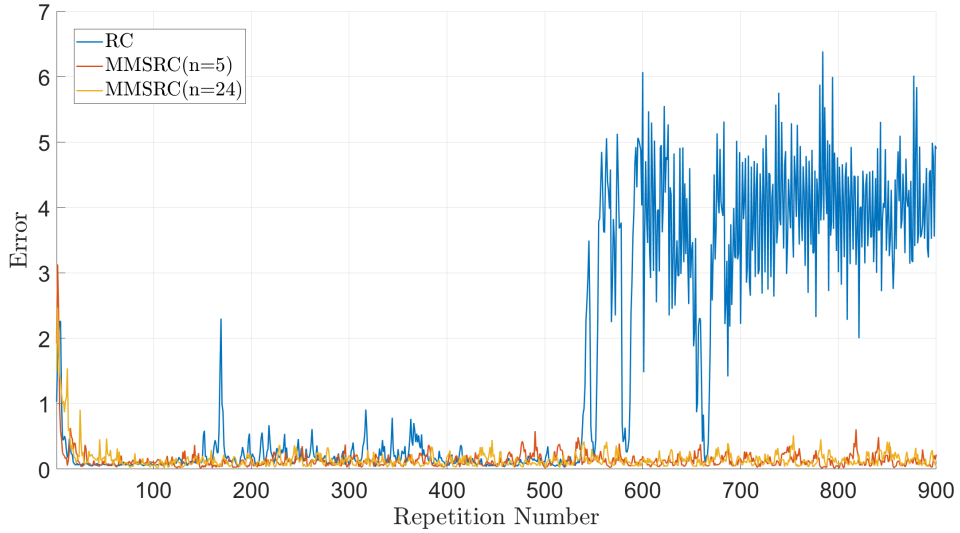

FIGURE 6.10: RC and MMSRC error norms plotted against the period number for the muscle fatigue test (Participant C).

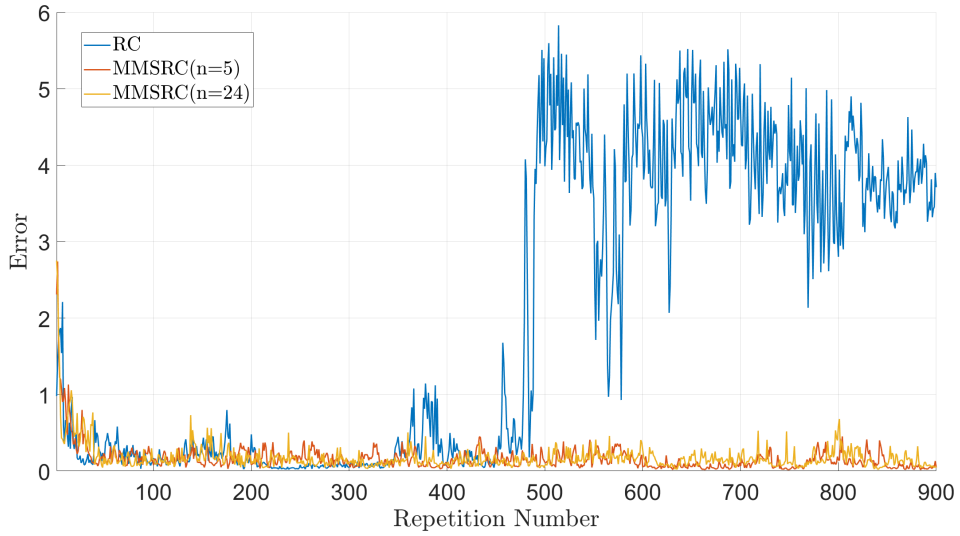

FIGURE 6.11: RC and MMSRC error norms plotted against the period number for the muscle fatigue test (Participant D).

As can be seen from the four figures, a similar trend is observed: Initially, both RC and MMSRC demonstrate comparable suppression effects. However, as the wrist dynamics change due to muscle fatigue, the performance of conventional RC declines, while MMSRC maintains a consistently high level.

In the **misaligned electrodes tests**, standard RC fails completely. However MMSRC5 still maintains the same performance as in the previous tests. The MMSRC24 results are even better, showing a 1.4% performance improvement over those of MMSRC5. The high performance of MMSRC is notable, since the candidate model sets were

not constructed using an uncertainty set which explicitly incorporated variation due to electrode misalignment. This shows that the variation due to fatigue used to construct $\mathcal{U}$ is sufficient to account for misalignment also. Here the MMSRC design procedure is also a critical factor, since a robust design increases the robust stability margin and allows a larger uncertainty space to be stabilised than the original $\mathcal{U}$.

In the **misaligned electrodes tests**, the error norms for each period obtained using conventional RC and MMSRC for the four participants are shown in Figure 6.12, Figure 6.13, Figure 6.14 and Figure 6.15.

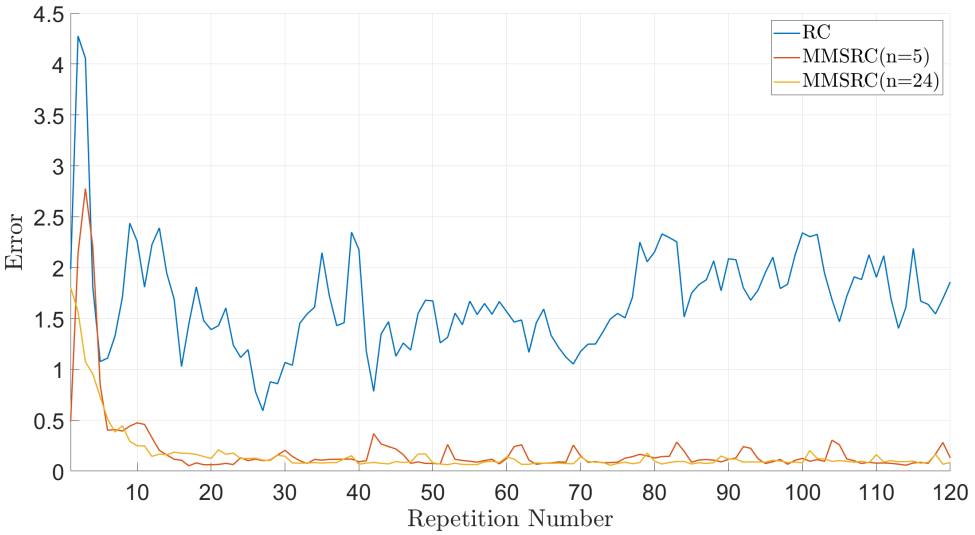

FIGURE 6.12: RC and MMSRC error norms plotted against the period number for the electrode misalignment test (Participant A).

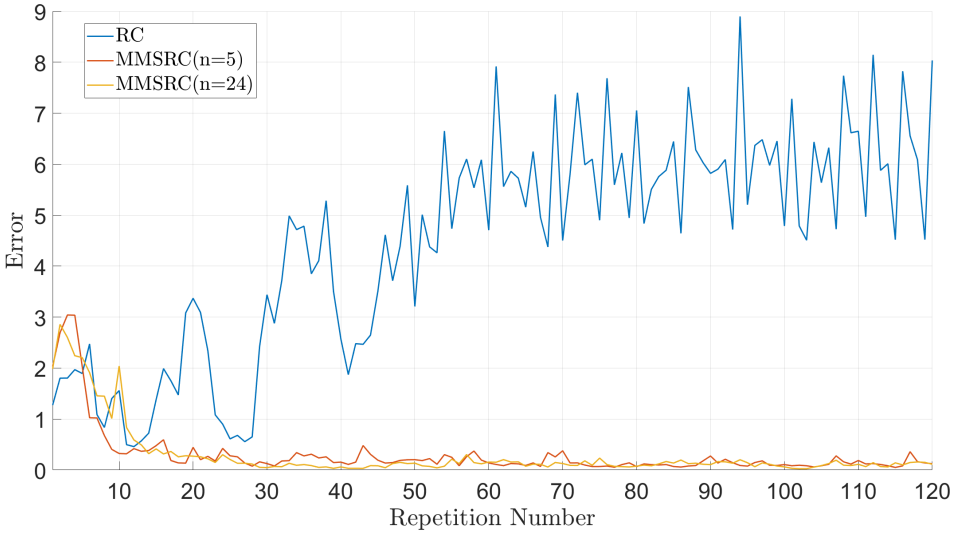

FIGURE 6.13: RC and MMSRC error norms plotted against the period number for the electrode misalignment test (Participant B).

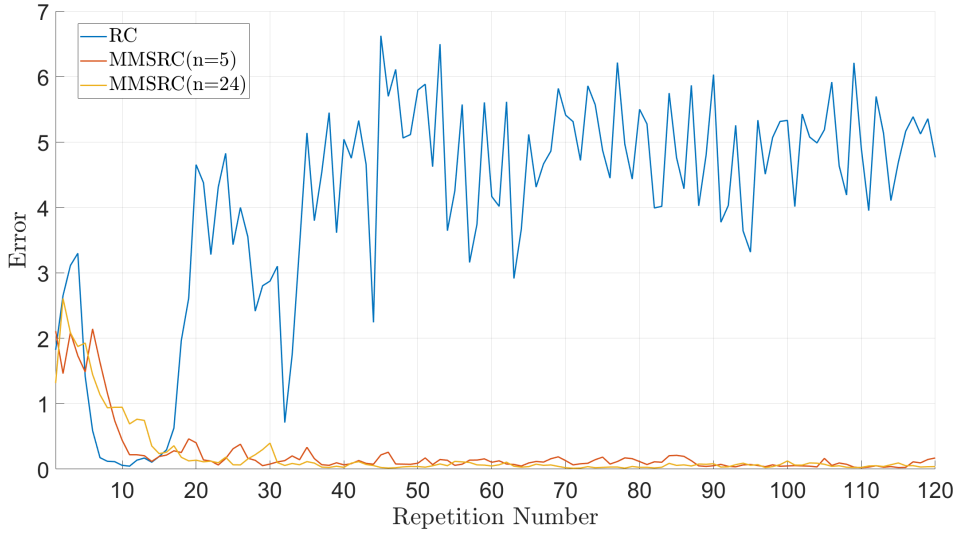

FIGURE 6.14: RC and MMSRC error norms plotted against the period number for the electrode misalignment test (Participant C).

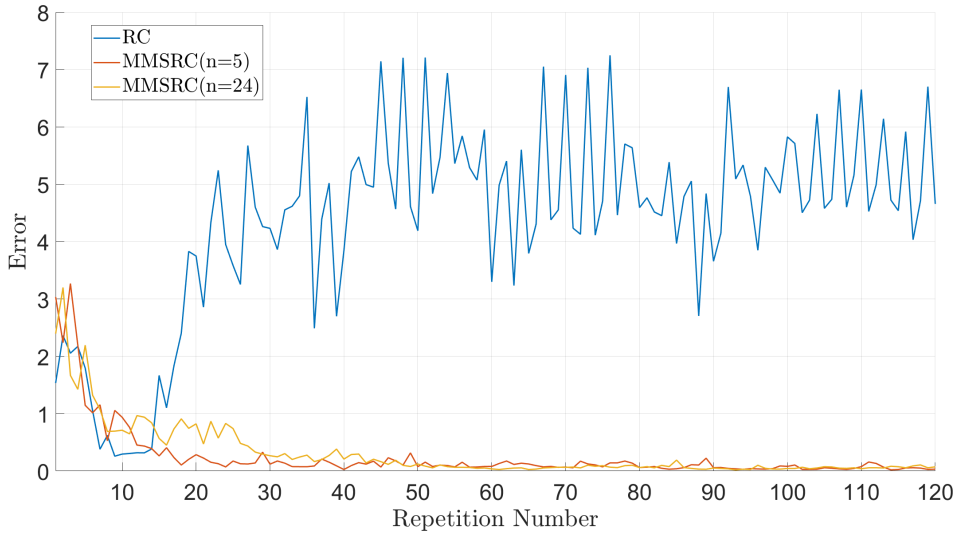

FIGURE 6.15: RC and MMSRC error norms plotted against the period number for the electrode misalignment test (Participant D).

The sharp increases in the RC error curves across the four figures above all demonstrate its sensitivity to model variations caused by electrode position changes. In contrast, MMSRC consistently maintains low error levels, exhibiting robustness against electrode position shifts.

The low performance indices of RC in both the muscle fatigue test and the misaligned electrodes test indicate that RC relies on high precision modelling and lacks robustness to model variation. However, MMSRC still maintains performance close to that under ideal conditions. In most cases, MMSRC24 outperforms MMSRC5 and has higher average

performance indices for all test scenarios. This means that increasing the number of candidate models is likely to further increase performance.

6.5.2 Switching of MMSRC

As mentioned in Section 4.3.3, when a new controller is switched into closed loop at the beginning of a new period, its computed control output utilizes the stored error and the state of the previous controller. Consequently, during the switching process, the internal state remains continuous without jumps. This smooth switching process achieves a bumpless controller transition by eliminating discontinuous state jumps, thereby preventing discomforting sudden changes in the participant's control signal. Throughout the experimental trials, all four participants reported no noticeable additional discomfort during control mode transitions.

Figure 6.16 and Figure 6.17 provide an example of smooth switching in MMSRC. Figure 6.16 shows the switching signal for MMSRC24 during the misaligned electrode test for Participant A. During the first few cycles, the switch varies but settles down to mainly point to model 16. This reflects the success of the MMSRC in dynamically adapting to change.

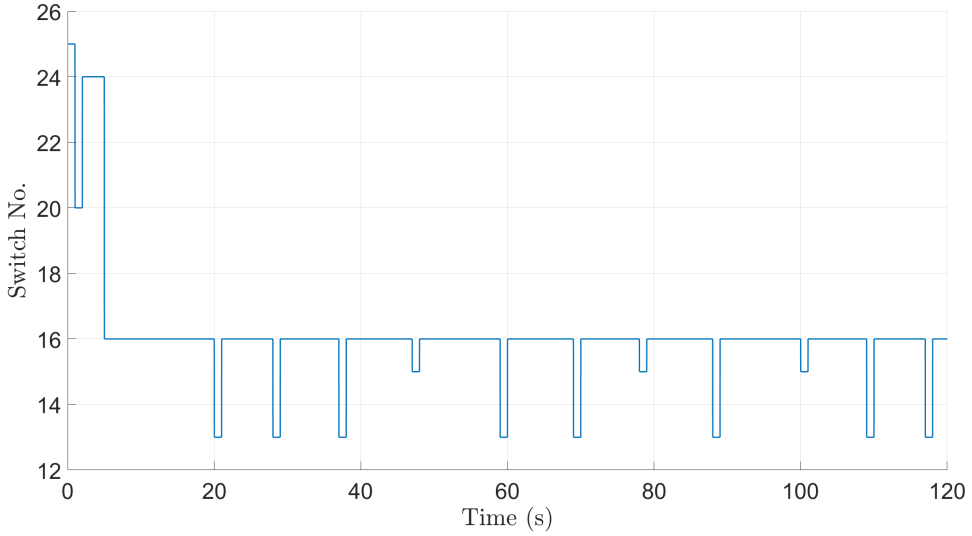

FIGURE 6.16: Switching signal $i_c(k)$ for MMSRC24 plotted against the period number for the misaligned electrodes test (Participant A).

Figure 6.17 displays the control signal during the 4-6s switch transition in Figure 6.16. The switching is smooth due to the absence of abrupt changes in the controller's internal state.

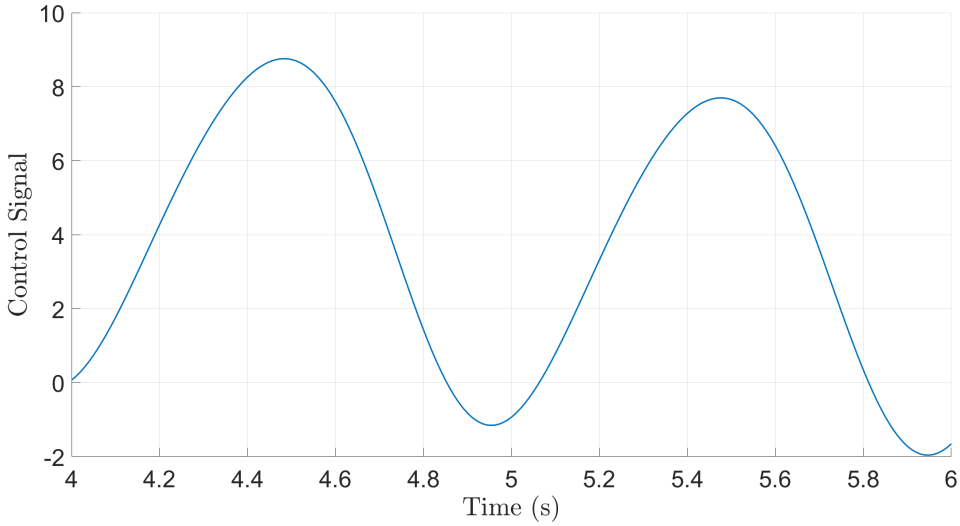

FIGURE 6.17: Control signal $u_w(k)$ during switch transition for MMSRC24 plotted against time for the misaligned electrodes test (Participant A).

6.5.3 Energy Consumption

The amount of FES required to suppress tremor is an important metric as wearable devices will ultimately be used over many hours or even days. This has been quantified by integrating the square of the electrical stimulation signal over time, i.e.

$$\text{control energy} = T_s \sum_{k=0}^{N} \left\{ u_{fcr}(k)^2 + u_{ecr}(k)^2 \right\} \tag{6.10}$$

where T_s is the sampling interval. The computation again excludes the initial 30 seconds to remove transients. The control energy is shown in Table 6.3 for all controllers and test scenarios. The 'Average' row represents the mean energy of the same controller across experiments involving all four participants. The data have been converted into a more intuitive percentage-based representation. Each test scenario uses the best (i.e. lowest) mean value (highlighted in green) as the 100% baseline:

- Ideal Conditions Test: RC (13.99 $\times 10^5$)
- Muscle Fatigue Test: MMSRC5 (159.72 $\times 10^5$)
- Misaligned Electrodes Test: MMSRC24 (15.25 $\times 10^5$)

Individual cell values are converted to percentages by dividing them by their respective baseline and multiplying by 100, then rounded to the nearest integer. The optimal controller's average (green) remains at 100% for comparison across scenarios.

TABLE 6.3: Steady control energy for different controllers in different test scenarios

Participants	Ideal Conditions Test			Muscle Fatigue Test			Misaligned Electrodes Test		
	RC	MMSRC5	MMSRC24	RC	MMSRC5	MMSRC24	RC	MMSRC5	MMSRC24
A	140%	147%	208%	307%	205%	335%	843%	270%	180%
B	69%	51%	94%	187%	74%	80%	378%	43%	61%
C	135%	118%	92%	109%	58%	115%	227%	59%	79%
D	56%	92%	124%	105%	64%	82%	222%	57%	80%
Average	100%	102%	130%	177%	100%	153%	417%	107%	100%

In the **ideal conditions test**, all controllers use a low level of energy. MMSRC uses slightly more that the others in some cases as it initially uses a controller which uses excessive control action.

In the **ideal conditions tests**, the norm of the control energy for each period obtained using conventional RC and MMSRC for the four participants are shown in Figure 6.18, Figure 6.19, Figure 6.20 and Figure 6.21.

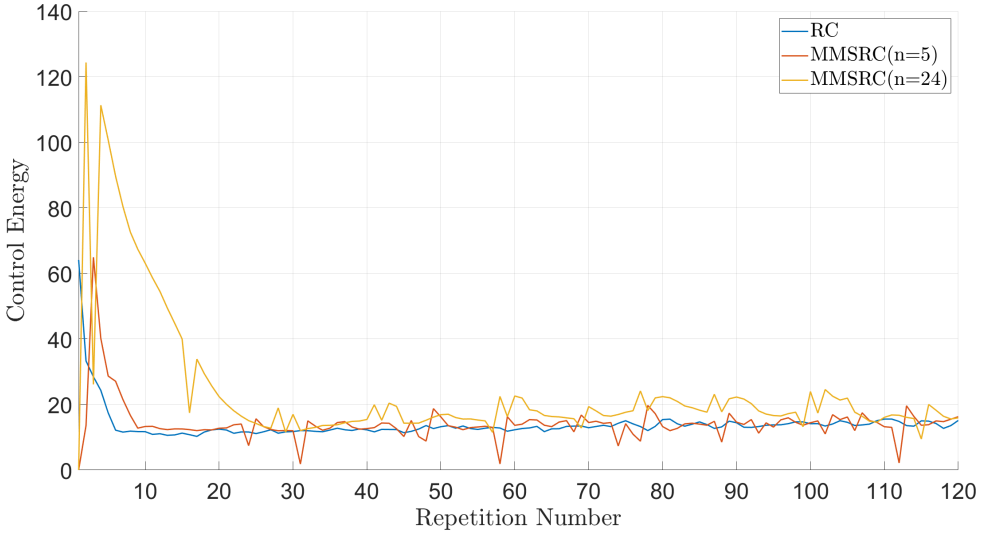

FIGURE 6.18: RC and MMSRC energy norms plotted against the period number for the ideal conditions test (Participant A).

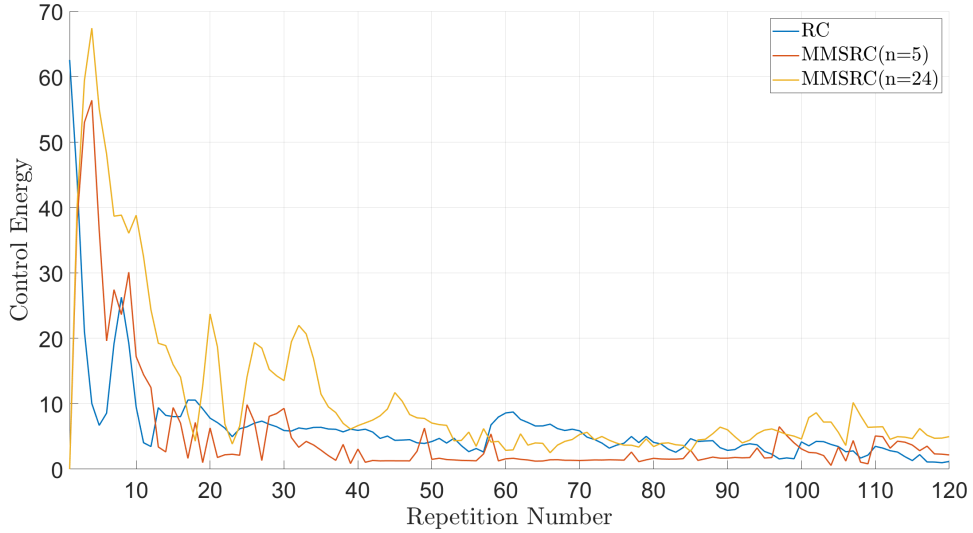

FIGURE 6.19: RC and MMSRC energy norms plotted against the period number for the ideal conditions test (Participant B).

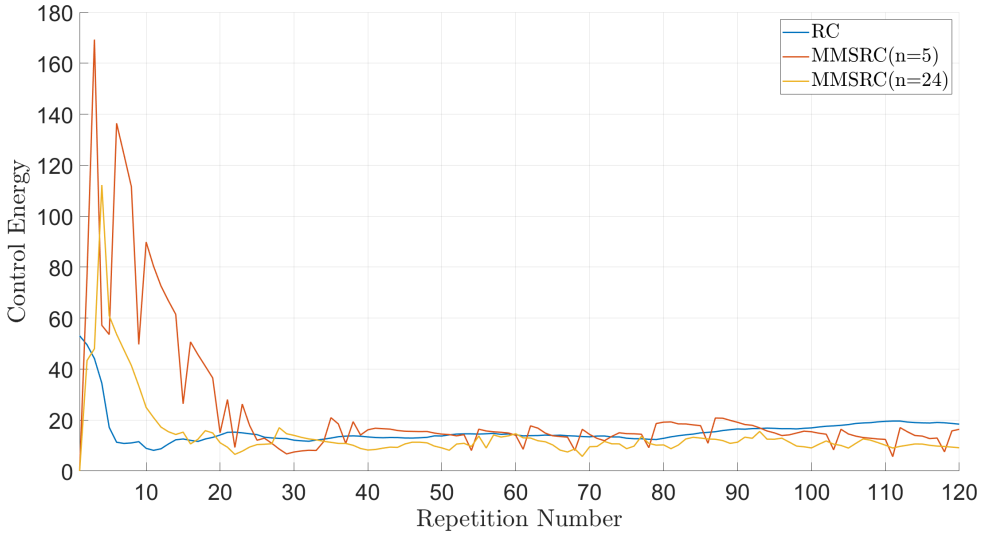

FIGURE 6.20: RC and MMSRC energy norms plotted against the period number for the ideal conditions test (Participant C).

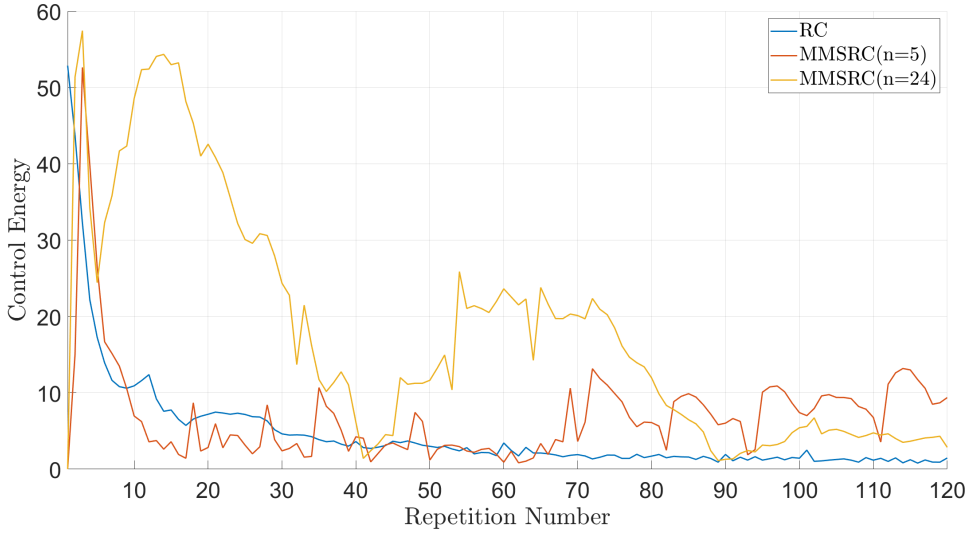

FIGURE 6.21: RC and MMSRC energy norms plotted against the period number for the ideal conditions test (Participant D).

As can be seen from the four figures above, although MMSRC consumes more energy in the initial phase of the ideal conditions test, there is no significant difference in energy consumption between RC and MMSRC after convergence, with the gap remaining within a small range.

In the **muscle fatigue test**, standard RC is unable to adapt to the changing dynamics, causing oscillation and over-correction. These larger control signals correspond to an energy consumption which gradually (or sometimes rapidly) increases as the test continues. Conversely, MMSRC5 and MMSRC24 adapt to the changing dynamics and preserve stability, requiring less control energy. These controllers still require more energy than the ideal conditions test, since fatigue reduces the effect of the FES, causing a larger signal to be required to produce a similar level of movement. Note that the fatigue test has 7.5 times longer duration than the ideal conditions test (and the energy computation period is 9.67 times longer), so the increase in control energy is 1016% for MMSRC5 and 1247% for MMSRC24.

In the **muscle fatigue tests**, the norm of the control energy for each period obtained using conventional RC and MMSRC for the four participants are shown in Figure 6.22, Figure 6.23, Figure 6.24 and Figure 6.25.

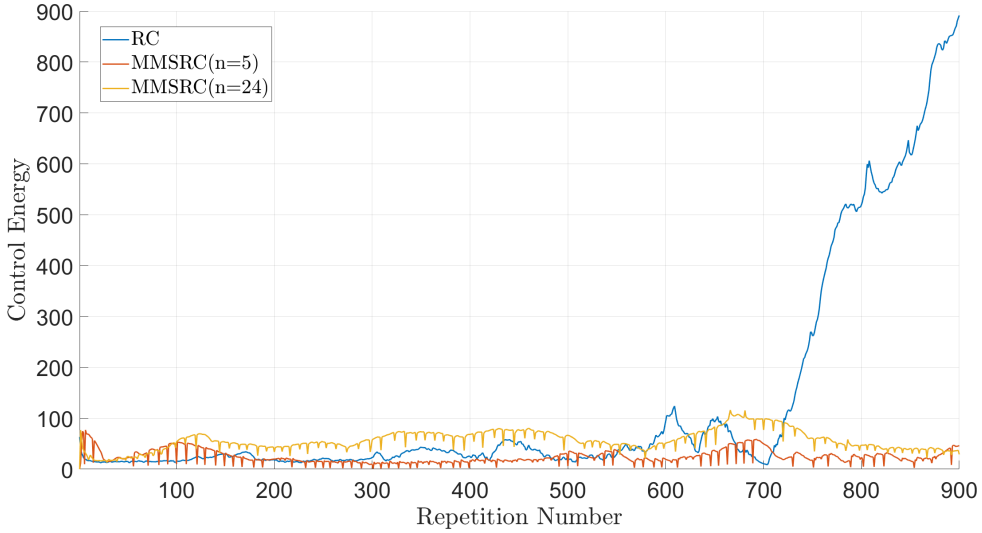

FIGURE 6.22: RC and MMSRC energy norms plotted against the period number for the muscle fatigue test (Participant A).

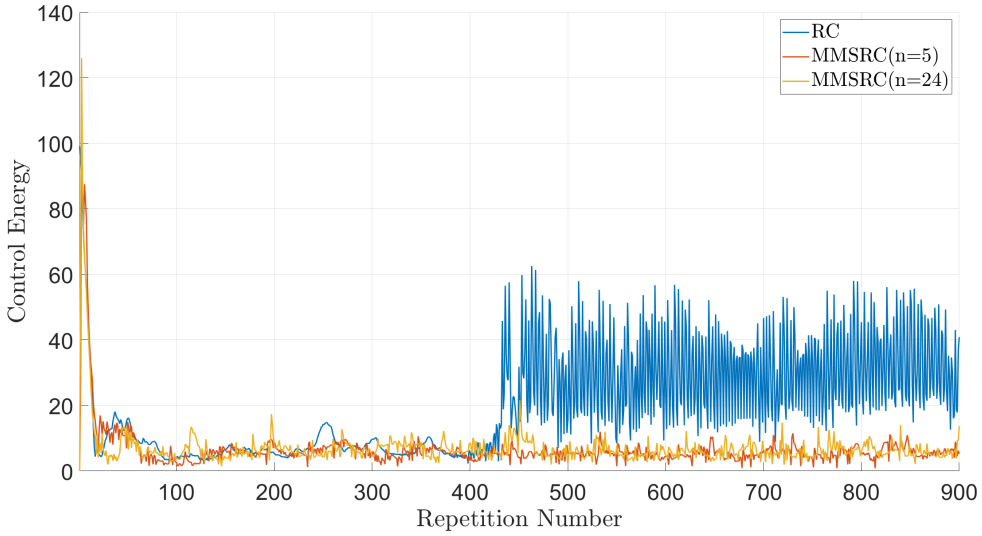

FIGURE 6.23: RC and MMSRC energy norms plotted against the period number for the muscle fatigue test (Participant B).

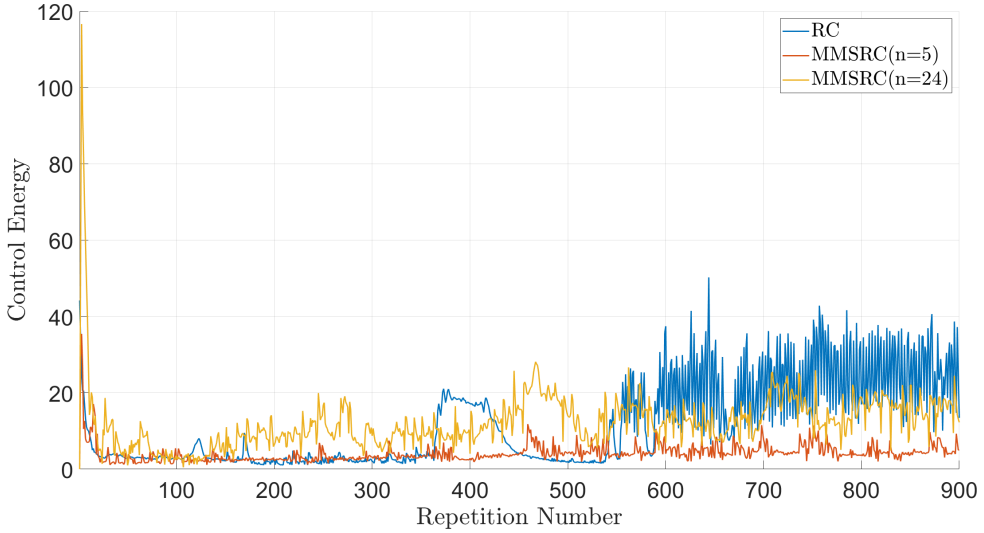

FIGURE 6.24: RC and MMSRC energy norms plotted against the period number for the muscle fatigue test (Participant C).

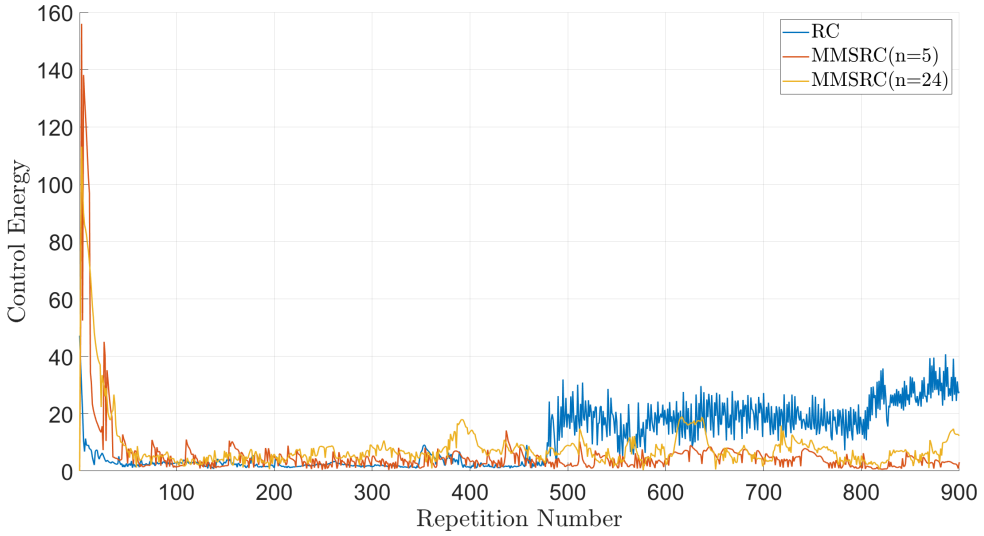

FIGURE 6.25: RC and MMSRC energy norms plotted against the period number for the muscle fatigue test (Participant D).

The above four figures demonstrate that when changes induced by muscle fatigue exceed the tolerable limit of RC, its energy consumption experiences a dramatic surge. In contrast, while still effectively suppressing tremors, MMSRC maintains a relatively low level of energy consumption.

In the **misaligned electrodes test**, standard RC again achieves very poor suppression accuracy, and the oscillatory and often unstable control action corresponds to excessive energy. MMSRC on the other hand maintains stability and both designs require similar

levels of control energy as they did in their ideal conditions tests. This clearly shows the importance of adapting the model in order to maintain efficiency and low energy.

In the **misaligned electrodes tests**, the norm of the control energy for each period obtained using conventional RC and MMSRC for the four participants are shown in Figure 6.26, Figure 6.27, Figure 6.28 and Figure 6.29.

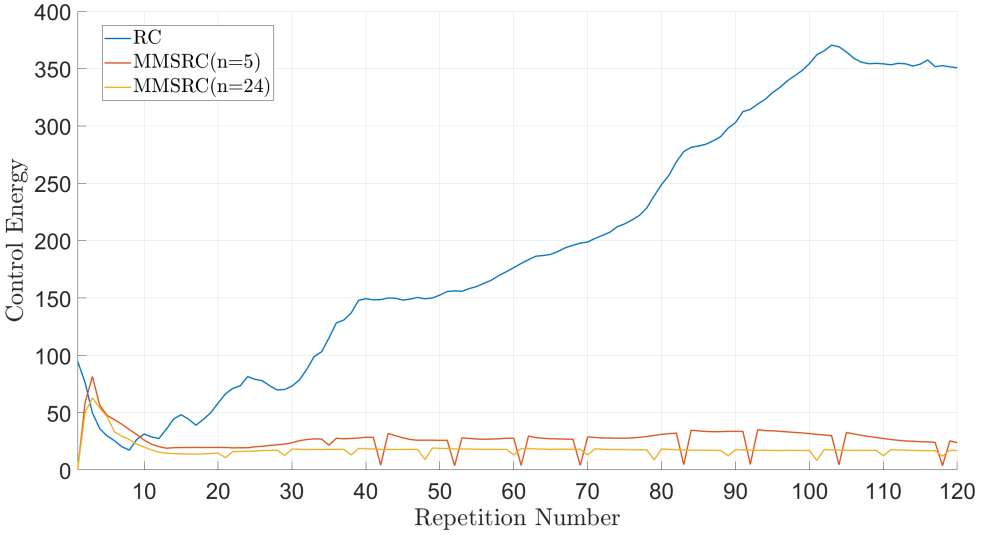

FIGURE 6.26: RC and MMSRC energy norms plotted against the period number for the electrode misalignment test (Participant A).

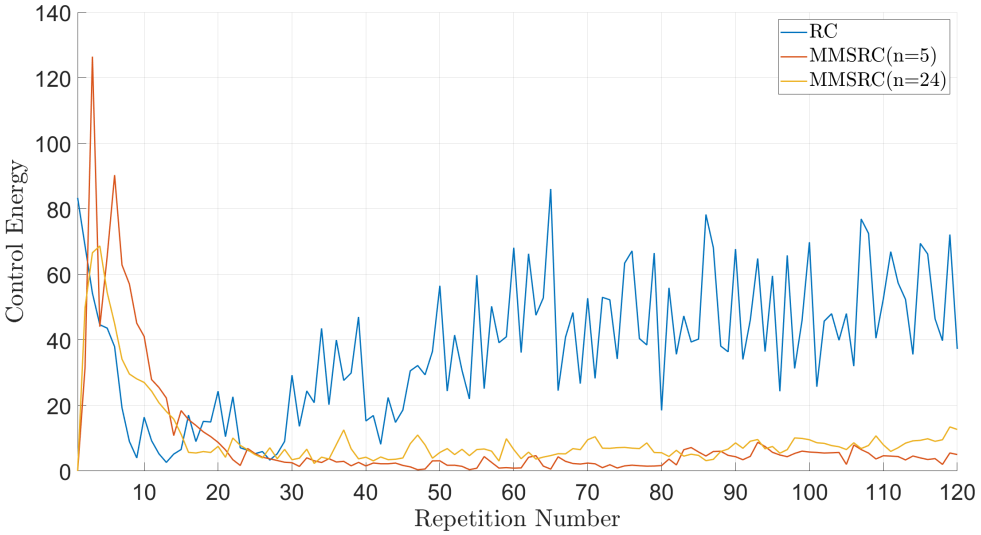

FIGURE 6.27: RC and MMSRC energy norms plotted against the period number for the electrode misalignment test (Participant B).

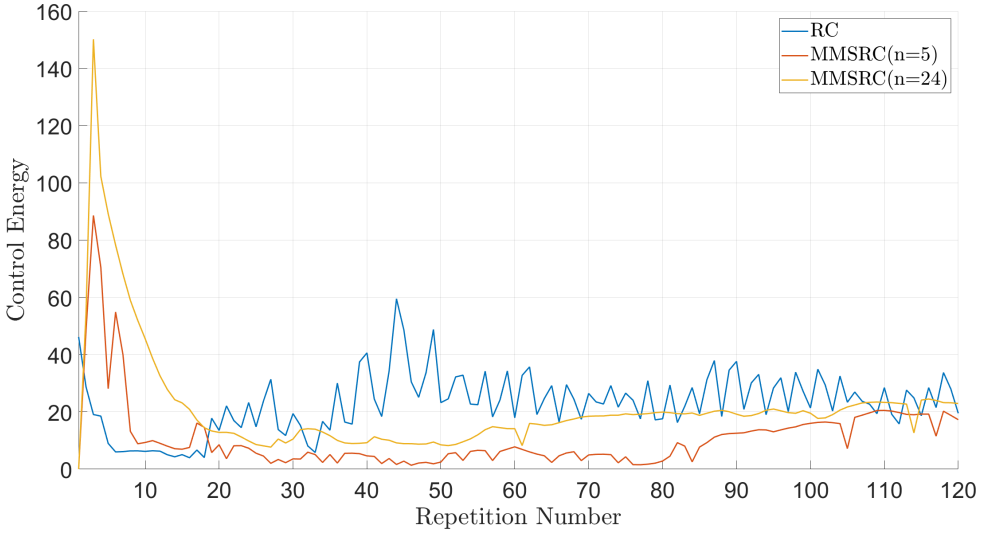

FIGURE 6.28: RC and MMSRC energy norms plotted against the period number for the electrode misalignment test (Participant C).

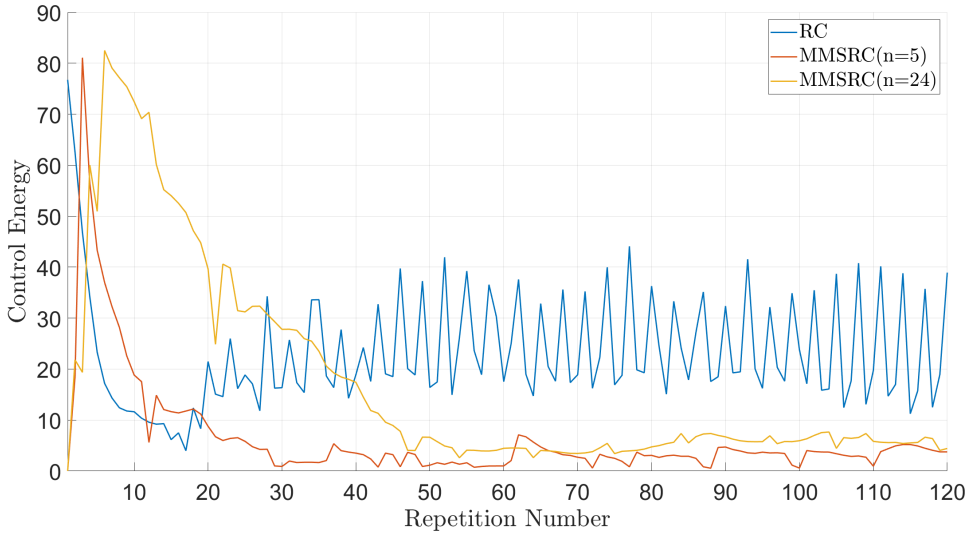

FIGURE 6.29: RC and MMSRC energy norms plotted against the period number for the electrode misalignment test (Participant D).

These figures further demonstrate that RC exhibits significantly higher energy consumption after electrode position shifts, while both MMSRC maintain lower energy usage with minimal difference between them.

6.5.4 Conclusions based on Quantitative Analyses and Further Discussion

The experimental results presented in this chapter demonstrated the superior robustness and adaptability of MMSRC compared to conventional RC, particularly under conditions of muscle fatigue and electrode misalignment. The test results confirmed that MMSRC maintained high performance when the system dynamics were unknown, changed rapidly, or slowly varied over time. These are all scenarios that would occur when FES is used in homes or clinics where frequent re-identification of a model is infeasible. On the other hand, standard RC performance decreased significantly. The improvement from RC to MMSRC5 was significant, while the improvement from MMSRC5 to MMSRC24 was small.

In terms of energy consumption, MMSRC5 had low energy consumption and high stability, which was suitable for most of the changing scenarios. For high-precision scenarios with complex system variations, MMSRC24 was superior, but the model complexity and energy consumption needed to be balanced. From the energy consumption point of view, more candidate models were not always better; MMSRC5 was sufficient for most scenarios, while more models in MMSRC24 introduced redundancy. This requires the designer to make a trade-off between performance and energy consumption.

However, several important observations and limitations warrant further discussion, as they have implications for the future exploitation and refinement of this approach:

- Choice of 1 Hz Tremor Frequency: The artificial tremor introduced in these experiments was set to a frequency of 1 Hz, which is characteristic of intention tremor. While this choice allowed for a controlled and repeatable experimental platform, it may not fully represent the broader spectrum of pathological tremors. The current MMSRC framework, though designed to handle uncertainty in plant dynamics, was not explicitly tested against higher frequency tremors. Future work should validate the approach across a wider frequency range to ensure generalizability. Furthermore, the use of a single-frequency tremor does not capture the multi-frequency components often present in pathological tremors. Extending MMSRC to handle multiple or time-varying frequencies would be a critical next step toward clinical applicability.
- Challenges with Voluntary Contractions: During testing, some participants (notably Participants D) exhibited difficulty in fully relaxing their wrist muscles, leading to unintended voluntary contractions. This was observed as irregular fluctuations in the control signal, particularly during the initial periods of the ideal conditions test. Such voluntary contractions introduce unmodeled dynamics that can degrade controller performance and complicate the estimation process. To mitigate this issue in future studies, researchers could incorporate EMG sensors to

monitor muscle activity and detect voluntary efforts. Alternatively, participants could undergo more extensive training to familiarize themselves with the requirement for relaxation. Another approach is to integrate voluntary motion estimation into the MMSRC framework to explicitly account for and decouple voluntary actions from tremor.

- Participant A's Results: A consistent trend observed across all test scenarios was that Participant A exhibited less distinct performance differences between RC and MMSRC controllers. For instance, in the misaligned electrodes test, the performance indices for RC, MMSRC5, and MMSRC24 were 0.4807, 0.9562 and 0.9701, respectively—a narrower margin compared to other participants. This may be attributed to Participant A's wrist dynamics aligning more closely with the nominal model, thereby reducing the relative advantage of MMSRC. Additionally, the model parameters for Participant A might fall within a region of the uncertainty space where even conventional RC can provide adequate coverage and moderate stability. Alternatively, Participant A may exhibit lower resistance to FES, with more relaxed muscles and no voluntary opposition. This highlights the individual variability in responses to FES, underscoring an important fact: different individuals react differently to FES therapy. Consequently, when designing MMSRC, it is crucial to develop personalized model sets tailored to each individual. Future systems capable of creating customized solutions for each person would ensure optimal therapeutic outcomes across diverse individuals.

6.6 Summary

This chapter systematically introduced the parameters and steps required for identifying the wrist model, as well as the process of establishing the uncertainty space. The estimator was extended to handle uncertain tremor. The specific experimental system for tremor suppression and the steps for testing different controllers were described.

Although the system was extended to a Hammerstein structure, the experimental results still validated the conclusions from the simulations of the linear system in Chapter 3: MMSRC was more robust to uncertainty than RC, and increasing the number of candidate models helped further enhance robustness. However, this enhancement was minimal in practical experiments. In contrast, regarding energy consumption, MMSRC with fewer candidate models consumed less energy while maintaining high performance. This provided guidance for other research in balancing performance and energy consumption. For application scenarios requiring higher precision and having lower energy constraints, the number of candidate models can be increased. Conversely, for scenarios with high energy constraints but demanding performance requirements, MMSRC with fewer candidate models can be selected.

While MMSRC demonstrated remarkable robustness to modeled uncertainty, it is important to note that the candidate model sets were constructed based on a limited number of identification trials. In real-world scenarios, the uncertainty space may be larger and more complex. Moreover, the computational burden of MMSRC may pose challenges for embedded implementation in wearable devices. Future research should explore model reduction techniques and optimized switching strategies to balance performance and computational efficiency. Finally, the use of healthy participants and artificially induced tremor, while necessary for controlled validation, limits the direct translation of these findings to pathological populations. Testing with individuals with neurological disorders is essential to confirm the clinical efficacy of MMSRC.

Chapter 7

Conclusions and Future Work

7.1 Conclusions

There is extensive evidence that tremor can seriously interfere with an individual's activities of daily life. However, the range of current medical treatments available to sufferers does not provide satisfactory suppression. FES has proved to be a promising technology, but has not met its potential due to the competing requirements of high accuracy, complex time-varying system dynamics and the need for rapid set-up procedures. In Chapter 2 it was shown that RC is the leading control approach and has the potential to completely suppress tremors, however current RC implementations required time-consuming tests to identify a precise model, dependence on high precision modeling, and lack of adaptability to tremor frequency variations. Resolving these issues would mean effective FES based tremor suppression could be successfully applied in the settings where it is most needed: e.g. the user's own home or workplace.

The primary objective of this programme of research was therefore to design a new controller—MMSRC—to address the limitations of previous RC-based tremor suppression approaches. The first step was to further analyse the fundamental structure and principles of RC in Chapter 2. To quantitatively describe the current RC system's tolerance to model uncertainty, a robust stability margin was derived. In Chapter 3, robust theory based on this was used to develop design procedures for different RC structures. The design procedures allow designers to tune parameters themselves to make a trade-off between system robustness and convergence speed. These procedures were applied to suppress tremor in an idealized wrist model. The results demonstrated that RC is sensitive to parameter variations in the model, lacking robustness. Moreover, RC cannot adapt to changes in tremor frequency and can only suppress tremor at a single frequency.

Having understood the precise failings to current RC designs, the structure and theory of MMSRC were introduced in Chapter 4. Its theoretical and practical design procedures were described in detail, with the latter applied in simulations. The results were

compared with the RC tremor suppression results from Chapter 3, demonstrating that MMSRC is more robust to model parameter variations than standard RC. Furthermore, increasing the number of candidate models in MMSRC can further cover the model uncertainty space, thereby enhancing the robustness of MMSRC.

However, the assumption of a linear model form was somewhat idealised. Therefore, in Chapter 5, the linear wrist model was extended into a Hammerstein structure. For models containing nonlinear parts, RC and robustness theories were expanded to include the nonlinear components. Based on this, MMSRC was also extended to a Hammerstein structure, and a theoretical design procedure was developed. Such an extension not only addressed nonlinearity in the wrist, but also enables MMSRC to be applied to more application scenarios in other research contexts.

The Hammerstein structure in Chapter 5 laid the foundation for the experiments in Chapter 6. First, the form and identification of model parameters in the Hammerstein wrist model were defined, and the process of establishing the model uncertainty space was detailed. Then, the MMSRC estimator was extended to address unknown and/or varying tremor. Following a detailed explanation of the experimental system and procedures, experiments were conducted using RC, MMSRC with 5 candidate models, and MMSRC with 24 candidate models. The experimental results validated the conclusions from Chapter 4: under dynamic model changes caused by muscle fatigue and electrode misplacement, MMSRC demonstrated superior and more stable performance compared to RC. Although robustness to model uncertainty can be enhanced by increasing the number of candidate models, this enhancement was less pronounced than in the simulation results of Chapter 4, due to computational load and the fact that MMSRC with fewer candidate models already exhibited good performance. Additionally, the experiments evaluated the energy consumption of the three controllers. In most tests, MMSRC with fewer models consumed less control energy. This provides designers with a design principle: For scenarios demanding high precision with low energy constraints, the number of candidate models should be increased. For scenarios requiring a balance between performance and energy consumption, MMSRC with a relatively small number of candidate models should be selected.

In summary, the main objectives of this research has been achieved. The newly designed MMSRC has overcome the major limitations of previous RC approaches. For limitations not yet fully overcome, MMSRC also demonstrates the potential to address them. Its main breakthroughs are as follows:

1) Elimination of time-consuming model identification: The time-consuming process of model identification and dynamic range confirmation needs to be performed only once per individual. In the misaligned electrodes test described in Chapter 6, both MMSRC variants demonstrated superior tremor suppression performance without

re-identifying the model. This demonstrates that in future clinical or home applications, if the electrodes are placed inconsistently or repositioned, MMSRC can still deliver high-performance suppression without requiring model re-identification. A future commercial system can therefore be used by the individual alone, rather than needing an engineer or training operator.

2) High tolerance for imprecise modeling and robustness to model uncertainty: During practical model identification, the obtained model inherently contains some degree of modeling error. Under these conditions, during the muscle fatigue test and misaligned electrodes tests, MMSRC exhibited superior performance and stability. Compared to the ideal scenario where the model remains unchanged, MMSRC did not show any of the significant performance degradation observed with RC, demonstrating its robustness to variation in model dynamics. Although tests for other potential causes of model parameter changes (e.g. spasticity) were lacking, MMSRC can still be expected to handle such scenarios. This is because the simulation results in Chapter 4 have already demonstrated that MMSRC can increase the number of candidate models, covering a broader uncertainty space. However, in practical applications, this operation might be constrained by computational load.

Furthermore, in addition to achieving its primary objectives, this study yielded the following outcomes:

1) A robust stability margin applicable to a general RC system was derived based on gap metric analysis, establishing a connection between gain stability and the standard stability condition of RC. When the RC system was extended to a Hammerstein structure, the summarized robust theory was also extended to include the nonlinear component. This provides a tool for quantitatively describing the degree of uncertainty the system can tolerate. Although the robust stability margin might be overly conservative, the design procedures developed based on this concept still provide a useful guide to maximize the system's robustness. Moreover, in practical applications, the robust stability margin can be replaced by the performance index, enabling a reasonable assessment of system robustness while reducing computational load.

2) Design procedures were developed for both the general structure of RC and an extended structure incorporating an additional feedback controller. Although both simulations and experiments demonstrated that RC lacks robustness against model uncertainty, these design procedures remain valuable. They provide designers with a design rationale, allowing parameter adjustment based on scenario-specific requirements for convergence rate and system robustness.

3) Theoretical design procedures were developed for linear MMSRC and Hammerstein MMSRC. Since the computational load of the performance index is less than that of the robust stability margin, the practical design procedure involves computing the performance index to select a suitable candidate model set. This offers designers a feasible design approach with low computational burden.

4) The control energy consumption of MMSRC was quantitatively analysed and compared. Combined with the results of the performance index used to evaluate its performance, the study provides designers with a rationale for controller selection: In ideal scenarios with infrequent model changes, choose RC to simplify design. In scenarios with requirements for both performance and energy consumption, choose MMSRC with a small number of candidate models to achieve high performance tracking or suppression tasks while reducing control energy consumption. When pursuing high precision control regardless of energy consumption, increase the number of candidate models in MMSRC to achieve high performance.

Translating the MMSRC architecture into a commercial device is likely to involve embedding it in some form of wearable. The above trade-offs are critical in this case, since wearable hardware (e.g. a ESP32 or nRF52 series microchip) contains very limited computational resources. In addition, battery power will also be a prime concern.

7.2 Future Work

Despite the promising results demonstrated in this thesis, several limitations present opportunities for future research. Addressing these limitations will be crucial for translating the MMSRC framework from a laboratory prototype to a clinically viable system.

7.2.1 Limitations of Current Testing Methods and Potential Solutions

The experimental validation in this work, while comprehensive, has inherent limitations that future researchers should consider:

- Limitations of artificial tremor in comparison to physiological tremor: The use of a motor-induced tremor in healthy participants, as employed in this study, provides a controlled and repeatable platform for initial validation. However, it cannot fully capture the complex, multi-frequency composition, spontaneous amplitude fluctuations, and intricate directional patterns characteristic of pathological tremors originating from neurological dysfunction (Bhatia et al., 2018; Elble, 2017). Future work should employ more sophisticated tremor simulators that can generate multi-joint, multi-frequency perturbations, or better yet, progress to testing with

individuals living with pathological tremor. The reliability and ecological validity of the findings would be significantly enhanced by such a progression.

- Lack of study on interference with voluntary motion: In real world problem, the system must suppress tremor without impeding intentional voluntary movement. In particular, the impact of MMSRC on voluntary movement interference is currently inconclusive. Future work must formally design and implement experiments where participants perform tracking tasks (e.g., following a moving target on a screen) while the controller simultaneously suppresses tremor. This will quantitatively evaluate the trade-off between suppression performance and voluntary motion preservation.

- Limitations of the uncertainty space: The uncertainty set $\mathcal{U}$ was constructed primarily from variations induced by muscle fatigue. While it serendipitously covered the effects of electrode misalignment, it may not encompass all potential sources of uncertainty in a home-based setting, such as significant changes in skin or extreme spasticity. Future researchers could adopt more extensive system identification campaigns, collecting data across a wider range of physiological states and electrode placements to construct a more comprehensive and robust uncertainty set.

7.2.2 Transition to Testing People with Tremor

A critical issue for future research is determining the appropriate stage for testing algorithms such as MMSRC on people living with tremor. This transition process may be divided into the following three steps:

- Testing on a broader population of unimpaired participants: Extensive testing on healthy participants with artificially induced tremor, as conducted in this thesis, is a necessary and ethically responsible first step. It allows for rapid prototyping, initial robustness checks, and the refinement of experimental protocols without imposing undue burden on clinical populations. The algorithm should demonstrate consistent performance and safety across a diverse group of healthy participants under various perturbed conditions before proceeding to patient testing.

- Preliminary testing of a patient population with tremors: The transition to clinical testing should be conducted in phases. An initial feasibility study with a small cohort (e.g., 3-5 patients) can confirm the basic functionality and safety of MMSRC within the intended patient population. This should be carried out in a laboratory setting. Statistical validation should be used to verify performance advantages over conventional methods. Early engagement with patients is essential. Their feedback is invaluable for refining performance metrics and ensuring the usability of the device.

- Application in clinical and home settings: If the evaluation of preliminary patient testing demonstrates success, it would justify conducting a larger scale clinical study. Ultimately, home trials should be carried out to assess long term usability and effectiveness in daily life.

In conclusion, while this thesis has established MMSRC as a robust framework for FES-based tremor suppression, its full potential can only be realized through continued research that addresses these limitations and successfully navigates the path to clinical validation.

References

Bain, P. G. (2002). The management of tremor. *Journal of Neurology, Neurosurgery & Psychiatry*, 72(suppl 1):i3–i9.

Benabid, A., Pollak, P., and Louveau, A. (1987). Combined (thalamotomy and stimulation) stereotactic surgery of the vim thalamic nucleus for bilateral parkinson disease. *Stereotactic and Functional Neurosurgery*, 50(1-6):344–346.

Bhatia, K. P., Bain, P., and Bajaj, N. (2018). Consensus statement on the classification of tremors. from the task force on tremor of the international parkinson and movement disorder society. *Movement Disorders*, 33(1):75–87.

Bradley, R. S. (2010). *The robust stability of iterative learning control*. PhD thesis, University of Southampton.

Brend, O. (2014). *Implementation and experimental evaluation of multiple model switched adaptive control for FES-based rehabilitation*. PhD thesis, University of Southampton.

Buchstaller, D. and French, M. (2016). Robust stability for multiple model adaptive control: Part ii—gain bounds. *IEEE Transactions on Automatic Control*, 61(3):693–708.

Cha, Y. and Arami, A. (2020). Quantitative modeling of spasticity for clinical assessment, treatment and rehabilitation. *Sensors*, 20(18):5046.

Chen, Q., Yu, X., Sun, M., Wu, C., and Fu, Z. (2021). Adaptive repetitive learning control of pmsm servo systems with bounded nonparametric uncertainties: Theory and experiments. *IEEE Transactions on Industrial Electronics*, 68(9):8626–8635.

Copur, E. H. (2017). *Repetitive control for FES-based tremor suppression*. Doctoral thesis, University of Southampton.

Copur, E. H., Freeman, C. T., Chu, B., and Laila, D. S. (2019). Repetitive control of electrical stimulation for tremor suppression. *IEEE Transactions on Control Systems Technology*, 27(2):540–552.

Deuschl, G., Bain, P., and Brin, M. (1998). Consensus statement of the movement disorder society on tremor. *Movement disorders: official journal of the Movement Disorder Society*, 13 Suppl 3:2–23.

Dey, N., Mondal, U., and Sengupta, A. (2020). Robust higher order repetitive controller for disturbance rejection and multiplicative uncertainty. In *2020 2nd International Conference on Innovative Mechanisms for Industry Applications (ICIMIA)*, pages 608–613.

Dirkx, M. F. and Bologna, M. (2022). The pathophysiology of parkinson's disease tremor. *Journal of the Neurological Sciences*, 435:120196. Special issue on Tremors.

Elble, R. (2017). Tremor. In *Neuro-Geriatrics*, pages 311–326. Springer.

Fang, T. and Freeman, C. T. (2023). Multiple model switched repetitive control with application to tremor suppression. In *2023 American Control Conference (ACC)*, pages 3859–3864.

Fang, T. and Freeman, C. T. (2025). Multiple model switched repetitive control for tremor suppression. *Mechatronics*, 110:103392.

Fekri, S., Athans, M., and Pascoal, A. (2004a). Rmmac: a novel robust adaptive control scheme. part i. architecture. In *2004 43rd IEEE Conference on Decision and Control (CDC) (IEEE Cat. No.04CH37601)*, volume 2, pages 1134–1139 Vol.2.

Fekri, S., Athans, M., and Pascoal, A. (2004b). Rmmac: a novel robust adaptive control scheme. part ii. performance evaluation. In *2004 43rd IEEE Conference on Decision and Control (CDC) (IEEE Cat. No.04CH37601)*, volume 2, pages 1140–1145 Vol.2.

Feys, P., Duportail, M., Kos, D., Ilsbroukx, S., Lamers, I., Asch, P. V., Helsen, W., and Moumdjian, L. (2023). Effects of peripheral cooling on upper limb tremor severity and functional capacity in persons with ms. *Journal of Clinical Medicine*, 12(13):4549.

Feys, P., Helsen, W., Liu, X., Mooren, D., Albrecht, H., Nuttin, B., and Ketelaer, P. (2005). Effects of peripheral cooling on intention tremor in multiple sclerosis. *Journal of Neurology, Neurosurgery & Psychiatry*, 76(3):373–379.

Freeman, C. (2017). Multiple model switched repetitive control. In *2017 IEEE 56th Annual Conference on Decision and Control (CDC)*, pages 4801–4806.

Freeman, C., Sampson, P., Burridge, J., and Hughes, A. M. (2015). Repetitive control of functional electrical stimulation for induced tremor suppression. *Mechatronics*, 32:79–87.

Freeman, C. T., Hughes, A.-M., Burridge, J. H., Chappell, P. H., Lewin, P. L., and Rogers, E. (2009). A Model of the Upper Extremity Using FES for Stroke Rehabilitation. *Journal of Biomechanical Engineering*, 131(3):031011.

Freeman, C. T., Lewin, P. L., Rogers, E., Owens, D. H., and HÄtÖnen, J. (2008). An optimality-based repetitive control algorithm for discrete-time systems. *IEEE Transactions on Circuits and Systems I: Regular Papers*, 55(1):412–423.

Frei, K. and Truong, D. D. (2022). Medications used to treat tremors. *Journal of the Neurological Sciences*, 435:120194. Special issue on Tremors.

Gao, D., Zhou, L., Pan, C., and Liao, C. (2021). Generalized-reduced-order-extended-state-observer-based adaptive repetitive control for brushless dc motor. In *2021 IEEE 10th Data Driven Control and Learning Systems Conference (DDCLS)*, pages 1528–1533.

Garcia-Higuera, J. A., Paredes-Acuña, N., Le, T., Auclair, B., Tomašković, K., Berberich, N., and Cheng, G. (2023). Damping tens-induced essential tremor symptoms in activities of daily living using the tumove wrist exoskeleton. In *2023 International Conference on Rehabilitation Robotics (ICORR)*, pages 1–6.

Geigel, N. and Gunduz, A. (2024). Performance of closed-loop dbs during sleep in patients with essential tremor. In *2024 46th Annual International Conference of the IEEE Engineering in Medicine and Biology Society (EMBC)*, pages 1–4.

Georgiou, T. and Smith, M. (1990). Optimal robustness in the gap metric. *IEEE Transactions on Automatic Control*, 35(6):673–686.

Georgiou, T. and Smith, M. (1997). Robustness analysis of nonlinear feedback systems: an input-output approach. *IEEE Transactions on Automatic Control*, 42(9):1200–1221.

Ghimire, S., Thapa, B., Neupane, D., and Pokharel, P. (2024). Outcomes of stereotactic thalamotomy in patients of essential tremor: A systematic review. *Journal of Clinical Neuroscience*, 126:38–45.

Gironell, A., Sedano, B. P., Aracil, I., Marín-Lahoz, J., Pagonabarraga, J., and Kulisevsky, J. (2018). Tremor types in parkinson disease: A descriptive study using a new classification. *Parkinson's Disease*, 2018.

Gupta, H. V., Pahwa, R., Dowell, P., Khosla, S., and Lyons, K. E. (2021). Exploring essential tremor: Results from a large online survey. *Clin Park Relat Disord.*, 25(5):100101.

Hamid, S. and Hayek, R. (2008). Role of electrical stimulation for rehabilitation and regeneration after spinal cord injury: An overview. *European Spine Journal*, 17(9):1256–1269.

Handforth, A. (2009). Zonisamide for essential tremor: An evaluator-blinded study. *Movement Disorders*, 24(3):437–440.

He, S., Debarros, J., Khawaldeh, S., Pogosyan, A., Mostofi, A., Baig, F., Pereira, E., Brown, P., and Tan, H. (2020). Closed-loop dbs triggered by real-time movement and tremor decoding based on thalamic lfps for essential tremor. In *2020 42nd Annual International Conference of the IEEE Engineering in Medicine & Biology Society (EMBC)*, pages 3602–3605.

Hsu, S.-C. and Lin, C.-Y. (2013). Robust μ control and repetitive control for dynamic tracking control of a pneumatic actuating table. In *2013 IEEE International Conference on Mechatronics and Automation*, pages 312–317.

Huen, D., Liu, J., and Lo, B. (2016). An integrated wearable robot for tremor suppression with context aware sensing. In *2016 IEEE 13th International Conference on Wearable and Implantable Body Sensor Networks (BSN)*, pages 312–317.

Hätönen, J., Freeman, C., Owens, D., Lewin, P., and Rogers, E. (2006). A gradient-based repetitive control algorithm combining ilc and pole placement. *European Journal of Control*, 12(3):278–292.

Jankovic, J. (1995). Outcome after stereotactic thalamotomy for parkinsonian, essential, and other types of tremor. *Neurosurgery*, 37(4):680–686.

Ji, Z.-C., Zhu, R.-J., and Shen, Y.-X. (2005). Fuzzy multiple reference models adaptive control and simulation study. In *2005 International Conference on Machine Learning and Cybernetics*, volume 5, pages 2747–2752 Vol. 5.

Jiang, X., Li, L., and Yu, P. (2021). Robust design of uncertain repetitive control system. In *2021 40th Chinese Control Conference (CCC)*, pages 3864–3869.

Kim, J., Wichmann, T., Inan, O. T., and Deweerth, S. P. (2020). A wearable system for attenuating essential tremor based on peripheral nerve stimulation. *IEEE Journal of Translational Engineering in Health and Medicine*, 8:1–11.

Lainiotis, D. (1976a). Partitioning: A unifying framework for adaptive systems, i: Estimation. *Proceedings of the IEEE*, 64(8):1126–1143.

Lainiotis, D. (1976b). Partitioning: A unifying framework for adaptive systems, ii: Control. *Proceedings of the IEEE*, 64(8):1182–1198.

Le, F., Markovsky, I., Freeman, C. T., and Rogers, E. (2010). Identification of electrically stimulated muscle models of stroke patients. *Control Engineering Practice*, 18(4):396–407.

Longman, R. W. (2000). Iterative learning control and repetitive control for engineering practice. *International Journal of Control*, 73(10):930–954.

Longman, R. W. (2010). On the theory and design of linear repetitive control systems. *European Journal of Control*, 16(5):447–496.

Luo, Y., Gao, Y., Li, Q., and Zhao, J. (2018). Central pattern generator based band-limited multiple fourier linear combiner for tremor estimation in functional electrical stimulation system. In *2018 IEEE International Conference on Mechatronics and Automation (ICMA)*, pages 1299–1304.

Mehanna, R. and Jankovic, J. (2013). Movement disorders in multiple sclerosis and other demyelinating diseases. *Journal of the neurological sciences*, 328(1-2):1–8.

Morse, A. (1996). Supervisory control of families of linear set-point controllers - part i. exact matching. *IEEE Transactions on Automatic Control*, 41(10):1413–1431.

Morse, A. (1997). Supervisory control of families of linear set-point controllers. 2. robustness. *IEEE Transactions on Automatic Control*, 42(11):1500–1515.

Okelberry, T., Lyons, K. E., and Pahwa, R. (2024). Updates in essential tremor. *Parkinsonism & Related Disorders*, 122:106086.

Ondo, W., Jankovic, J., and Connor, G. (2006). Topiramate in essential tremor: A double-blind, placebo-controlled trial. *Neurology*, 66(5):672–677.

Padilha Lanari Bó, A., Azevedo-Coste, C., Poignet, P., Geny, C., and Fattal, C. (2011). On the use of fes to attenuate tremor by modulating joint impedance. In *2011 50th IEEE Conference on Decision and Control and European Control Conference*, pages 6498–6503.

Page, A. P. (2020). *Repetitive control and electrode array pattern selection for FES-based drop-foot assistance*. Doctoral thesis, University of Southampton.

Panomruttanarug, B. and Longman, R. W. (2004). Repetitive controller design using optimization in the frequency domain. *Collection of Technical Papers*, 3:1215–1236.

Pascual-Valdunciel, A., González-Sánchez, M., Muceli, S., Adán-Barrientos, B., Escobar-Segura, V., Pérez-Sánchez, J. R., Jung, M. K., Schneider, A., Hoffmann, K.-P., Moreno, J. C., Grandas, F., Farina, D., Pons, J. L., and Barroso, F. O. (2021). Intramuscular stimulation of muscle afferents attains prolonged tremor reduction in essential tremor patients. *IEEE Transactions on Biomedical Engineering*, 68(6):1768–1776.

Peaden, A. W. and Charles, S. K. (2014). Dynamics of wrist and forearm rotations. *Journal of Biomechanics*, 47(11):2779–2785.

Peckham, P. H. and Knutson, J. S. (2005). Functional electrical stimulation for neuromuscular applications. *Annual Review of Biomedical Engineering*, 7:327–360.

Peng, S., Liu, P., Wang, X., and Li, K. (2025). Global, regional and national burden of parkinson's disease in people over 55 years of age: a systematic analysis of the global burden of disease study, 1991–2021. *BMC Neurol*, 17:178.

Pipeleers, G., Demeulenaere, B., and Sewers, S. (2008). Robust high order repetitive control: Optimal performance trade offs. *Automatica*, 44:2628–2634.

Pipeleers, G. and Moore, K. L. (2014). Unified analysis of iterative learning and repetitive controllers in trial domain. *IEEE Transactions on Automatic Control*, 59(4):953–965.

Prochazka, A., Elek, J., and Javidan, M. (1992a). Attenuation of pathological tremors by functional electrical stimulation i: Method. *Annals of biomedical engineering*, 20(2):205–224.

Prochazka, A., Elek, J., and Javidan, M. (1992b). Attenuation of pathological tremors by functional electrical stimulation ii: Clinical evaluation. *Annals of biomedical engineering*, 20(2):225–236.

Saridis, G. and Dao, T. (1972). A learning approach to the parameter-adaptive self-organizing control problem. *Automatica*, 8(5):589–597.

Songjun, M. (2014). Polynomial model of the inverse plant ilc algorithm. In *2014 International Conference on Information Science Applications (ICISA)*, pages 1–4.

Steinbuch, M., Weiland, S., and Singh, T. (2007). Design of noise and period-time robust high order repetitive control, with application to optical storage. *Automatica*, 43:2086–2095.

Sun, X., Huang, L., and Pan, Y. (2020). Bilateral posterior subthalamic area deep brain stimulation for essential tremor: A case series. *Frontiers in Human Neuroscience*, 14:16.

Turk, R., Notley, S. V., Pickering, R. M., Simpson, D. M., Wright, P. A., and Burridge, J. H. (2008). Reliability and sensitivity of a wrist rig to measure motor control and spasticity in post-stroke hemiplegia. *Neurorehabilitation and Neural Repair*, 22(6):684–696.

Vatanpour, M., Tahami, E., Majdi, H., and Namdari, H. (2015). Pathological tremor suppression in elbow joint using anfis-based functional electrical stimulation. In *2015 International Congress on Technology, Communication and Knowledge (ICTCK)*, pages 281–286.

Verstappen, R. J. L. M., Freeman, C. T., Rogers, E., Sampson, T., and Burridge, J. H. (2012). Robust higher order repetitive control applied to human tremor suppression. In *2012 IEEE International Symposium on Intelligent Control*, pages 1214–1219.

Wagle Shukla, A. and Okun, M. S. (2014). Surgical treatment of parkinson's disease: patients, targets, devices, and approaches. *Neurotherapeutics: the journal of the American Society for Experimental NeuroTherapeutics*, 11(1):47–59.

Wang, L.-y., Wang, W.-f., Hui, S.-y., Yang, L., Liu, Y.-x., and Li, H.-j. (2025). Emerging epidemiological trends of multiple sclerosis among adults aged 20-54years, 1990-2021, with projections to 2035: a systematic analysis for the global burden of disease study 2021. *Front Neurol*, 16.

Willems, J. C. (2004). Deterministic least squares filtering. *Journal of Econometrics*, 118(1-2):341–373.

Wonham, W. M. and Francis, B. A. (1975). The internal model principle for linear multivariable regulators. *Applied Mathematics & Optimization*, 2(2):170–194.

Xudong, Y. (2012). Nonlinear adaptive learning control with disturbance of unknown periods. *IEEE Transactions on Automatic Control*, 57(5):1269–1273.

Yi, A., Zahedi, A., Wang, Y., Tan, U.-X., and Zhang, D. (2019). A novel exoskeleton system based on magnetorheological fluid for tremor suppression of wrist joints. In *2019 IEEE 16th International Conference on Rehabilitation Robotics (ICORR)*, pages 1115–1120.

Yin, Q. and Zhang, T. (2024). Tremor suppression using functional electrical stimulation based repetitive control. In *2024 IEEE/ACIS 24th International Conference on Computer and Information Science (ICIS)*, pages 156–161.

Yu, M. and Huang, D. (2015). Switching adaptive learning control for nonlinearly parameterized systems with disturbance of unknown periods. *International Journal of Robust and Nonlinear Control*, 25(9):1327–1337.

Zames, G. and El-Sakkary, A. (1981). Uncertainty in unstable systems: The gap metric. *IFAC Proceedings Volumes*, 14(2):149–152. 8th IFAC World Congress on Control Science and Technology for the Progress of Society, Kyoto, Japan, 24-28 August 1981.

Zhang, Z., Chu, B., Liu, Y., Li, Z., and Owens, D. H. (2022a). Multimuscle functional-electrical-stimulation-based wrist tremor suppression using repetitive control. *IEEE/ASME Transactions on Mechatronics*, 27(5):3988–3998.

Zhang, Z., Chu, B., Liu, Y., Ren, H., Li, Z., and Owens, D. H. (2022b). Multiperiodic repetitive control for functional electrical stimulation-based wrist tremor suppression. *IEEE Transactions on Control Systems Technology*, 30(4):1494–1509.

Zhang, Z., Huo, B., Liu, Y., Dong, A., and Yu, H. (2024). Active disturbance rejection control of wrist tremor suppression system with additional high-order repetitive control component. *IEEE/ASME Transactions on Mechatronics*, pages 1–12.

Zhou, C., Ogata, K., and Fujii, S. (1996). Adaptive switching control method and its application to tracking control of a robot. In *Proceedings of the 1996 IEEE IECON. 22nd International Conference on Industrial Electronics, Control, and Instrumentation*, volume 1, pages 214–219 vol.1.

Zhou, Y., Ibrahim, A., Hardy, K. G., Jenkins, M. E., Naish, M. D., and Trejos, A. L. (2021). Design and preliminary performance assessment of a wearable tremor suppression glove. *IEEE Transactions on Biomedical Engineering*, 68(9):2846–2857.

Zierle-Ghosh, A. and Jan, A. (2023). Physiology, body mass index. In *StatPearls*. StatPearls.

Zirh, A. (1999). Stereotactic thalamotomy in the treatment of essential tremor of the upper extremity: reassessment including a blinded measure of outcome. *Journal of neurology, neurosurgery, and psychiatry*, 66(6):772–775.